

NUMERICAL EXPERIMENTS IN CORE-COLLAPSE SUPERNOVA
HYDRODYNAMICS

by

Rodrigo A. Fernández

A thesis submitted in conformity with the requirements
for the degree of Doctor of Philosophy
Graduate Department of Astronomy & Astrophysics
University of Toronto

Copyright © 2009 by Rodrigo A. Fernández

Abstract

Numerical Experiments in Core-Collapse Supernova Hydrodynamics

Rodrigo A. Fernández

Doctor of Philosophy

Graduate Department of Astronomy & Astrophysics

University of Toronto

2009

The explosion of massive stars involves the formation of a shock wave. In stars that develop iron cores, this shock wave stalls on its way out due to neutrino emission and the breakup of heavy nuclei flowing through the shock. For the explosion to succeed, a fraction of the gravitational binding energy of the collapsed core that is radiated in neutrinos needs to be absorbed by the material below the shock. How much energy is needed depends on the interplay between non-spherical hydrodynamic instabilities, neutrino heating, and nuclear dissociation. This thesis seeks to understand this interplay through numerical experiments that model the key physical components of the system and separate them out to examine their individual effects. Specifically, one- and two-dimensional time-dependent hydrodynamic simulations are performed to study the effects of non-spherical shock oscillations, neutrino-driven convection, and alpha particle recombination on the dynamics of the system and the critical heating rate for explosion.

We find that nuclear dissociation has a significant effect on the linear stability and saturation amplitude of shock oscillations. At the critical neutrino heating rate for an explosion, convection due to a negative entropy gradient plays a major role in driving dipolar shock motions. One dimensional explosions are due to a global instability involving the advection of entropy perturbations from the shock to the region where the accretion flow cools due to neutrino emission. Large scale shock expansions in two-dimensions are due to a finite amplitude instability involving the balance between buoyancy forces and the

ram pressure of the flow upstream of the shock. During these expansions, a significant amount of energy is released when nucleons recombine into α particles, constituting a significant last step in the transition to explosion. The critical neutrino heating rate for an explosion depends sensitively on the starting radius of the shock relative to the radius at which the binding energy of an α particle is comparable to the gravitational binding energy.

Acknowledgements

My thanks go first of all to my PhD supervisor Chris Thompson, for guiding me through this amazing journey of learning and discovery, and for providing unwavering support throughout my time as his student.

I'm also grateful to Jonathan Dursi, for very valuable help with the FLASH code, and for illuminating scientific discussions. My PhD committee members, Marten van Kerkwijk and Ue-Li Pen, were always supportive of this research from its very beginning, providing constructive feedback during committee meetings, qualifier exam, and defense. My thanks also go to Ethan Vishniac and Ray Carlberg, for having read my thesis and asked interesting questions during my defense, allowing me to look at this work from a different angle. I'm grateful to Adam Burrows, Christian Ott, and Jeremiah Murphy, for stimulating discussions on the Core-Collapse Supernova problem, which helped widen my perspective of this fascinating topic; to Peichun Tsai, for discussions on fluid instabilities; and to Marc Goodman and the CITA requests team, for always being there to help when trouble arose.

Finally, my thanks go to my mother, Leda, for her love and support.

All the figures and significant parts of the text of this thesis form part of two articles that have been published or are in press at The Astrophysical Journal [Fernández & Thompson (2009b) and Fernández & Thompson (2009a), respectively]. The material has been reproduced by permission of the AAS. The software used in this work was, in part, developed by the DOE-supported ASC / Alliance Center for Astrophysical Thermonuclear Flashes at the University of Chicago. Computations were performed in the CITA Sunnyvale cluster, which was funded by the Canada Foundation for Innovation. This research was supported by NSERC and the Ontario Graduate Scholarship Program.

Contents

1	Introduction	1
1.1	Overview	1
1.2	Importance for Astrophysics	2
1.3	The Explosion Mechanism	4
1.3.1	Constraints from Observations and Stellar Evolution Theory	4
1.3.2	Early Theories	8
1.3.3	The Neutrino Mechanism	9
1.3.4	Alternative Mechanisms	14
1.4	This Thesis	16
2	Methods	21
2.1	Overview	21
2.2	Physical Model	21
2.2.1	Equation of State	24
2.2.2	Energy Source Terms	27
2.3	Numerical Model	29
2.3.1	Initial Conditions	29
2.3.2	Time Dependent Aspects	34
2.4	Diagnostic Methods	41

2.4.1	Procedure for Obtaining SASI Eigenfrequencies from a Hydrodynamical Simulation	41
2.4.2	Linear Stability Analysis with Nuclear Dissociation Downstream of the Shock	42
2.4.3	Residency Time	44
3	Linear Phase of the SASI	45
3.1	Overview	45
3.2	Comparison of Hydrodynamical Simulation and the Solution to the Eigenvalue Problem	47
3.3	Dependence of Eigenfrequencies on Nuclear Dissociation and Adiabatic Index	55
3.4	On the linear instability mechanism	58
3.5	Summary	64
4	Non-Linear Phase of the SASI	66
4.1	Overview	66
4.2	From Linear Instability to Saturation	67
4.3	Time-Averaged Properties	68
4.4	Convection and the SASI	75
4.5	Summary	84
5	Explosions Hydrodynamics in One and Two Dimensions	87
5.1	Overview	87
5.2	One-Dimensional Simulations	88
5.3	Two-Dimensional Simulations	91
5.3.1	Heat Engine in a Two-Dimensional Explosion	93
5.3.2	Residency Time	97
5.4	Summary	100

6	Effects of α-Particle Recombination	101
6.1	Overview	101
6.2	One-Dimensional Simulations	102
6.3	Two-Dimensional Simulations	106
6.4	Critical Heating Rate for Explosion	112
6.5	Summary	120
7	Conclusions	123
A	NSE Model	126
B	Initial Model Equations	129
C	Nuclear Burning in FLASH2.5	132
	Bibliography	135

Chapter 1

Introduction

1.1 Overview

Core-collapse supernovae are the last stage in the life cycle of massive stars, during which an explosion powered by the gravitational collapse of the stellar core expels the envelope, injecting $\sim 10^{51}$ erg into the surrounding interstellar medium (e.g., Woosley et al. 2002). Observationally, these explosions manifest themselves as a sudden increase in brightness at the location of the progenitor star, with a subsequent decay on a timescale of weeks to months. The explosion leaves behind either a neutron star or a black hole.

The term supernova comes from the Latin word *nova*, which means *new*. The latter was originally used by Tycho Brahe in his book *De Nova Stella* to denote a “new star” that he observed to appear in the sky in 1572 (Murdin & Murdin, 1985). Such “guest stars” had been recorded by Chinese astronomers as early as 185 CE. Baade & Zwicky (1934b) first distinguished *classical novae*, with a typical bolometric luminosity $\gtrsim 10^{38}$ erg s⁻¹ (Gallagher & Starrfield, 1978) and a Galactic rate of ~ 50 yr⁻¹ (Shara, 1989), from *supernovae*, which at peak emit $\sim 10^{42}$ erg s⁻¹ in photons (Woosley et al., 2002) and occur at a rate $\sim 1/100$ yr⁻¹ in the Milky Way (Cappellaro et al., 1999). The former arise from a thermonuclear explosion on the surface of a white dwarf that

accretes matter from a low-mass stellar companion (Gallagher & Starrfield, 1978), while the latter can have two origins. Type Ia supernovae, which at their peak display strong silicon absorption but no hydrogen lines in their spectrum, are thought to originate in the runaway thermonuclear burning of a white dwarf that completely disrupts it (e.g., Hillebrandt & Niemeyer 2000). The remaining supernova types (Ib, Ic, and II) correspond to core-collapse supernovae (e.g., Woosley et al. 2002).

Given the low Galactic rate, most core-collapse supernova data accumulated with modern telescopes correspond to events in distant galaxies. This normally means that only their optical, near infrared, and (for some objects) X-ray and/or radio emission can be detected (e.g., Hamuy 2004). An exception to this was Supernova 1987A (SN 1987A) in the Large Magellanic Cloud (LMC). The small distance (50 kpc) allowed the detection of neutrinos from the explosion, very detailed long term observations of the electromagnetic light curve, and an unambiguous identification of the stellar progenitor from previous stellar population studies in the LMC, providing a rich dataset to which theories could be compared (Arnett et al., 1989). In spite of this increase in our understanding of core-collapse supernovae, some fundamental questions regarding the explosion mechanism remain still unanswered.

In what follows, we elaborate on the importance of core-collapse supernovae for astrophysics, review previous and current work on the explosion mechanism, and lay out the questions that we address in this thesis.

1.2 Importance for Astrophysics

Core-collapse supernovae play a fundamental role in the evolution of the universe. They are: (1) the site where a significant fraction of heavy elements is produced; (2) the place where neutron stars are born; and (3) the source of shock waves that are believed to accelerate most Galactic cosmic rays. We expand on each of these aspects below.

In addition to the advanced stages of nuclear burning experienced by stars more massive than $8M_{\odot}$, several nuclear processes take place after a successful supernova shock is launched (Burbidge et al. 1957; see Wallerstein et al. 1997 or Woosley et al. 2002 for a recent review): *explosive burning* of Si, O, C, and Ne, which together account for a significant fraction of ejected elements up the iron group; the *p process*, which creates proton rich nuclei such as ^{168}Yb through absorption of γ -rays; the *neutrino process*, which arises due to scattering of μ and τ neutrinos off abundant targets, exciting nuclei to unbound levels that decay by emitting a neutron, and producing nuclei like ^{19}F from ^{20}Ne ; and the *r process* or rapid neutron capture process, which is thought to take place in the neutrino driven wind following the explosion (or in a high entropy outflow from a highly asymmetric explosion), and which is responsible for generating about one half of the neutron-rich nuclei heavier than iron.

The initial collapse of the iron core is halted when the central regions reach nuclear density (Bethe et al., 1979), with a substantial stiffening of the equation of state of the material. This generates sound waves which steepen into an outgoing shock (Brown et al., 1982), in what supernova theorists call the *bounce* phase. The core that is left behind stores its gravitational energy of collapse in thermal and degeneracy energy. The bulk of the core is dense enough to be opaque to neutrinos, with its outer surface conventionally defined at the point where the optical depth for neutrinos reaches $2/3$: the *neutrinosphere*¹. Neutrinos diffuse from the inner core towards the neutrinosphere, at which point they become free to leave the system. In this way, the collapsed core loses heat and lepton number and contracts, much in the same way as a protostar undergoes Kelvin-Helmholtz contraction. The collapsed core is correspondingly called *protoneutron star*, and its Kelvin-Helmoltz contraction is conventionally referred to as *deleptonization* (e.g., Burrows et al. 1981). Depending on the outcome of the explosion and the mass

¹Since the opacity for each neutrino species is dominated by a different process, and depends on the neutrino energy, there is a neutrinosphere for each particle species and energy (e.g., Bethe 1990). To simplify the discussion, we take the neutrinosphere to be a single surface in the remainder of this work.

of the progenitor star, the forming neutron star can either survive the supernova, or collapse into a black hole (if the total mass exceeds the maximum mass allowed by the dense matter equation of state; see §1.3.1). Neutron stars are the densest and in some cases also the most magnetized objects in the universe, providing a unique laboratory for probing physics in extreme parameter regimes not accessible in laboratories on Earth (see, e.g., Lattimer & Prakash 2007 and Harding & Lai 2006 for recent reviews).

Cosmic rays are high energy particles that are incident on the Earth's atmosphere. Their energy spectrum follows a power law from 1 GeV to about 10^{20} eV, with changes in the spectral index around $10^{15.5}$, $10^{17.8}$, and 10^{19} eV (the first and second *knee*, and the *ankle*, respectively, e.g., Nagano & Watson 2000). Cosmic rays with energies below the first knee are thought to be of galactic origin, given that their lifetime in the galactic disk is much shorter than the age of the galaxy (e.g., Kulsrud 2005). They are thought to be produced through *diffusive shock acceleration* in supernova remnants (SNRs): high energy particles bounce across the shock many times by scattering off Alfvén waves. This process naturally produces an energy spectrum close to that observed below the first knee (e.g., Blandford & Eichler 1987).

1.3 The Explosion Mechanism

1.3.1 Constraints from Observations and Stellar Evolution Theory

Theoretical lightcurves of core-collapse supernovae in the ultraviolet, optical, and near-infrared are relatively well understood. The critical parameters are the mass of the hydrogen envelope, the radius, the explosion energy, and the mass of ^{56}Ni synthesized. The lightcurve is quite insensitive to the details of energy injection in the collapsed core (Woosley et al., 2002). However, the simplest radiation transfer models do not say any-

thing about the shape of the explosion, and how the energy and ejecta are distributed in space. There is increasing observational evidence pointing to explosions being intrinsically asymmetric, such as the early detection of radioactive element emission and clumpy ejecta from SN1987A (see references in Janka & Mueller 1996 and Kifonidis et al. 2006), jet-like outflows from the supernova remnant Cas A (e.g., DeLaney et al. 2009), and spectropolarimetric observations that show an increase in the asymmetry of the ejecta as the photosphere reaches the helium core boundary (e.g., Wang & Wheeler 2008). Obtaining the explosion energy from first principles and as a function of progenitor mass and metallicity is one of the main goals of supernova theory. The amount of heavy elements synthesized, mass cut, type of remnant, and binary effects are also of interest. Although the explosion mechanism is currently not well understood, significant constraints can be obtained from stellar evolution theory.

Stars with main sequence masses below about $8M_{\odot}$ develop a degenerate core and do not ignite carbon, while stars above about $11M_{\odot}$ ignite carbon non-degenerately and go through all the advanced nuclear burning stages leading to the formation of an iron core (Woosley et al., 2002). In between², the star develops an O-Ne-Mg core, and its subsequent evolution can follow two paths: either (1) form a heavy white dwarf, or (2) become unstable due to electron capture and collapse to a neutron star, triggering a supernova (Miyaji et al., 1980). In the second case, the steepness of the density profile outside the O-Ne-Mg core makes it easy for the shock to succeed: the mass accretion rate decreases rapidly with time. Hence this type of supernova is not considered to be problematic: explosions are found in spherical symmetry through the neutrino mechanism, albeit somewhat subluminous (explosion energy $\sim 10^{50}$ erg, Kitaura et al. 2006, see also §1.3.3).

In stars of solar metallicity, the mass of the iron core is thought to depend weakly

²The precise limits of this mass interval depend on the helium abundance, metallicity, and the treatment of convection and convective overshoot in stellar models (Woosley et al., 2002).

on progenitor mass above $\sim 30M_{\odot}$ due to the nearly complete ejection of the hydrogen envelope (Woosley et al., 2002). The mass of iron and neutron-rich elements ejected per supernova is limited by abundance measurements in stars (Weaver et al., 1978). A lower limit to the *baryonic mass*³ of the remnant is given by the mass of the iron core (Woosley et al., 2002). A jump in entropy and steep density decline outside the oxygen burning shell also suggests that the baryonic mass of the remnant is limited from above by the mass enclosed by the oxygen layer (Woosley et al., 2002). These two bounds on the remnant are respectively 1.4 and $1.6M_{\odot}$ for progenitors above $30M_{\odot}$, and essentially the same for $15M_{\odot}$ stars (Fig. 17 of Woosley et al. 2002). The oxygen shell mass increases in between 20 and $30M_{\odot}$ progenitors, peaking above $2M_{\odot}$ around $25M_{\odot}$.

Based on these results, the following conclusions are usually drawn for stars that form iron cores. (1) There is a mass limit around $20M_{\odot}$ below which a type II supernova and a neutron star results, the explosion mechanism being not well understood at present. (2) The lower mass limit for black hole formation is determined by the amount of *fallback*: even if a successful supernova is launched, the mass of the remnant can rise above the maximum mass allowed by the dense matter equation of state. The details of fallback depend on the explosion mechanism and progenitor density structure (e.g., Woosley & Weaver 1995), while the equation of state above nuclear saturation density is still not well understood, so this mass limit is highly uncertain at present. (3) A failed explosion would of course result in massive fallback and the formation of a black hole. (4) Stars above $30 M_{\odot}$, or less massive stars in binaries, are thought to be the progenitors of type Ib and Ic supernovae due to the lack of hydrogen lines in their spectra.

Large uncertainties in the post-main sequence mass loss prevent a definite conclusion about whether a neutron star or a black hole is left after the explosion of a star with mass above $30M_{\odot}$ (Woosley et al., 2002). Nevertheless, the similarity in the He core mass with

³This is the rest mass in unbound baryons. During deleptonization, the protoneutron star radiates away $\sim 10 - 15\%$ of its rest mass in neutrinos, therefore the final *gravitational mass* is lower than the baryonic mass by this amount (Woosley et al., 2002).

$15M_{\odot}$ progenitors suggests that the same explosion mechanism operates in supernovae of type Ib,c and type II (Woosley et al., 2002). In the case where the conventional explosion fails, a different type of explosion can be powered if there is enough angular momentum to form a disk, resulting in a long duration gamma-ray burst (Bodenheimer & Woosley, 1983; Woosley, 1993; MacFadyen & Woosley, 1999). This is supported by increasing evidence that this type of gamma-ray bursts are accompanied by (mostly type Ic) core collapse supernovae (although the reverse is not necessarily true, Woosley & Bloom 2006).

For stars of lower metallicity, stellar winds are less powerful and the mass limit for hydrogen envelope ejection increases. This also means that the mass of the iron core increases and therefore, in addition to fallback, direct black hole formation during collapse becomes possible (Woosley et al., 2002). If the helium core reaches $40M_{\odot}$, a different instability takes place (Fowler & Hoyle, 1964; Bond et al., 1984): the increase in internal energy due to contraction following helium burning goes into the formation of electron-positron pairs. The creation of these particles temporarily reduces the adiabatic index below $4/3$ and collapse ensues, with the continuing temperature increase resulting in even more pairs. Up to about $130M_{\odot}$ He core mass (Woosley et al., 2002), the onset of oxygen burning is able to halt the implosion. Since the collapse is dynamic, the central temperature overshoots the value implied by hydrostatic equilibrium, and the excess nuclear burning results in a thermonuclear explosion that completely disrupts the star. This is commonly known as a *pair instability supernova*. Above $130M_{\odot}$, however, thermonuclear burning is not able to halt collapse and, in the absence of rotation, the star collapses directly to a black hole. Rotation increases the limiting mass. Stars with helium cores large enough to trigger the pair-instability mechanism have main sequence masses $\sim 100M_{\odot}$ or higher (Woosley et al., 2002) and are thus very rare. This mechanism is therefore only relevant for Population III stars.

A complete understanding of the explosion mechanism of non-rotating⁴ progenitors, with metallicities comparable to solar, would enable to obtain from first principles the explosion energy, nucleosynthetic yields, and the type of remnant, all as a function of progenitor mass. We now review previous steps in this direction, leading us to the current state of the field.

1.3.2 Early Theories

Baade & Zwicky (1934b) were the first to estimate, from the visual lightcurve, that the total energetic output from of a supernova is $\sim 10^{51} - 10^{54}$ erg, and that this implies a fundamental transformation of the star. They further proposed in Baade & Zwicky (1934a) that the explosion is the result of the transition from a normal star to a neutron star. Burbidge et al. (1957) explained how the collapse of the iron core of a massive star is initiated once the Chandrasekhar mass is approached. The dissociation of iron into alpha particles, and electron captures such as $^{56}\text{Fe} + e^- \rightarrow ^{56}\text{Mn} + \nu_e$ reduce the pressure support and allow the collapse to take place on the dynamical time. They proposed that the explosion was powered by thermonuclear burning of the outer layers of the core due to an increase in the temperature following collapse.

The first time-dependent hydrodynamic calculations of stellar explosions were performed by Stirling Colgate and collaborators at Lawrence Livermore National Laboratory in the 1960s. They wished to understand the γ -ray signature of supernovae in satellites that were being designed to verify a nuclear test ban in space, the same satellites that would later discover γ -ray bursts (Colgate, 2004). Colgate & Johnson (1960) calculated the evolution of an outward propagating shock generated by injecting 10^{52} erg at the center of the system (mimicking the energy release from gravitational collapse). The energy was calibrated so as to eject $1M_{\odot}$ of material, in agreement with observations.

⁴Most massive, solar metallicity stars are expected to have rotation rates that, although rapid compared with the sun, have no dynamical importance in an explosion (Heger et al., 2005), see also §1.3.4.

They focused on the spectrum of cosmic rays that was generated during the expansion of the shock through the outer stellar layers. Colgate & White (1966) included the gravitational collapse of the core in their calculations, which releases far more energy than the thermonuclear burning of the outer core. They found that the energy could be transferred to the outer stellar mantle via high energy (~ 50 MeV) neutrinos arising from accretion onto the hard surface of a small neutron star (~ 10 km). Subsequent work by Arnett (1967) found that this energy transfer mechanism is not efficient enough for stars with massive cores. With a more careful treatment of neutrino transport, Wilson (1971) found that energy transfer was minimal and that the explosion failed altogether.

Freedman (1974) pointed out that the existence of a neutral current (e.g., weak interactions mediated by the Z boson) implies that neutrinos would scatter off heavy nuclei during collapse, thereby preventing excessive neutrino cooling of the collapsed core. At densities $\sim 10^{12}$ g cm $^{-3}$, the collision time for this process becomes comparable to the dynamical time, and neutrinos are said to be *trapped* (e.g., Bethe 1990). By the early 1980s, after several years of continuous improvement in 1D neutrino transport codes, a consensus emerged that the initial bounce shock stalls on its way out due to energy loss to nuclear dissociation and electron capture (e.g., Bowers & Wilson 1982 and references therein).

1.3.3 The Neutrino Mechanism

The next breakthrough came with the discovery by Wilson (1985) that few tenths of a second after the initial shock bounce, the material behind the stalled shock absorbs significant heat from neutrinos, giving rise to an explosion with a somewhat weak energy ($\sim 10^{50}$ erg). This revival of the stalled shock was put on a firmer theoretical footing by Bethe & Wilson (1985), and constitutes the currently favored channel for generating an explosion (the so-called *neutrino mechanism*). The energy transfer takes place via reactions involving the charged weak current (mediated by the W^\pm boson), that is, the

absorption of electron-type neutrinos and antineutrinos by nucleons:

$$\nu_e + n \rightarrow e^- + p \quad (1.1)$$

$$\bar{\nu}_e + p \rightarrow e^+ + n. \quad (1.2)$$

The efficiency of energy transfer by this process needs to be fairly low ($\sim 1\%$, since 10^{53} erg are emitted in neutrinos and the explosion energy is $\sim 10^{51}$ from observations). This encouraged researchers to invest significant effort in improving the methods of neutrino transport, neutrino opacities, and the equation of state of dense matter. Simulations incorporating *multigroup* (energy dependent) Boltzmann neutrino transport showed that stars that form iron cores do not explode in spherical symmetry. This result did not depend on whether Newtonian gravity (Thompson et al., 2003), full general relativity (Liebendörfer et al., 2001; Sumiyoshi et al., 2005), or a more approximate description of the gravitational field (Rampp & Janka, 2002) was employed. Lower mass stars which form an O-Ne-Mg core can explode in spherical symmetry by this mechanism (Kitaura et al., 2006; Janka et al., 2008).

With the availability of increasing computational power, numerical simulations in more than one spatial dimension became possible in the 1990s. Herant et al. (1992) were the first to perform two-dimensional hydrodynamic calculations of the postbounce phase, with an approximate implementation of the neutrino physics. They found that convection is excited by neutrino heating outside the neutrinosphere, thereby increasing the residency time of infalling material, and generating successful explosions for cases that failed in one dimension. They also found that the convective cells extended to large scales, potentially leading to an asymmetric explosion. The presence of a negative entropy gradient behind the shock had already been pointed out by Bethe (1990) as a driver of postshock convection. Subsequent work with approximate neutrino physics by Miller et al. (1993), Herant et al. (1994), Burrows et al. (1995), Janka & Mueller (1996), and Mezzacappa et al. (1998) found indeed that postshock convection was vigorous,

but did not agree as to whether it would make a difference in reviving a stalled shock that would otherwise fail in one dimension. The disagreement originated in the differing approximations that were employed for the neutrino heating and cooling, as well as the numerical methods for treating the hydrodynamics (Mezzacappa et al., 1998).

Convection of a different sort had already been suggested by Epstein (1979) to occur below the neutrinosphere, driven by the negative lepton gradient that arises due to the diffusion of neutrinos out of the protoneutron star. Using a mixing-length approach, Burrows (1987) found that protoneutron star convection yielded a 50% increase in the temperature of the neutrinosphere, with consequent increases in the neutrino luminosities. Doubly diffusive instabilities that assume faster heat diffusion than lepton number diffusion (neutron fingers) were invoked by Wilson & Mayle (1988) and Wilson & Mayle (1993) to enhance the neutrino luminosities, allowing them to obtain successful explosions. A more careful analysis by Bruenn et al. (2004) shows that diffusion of lepton number is always faster than thermal diffusion, which prevents neutron fingers from forming. More recent two-dimensional hydrodynamic simulations with multigroup neutrino transport show that indeed neutron fingers do not arise, and that protoneutron star convection takes place in a limited layer of negative lepton gradient. Convection significantly affects the μ and τ neutrino luminosities, but yields only modest changes for ν_e and $\bar{\nu}_e$ (Buras et al., 2006b; Dessart et al., 2006). The amplification and transport of magnetic fields by protoneutron star convection has been considered by Thompson & Duncan (1993) and Thompson & Murray (2001), respectively, although the effect on the explosion mechanism when no significant rotation is present has only been explored analytically by Thompson (2000).

Two-dimensional collapse calculations with a more realistic treatment of neutrino transport became available in the past several years, revealing the importance of multi-dimensional instabilities above the neutrinosphere for the explosion mechanism (Walder et al., 2005; Swesty & Myra, 2005b,a; Buras et al., 2006b,a; Burrows et al., 2006, 2007b;

Ott et al., 2008; Marek & Janka, 2009). Buras et al. (2006a) found that an $11M_{\odot}$ model, which did not explode in spherical symmetry, also failed when the two-dimensional grid was restricted to a 90 degree wedge around the equator. However, when the grid was allowed to cover the whole range of polar angles, a successful (albeit marginal) explosion was uncovered. The reason is that the postshock fluid was able to perform strong dipolar motions, which strengthened convection and allowed the absorption of enough heat to trigger an explosion. Similar results were obtained by Marek & Janka (2009) with the same $15M_{\odot}$ model as Buras et al. (2006b) and a 180 degree grid. In this case some evidence for an explosion is obtained at late times (~ 600 ms), with strong dipolar overturns of the postshock flow and recombination of α -particles. The work of Burrows et al. (2006) and Burrows et al. (2007b) also found strong dipolar motions, but they obtained explosions powered by a different mechanism (see §1.3.4).

Blondin et al. (2003) found that a standing spherical accretion shock is linearly unstable to non-spherical perturbations in the absence of convection. Using a simplified setup, which neglects the energy loss due to nuclear dissociation but otherwise starts with a density profile similar to that seen in full collapse calculations, they found that the shock develops an overstable mode in two dimensions, but is stable in spherical symmetry. The origin of the linear instability became the subject of debate, with Blondin & Mezzacappa (2006) arguing for a purely acoustic cycle, and Foglizzo et al. (2007) favoring a feedback between advected entropy-vortex perturbations and outgoing sound waves. Interest in the stability of the shocked fluid remained vivid, as it became clear that dipolar instabilities could be the origin of the high proper motions of radio pulsars. However, one should be cautious in associating this linear instability (commonly referred to as *Standing Accretion Shock Instability*, or SASI) with the large amplitude shock motions observed in full collapse calculations, as the latter arise in the presence of strong convective motions that are driven by neutrino heating. It is also unclear how nuclear dissociation at the shock affects its stability.

Given that full collapse calculations are expensive computationally, a set of two-dimensional (2D), parametric hydrodynamic studies that approximate the effects of neutrino transport have been performed recently to probe multidimensional effects (Fryer et al., 2006; Scheck et al., 2006; Ohnishi et al., 2006; Fryer & Young, 2007; Scheck et al., 2008; Iwakami et al., 2008; Murphy & Burrows, 2008). Ohnishi et al. (2006) conducted simulations of a standing accretion shock with a steady-state initial condition, including heating and cooling as energy source terms and using a realistic equation of state. They also found that the nonlinear shock oscillations are dominated by large scale modes, and that the mode periods scale with the postshock advection time (in line with the interpretation of Foglizzo et al. 2007 and the quantitative results of the linear stability analysis of Yamasaki & Yamada (2007)). Scheck et al. (2006) and Scheck et al. (2008) performed a large number of simulations that use approximate neutrino transport but a realistic equation of state. They found dipolar asymmetries large enough to explain the proper motions of most radio pulsars, and showed that convection is damped by strong accretion, as predicted by the linear analysis of Foglizzo et al. (2006). Fryer & Young (2007) studied the effects of shock motions on convection using an SPH code and grey neutrino transport, finding that in 3D the dipolar mode is not dominant.

Work by Blondin & Mezzacappa (2007) and Blondin & Shaw (2007) has investigated the nature of the 3D SASI without including the effects of neutrino heating or nuclear dissociation. They find that the shock can develop a spiral mode that could in principle spin up the forming neutron star. Iwakami et al. (2008) studied the development of the SASI in three dimensions (3D) with the same model as Ohnishi et al. (2006), focusing on the saturation properties and its comparison with the 2D case. The linear stability study of Yamasaki & Foglizzo (2008) has shown that at the equatorial midplane, the advective-acoustic cycle argued by Foglizzo et al. (2007) to drive the linear SASI also favors spiral modes that rotate in the same direction as the accretion flow.

1.3.4 Alternative Mechanisms

At present, the neutrino mechanism remains viable, and the fact that it arises naturally from the global energetics of the system makes it the favored one. But given the failures of spherically symmetric simulations and marginal success in the 2D case, it is not guaranteed to be robust. Here we briefly review alternative mechanisms that have been explored previously.

LeBlanc & Wilson (1970) investigated the consequences of rapid rotation and magnetic fields on the collapse with time-dependent 2D cylindrical axisymmetric MHD simulations. Starting with a uniformly rotating core with strong poloidal magnetic field, they found that at high densities, the centrifugal force becomes dynamically important, with significant deviations from spherical symmetry taking place. Strong differential rotation amplifies the magnetic field by a factor ~ 100 over pure flux freezing due to collapse. Once the collapse halts, this toroidal field generates an axial jet that causes a bipolar explosion due to an increase in the magnetic over gas pressure along the rotation axis. This constitutes the essence of the *magnetorotational mechanism*, with subsequent computations having improved the physics but still finding the same qualitative result. An important step forward was taken with the work of Akiyama et al. (2003), who showed that the magnetorotational instability (MRI) leads to exponential amplification of a seed magnetic field at the boundary of the protoneutron star as well as in the postshock cavity, in contrast to the linear growth of toroidal field by line wrapping found by LeBlanc & Wilson (1970). To date, the work of Burrows et al. (2007a) remains the only⁵ time-dependent 2D MHD collapse simulation of iron-core stars to include multigroup neutrino transport. They find powerful explosions, although they need to assume rapid rotation in the pre-collapse core (period of 2 s) and large seed magnetic fields ($\sim 10^{11}$ G). The main problem with the magnetorotational mechanism is that rapid progenitor rotation presents poten-

⁵Dessart et al. (2007) have performed 2D multigroup neutrino-transport MHD simulations of accretion induced collapse of a white dwarf to a neutron star.

tial problems, because if too large it can result in the neutron star over-energizing the surrounding nebula (e.g., Ott et al. 2006). Hence the rotational kinetic energy needed for successful magnetorotational models is somewhat fine-tuned. Also, axisymmetric velocity fields cannot sustain axisymmetric fields via dynamos action (Cowling, 1933), hence three-dimensional simulations are required for proper modeling of this scenario.

Burrows et al. (2006) performed a full 2D core-collapse calculation of a $15 M_{\odot}$ star with a computational grid that transitions from spherical to cartesian at ~ 20 km, allowing the collapsed core to move relative to the center of mass of the system. They found that neutrino heating was not able to drive an outflow, but instead that the explosion developed at late times (~ 1 s) and was powered by acoustic emission from the protoneutron star. They interpreted this acoustic emission as arising from dissipation of saturated g-modes of the collapsed core, which are excited by anisotropic accretion plumes caused by the strong dipolar shock motions. Correspondingly, this has been named the *acoustic mechanism*. Burrows et al. (2007b) found that it is able to power explosions for progenitor stars up to $25M_{\odot}$. The advantage of this mechanism is that it operates whenever the neutrino mechanism fails. However, it remains controversial for several reasons. First, because the core can only move along the axis of symmetry in a 2D axisymmetric simulation, increasing the dimensionality may result in lower saturation amplitudes and thus insufficient acoustic power to energize the shock. Second, it has not been verified independently: Marek & Janka (2009) find g-modes in their protoneutron star, but not with the amplitudes reported in Burrows et al. (2006)⁶. Finally, the analytic work of Weinberg & Quataert (2008) found that the dominant dipolar g-mode witnessed in the simulations of Burrows et al. (2006) is nonlinearly coupled to modes of a high radial order, which are dissipated by neutrino diffusion. These modes cannot be resolved by Burrows et al. (2006), and can lower the g-mode saturation energy by a factor ~ 100 . The

⁶The simulations of Marek & Janka (2009) do not, however, follow the evolution to ~ 1 s as done by Burrows et al. (2006), and evolve the inner part of their core in spherical symmetry to avoid the angular timestep restriction at small radii.

work of Fryer & Young (2007) made with an SPH code in 3D does not find a significant core motion. Full neutrino transport in 3D at high resolution is required to settle the fate of this mechanism, to capture multidimensional and dissipation processes effectively.

Very recently, Sagert et al. (2009) modeled the collapse of $10M_{\odot}$ and $15M_{\odot}$ stars in spherical symmetry using an equation of state that allows for a phase transition to deconfined quark matter. After the initial bounce shock becomes stalled, a fraction of the protoneutron star enters a mixed quark-hadronic phase, which decreases the adiabatic index and triggers a second collapse. This second collapse is halted by the formation of pure quark matter, generating a second shock. When the second shock meets the original stalled shock, the system gains enough energy to trigger an explosion. A key prediction of this model is the appearance of a second neutrino burst due to the passage of the second shock across the neutrinosphere. At present, the quark matter equation of state is computed with a phenomenological model (the MIT bag) which is parameter dependent. Further progress in quantum chromodynamics at high densities is needed to understand the feasibility of this model.

1.4 This Thesis

Dating back to the early days of time-dependent calculations, theorists have tried to use state-of-the art progenitor models, microphysics, and numerical techniques. This is generally viewed as the only way in which the combination of physical processes driving an explosion will ultimately be uncovered. However, the task is daunting: in particular, extending multi-energy and multi-species neutrino transport to three spatial dimensions is not possible with current computational capabilities (e.g., Marek & Janka 2009). The many nonlinear feedbacks that are present make it difficult to disentangle the causes of even the most dramatic global effects (e.g., the results of Burrows et al. 2006 and Marek & Janka (2009)).

An alternative approach, also dating back to the first time-dependent calculations, has been to use approximate descriptions of various components of the physics, in an attempt to speed up the otherwise slow progress towards full realism, or to gain a more fundamental understanding of global phenomena through parametric studies. Given the fact that developing a full core-collapse code is a long undertaking, we take the second approach in this thesis.

Numerous unexplained aspects of global instabilities observed in full collapse calculations can be addressed with a simplified hydrodynamic setup that nonetheless includes the essential physics in a parameterized form. In particular, the effects of nuclear dissociation on the stability of the shock have not been studied separately⁷, despite being one of the most significant sources and sinks of energy in the system. Indeed, at an accretion rate of $0.3M_{\odot} \text{ s}^{-1}$ over 200 ms, full dissociation of iron (8.8 MeV per nucleon, Audi et al. 2003) takes away 10^{51} erg of internal energy and thus pressure support behind the shock.

The material which flows through the stalled shock (predominantly iron, silicon, and oxygen) is only weakly bound to the forming neutron star, but loses roughly half of its kinetic energy to nuclear dissociation. The Bernoulli parameter (enthalpy plus kinetic and gravitational energies, equal to the energy flux divided by mass flux) of the shocked material with this dissociation energy subtracted becomes substantially negative. Much of this dissociation energy can be restored if protons and neutrons recombine into alpha particles, but this generally requires an outward expansion of the shock from the radius of $\sim 100 - 150$ km at which it typically stalls. The successful expansion of the shock does not, however, require imparting positive energy to the entire post-shock fluid: buoyancy forces will drive a global finite-amplitude instability in the presence of large-scale density inhomogeneities. The stability analysis given in Thompson (2000) shows that a non-spherical breakout of the shock is then possible.

Our main goal is to gain an understanding of results from more realistic but com-

⁷Simulations employing a realistic equation of state implicitly account for this effect.

plicated simulations in terms of fundamental physical principles. In particular, we focus on:

1. The effects of nuclear dissociation on the global modes of the shock in the absence of neutrino heating, and thus in isolation from convection. We also investigate the influence of different matter equations of state and upstream Mach numbers. The goal here is to probe the sensitivity of the modes to different aspects of the flow structure and equation of state.
2. The interplay between these intrinsic overstable oscillations of the shock and convection. We want to understand better the driving agent behind the large amplitude shock displacements that are observed in more complete multidimensional collapse calculations.
3. The dynamics of the shock at the transition from accretion to explosion in one and two spatial dimensions. We intend to gain a more fundamental understanding of global instabilities occurring at this transition, and on the differences introduced by changing the dimensionality of the flow.
4. The effects of α -particle recombination on the dynamics of the flow and the critical heating rate for explosion. Here the goal is to separate out the role of nuclear energy generation.

To pursue these goals, we have designed a set of numerical experiments consisting of time-dependent hydrodynamic simulations of a standing accretion shock that employ equations of state of increasing complexity. We concentrate on the phase of the supernova where the bounce shock has stalled, at which point global instabilities of the flow begin to play a significant role.

We use the code FLASH2.5 (Fryxell et al., 2000), which is well tested in problems involving nuclear energy release in compressible fluids (Calder et al., 2002). We adopt a

steady state model as our initial condition, and a constant mass accretion rate, neutrino luminosity, and fixed inner boundary. The steady-state approximation to the stalled shock phase was first introduced by Burrows & Goshy (1993), and has recently been used by Ohnishi et al. (2006) to study the non-linear development of the shocked flow with a semi-realistic equation of state and neutrino heating.

To address goal #1 above, we start by modeling the accretion flow as a polytropic fluid, from which a fixed dissociation energy is removed immediately below the shock (so as to mimic the most important effect of nuclear dissociation), and allow for neutrino cooling but not heating. We also solve and modify the linear stability calculation of Foglizzo et al. (2007) to study the linear modes of the accretion flow. We then add neutrino heating in a simple, parametrized way, without any attempt at simulating neutrino transport. In this way, we can drive convection below the shock and address goal #2 above. We then gradually increase the intensity of heating until an explosion is uncovered, and study the dynamics obtained around the critical point to investigate goal #3. Finally, we generalize the prescription of constant dissociation energy to allow for nuclear statistical equilibrium (NSE) between neutrons, protons, and α -particles. In this way, the energy feedback from α -particle recombination can be introduced (goal #4).

The plan of this thesis is as follows. In Chapter 2 we describe in detail the physical model we employ in this investigation, the numerical setup used in our time-dependent hydrodynamic calculations, and the diagnostic methods employed to analyze results. Chapter 3 addresses the linear phase of the SASI, focusing on the effects of a finite amount of nuclear dissociation, varying adiabatic index, and incident Mach number on the linear eigenfrequencies, as well as further probing the instability mechanism behind fundamental modes of the flow. In Chapter 4 we employ our hydrodynamic simulations to explore the nonlinear, saturated state of the instability and its energetics in the absence of heating, as well as its interplay with convection when heating is gradually added to the system. Chapter 5 examines the time-dependent dynamics in 1D and 2D when

the heating rate is close the critical value to cause an explosion. Finally, the effects of α -particle recombination on the dynamics and critical heating rate for explosion are investigated in Chapter 6. Chapters 3-6 each close with a summary of the main results, and our general conclusions follow in Chapter 7.

Chapter 2

Methods

2.1 Overview

In this chapter we describe the physical model we employ in our investigation (§2.2), the numerical techniques (§2.3), and analysis tools (§2.4). We focus on the phase of the supernova at which the stalled shock undergoes multidimensional hydrodynamic instabilities. Since we are interested in nonlinear phenomena, we perform time-dependent hydrodynamic simulations, and model nuclear dissociation, gravity, and energy source terms from neutrinos in a schematic way.

2.2 Physical Model

The initial configuration is a steady, spherically symmetric flow onto a gravitating point mass M with a hard surface at some radius r_* , corresponding roughly to the neutrinosphere. More complete core-collapse calculations find that the mass between the neutrinosphere and the shock is at most $\sim 0.1M_\odot$, compared to $1.3 - 1.4M_\odot$ below the neutrinosphere (e.g., Marek & Janka 2009 for a $15M_\odot$ progenitor). Point mass gravity is therefore a reasonable approximation when focusing on the nonlinear dynamics of the shock. Even though seed perturbations in the progenitor star may be amplified dur-

ing collapse (Lai & Goldreich, 2000), the collapsing core is by itself stable to nonradial perturbations (Goldreich & Weber, 1980). In the absence of any physically motivated asphericity in the progenitor, we assume that the collapsing material is spherically symmetric.

The flow contains a standing shock wave, and the settling flow below the shock cools radiatively in a narrow layer outside $r = r_*$. In more realistic calculations, which treat the effect of neutrinos with a higher degree of realism (e.g., Liebendörfer et al. 2001), cooling and heating by neutrinos is a consequence of the radial profiles of two simultaneous processes: cooling due to the capture of electrons and positrons, and heating due to the absorption of electron-type neutrinos and antineutrinos (Bethe & Wilson, 1985) in the regions that are nearly transparent to neutrinos. In our model, we include them as local energy source terms in the energy equation; we elaborate on this approximation in §2.2.2. Similarly, realistic simulations include nuclear dissociation and recombination below the shock implicitly through the equation of state. Here, we want to test the effect of nuclear processes explicitly, therefore we include them as another source term in the energy equation. The details of this are given in §2.2.1.

The space of such accretion shock models is labeled basically by three parameters: accretion rate \dot{M} , luminosity L_ν in electron neutrinos and anti-neutrinos, and the radius r_* of the base of the settling flow. The mass M of the collapsed material represents a fourth parameter, but it covers a narrower range than the other three.

For shock stability calculations without neutrino heating, our parameter space is two-dimensional, and we label it by the size of the envelope r_*/r_{s0} and the amount of nuclear dissociation below the shock, which is equivalent to giving r_{s0} physical dimensions.

In calculations that include heating, we explore a two-dimensional surface through this three-dimensional parameter space by i) fixing the ratio of r_* to the initial shock radius r_{s0} in the absence of heating ($r_*/r_{s0} = 0.4$); ii) allowing r_{s0} to vary with respect to an appropriately chosen physical radius; and then iii) increasing the level of heating until

an explosion is uncovered. In the full problem, the shock radius at zero heating is a unique function of \dot{M} and r_* , with a small additional dependence on M and the composition of the flow outside the shock (Houck & Chevalier, 1992). The secular cooling of the collapsed core forces a gradual decrease in r_* , and \dot{M} also varies with time and with progenitor model.

Given the important role that α -particle recombination plays in the final stages of an explosion, we implement ii) in our simulations with neutrino heating by referencing r_{s0} to the radius where the gravitational binding energy of an α -particle equals its nuclear binding energy,

$$r_\alpha = \frac{GMm_\alpha}{Q_\alpha} \simeq 254M_{1.3} \text{ km.} \quad (2.1)$$

Here $Q_\alpha \simeq 28.30$ MeV is the energy needed to break up an α -particle into 2 neutrons and 2 protons (e.g., Audi et al. 2003), m_α the mass of an α -particle, and $M_{1.3} = M/(1.3M_\odot)$. Choice i) allows us to consider models that have, implicitly, both a range of physical values of r_* and a range of \dot{M} . It is, of course, made partly for computational simplicity (the limited size of the computational domain) and also to facilitate a comparison between models that have different values of r_{s0}/r_α . Once this choice is made, the normalization of the cooling function is adjusted to give a fixed value of r_*/r_{s0} . The heating rate remains freely adjustable thereafter.

We adopt this simplification because we do not intend to find the precise value of the critical neutrino luminosity, but instead to probe the behavior of the system around this critical point, whatever its absolute value.

Our system of units is the following. All flow variables are made dimensionless by scaling radii to the initial shock radius r_{s0} , all velocities to the free-fall velocity at this radius, $v_{\text{ff}0}(r_{s0}) = (2GM/r_{s0})^{1/2}$, the time to the free-fall time $r_{s0}/v_{\text{ff}0}(r_{s0})$, and the density to the initial upstream density ρ_1 . Numerical values appropriate for the stalled shock phase of a core collapse are $r_{s0} \sim 150$ km, $v_{\text{ff}0}(r_{s0}) \sim 4.8 \times 10^9 M_{1.3}^{1/2} (r_{s0}/150 \text{ km})^{-1/2}$ cm s⁻¹, $t_{\text{ff}0} \equiv r_{s0}/v_{\text{ff}0} \sim 3.1 M_{1.3}^{-1/2} (r_{s0}/150 \text{ km})^{3/2}$ ms, and $\rho_1 \sim 4.4 \times 10^7 \dot{M}_{0.3} M_{1.3}^{-1/2}$

$(r_{s0}/150 \text{ km})^{-3/2} \text{ g cm}^{-3}$ (assuming a strong shock). Here the mass accretion rate has been normalized to $\dot{M} = 0.3 \dot{M}_{0.3} M_{\odot} \text{ s}^{-1}$. Throughout this work we denote the average of a function $F(X, \dots)$ over some variable X by $\langle F \rangle_X$. Table 2.1 summarizes the most frequently used, non-standard symbols.

2.2.1 Equation of State

Our equation of state is that of an ideal gas with adiabatic index γ . This choice is made to enable a clear identification of effects caused by the equation of state on the behavior of the flow, some of which are incorporated explicitly in the evolution of the internal energy. We choose the value of γ so as to achieve a realistic density profile near the base of the settling flow, given the fact that we are not explicitly including changes in the electron fraction due to weak processes (see also §2.3.1).

We model nuclear dissociation in two ways. First, we remove a fixed specific energy ε right below the shock. This represents the prompt and complete breakup of whatever heavy nuclei are present in the upstream flow. When $r_{s0} \sim 150 \text{ km}$, the gravitational binding energy per nucleon at the shock is $\sim 12 M_{1.3} (150 \text{ km} / r_{s0}) \text{ MeV}$, higher than the $\simeq 8.8 \text{ MeV}$ binding energy per nucleon of ^{56}Fe (e.g., Audi et al. 2003). In our simplified model, the effect of dissociation is parameterized by a constant dissociation energy per unit mass ε . For example, the complete dissociation of iron into nucleons costs an energy

$$\frac{\varepsilon}{v_{\text{ff0}}^2} \simeq 0.37 M_{1.3}^{-1} \left(\frac{r_{s0}}{150 \text{ km}} \right). \quad (2.2)$$

The main limitation of this approximation is that the dissociation energy does not change with the radius (or inclination) of the shock. The main advantage is simplicity: ε is independent of any dimensional parameters and can be expressed as a fraction of v_{ff0}^2 .

We also use a more accurate dissociation model which allows for NSE between α -particles and nucleons.¹ During the stalled shock phase of core-collapse supernovae, the

¹Although heavier nuclei can begin to recombine once the shock moves significantly beyond r_{α} ,

Table 2.1: List of frequently used, non-standard symbols

Symbol	Description
$\langle F \rangle_X$	Average of function F over variable X
b	Bernoulli parameter, (eq. 2.8)
c_s	Sound speed, equal to $\sqrt{\gamma p / \rho}$
de_{nuc}/dt	Specific nuclear energy generation rate (eq. 2.15)
ε	Specific nuclear binding energy (if no subscript, free parameter; subscripted cases specific to particle species, eqns. 2.3 and 2.4)
H	Normalization of heating function, eqn. (2.6)
ℓ	Index of Legendre polynomial $P_\ell(\cos(\theta))$
\mathcal{L}	Energy generation rate per unit volume. Subscript C corresponds to cooling (eq. 2.5), H to heating (eq. 2.6), and α to particle advection (eq. 2.7)
\mathcal{M}	Mach number
r_*	Stellar radius, inner boundary of the domain
r_α	Radius where α recombination energy equals gravitational binding energy (eq. 2.1)
r_{s0}	Initial shock radius in the absence of heating
r_s	Shock radius
s	Entropy (lower case denotes per unit mass, upper case per baryon)
t_{ff0}	Free-fall time at r_{s0} , equal to r_{s0}/v_{ff0}
v_{ff0}^2	Squared free-fall speed at r_{s0} , equal to $2GM/r_{s0}$
ω_{grow}	Growth rate
ω_{osc}	Oscillation frequency
w_{ad}	Adiabatic rate of change of enthalpy, eq. (6.1)
X_i	Mass fraction of species i , superscript eq denotes NSE value

shock sits at $r \sim 100 - 200$ km, with a postshock temperature $T > 1$ MeV and density $\rho \gtrsim 10^9$ g cm $^{-3}$. In these conditions, the heavy nuclei flowing through the shock are broken up into α , protons, and neutrons. A range of isotopes are present in the iron core of a massive star as well as in nuclear burning shells (Woosley et al., 2002), but since the binding energy per nucleon varies only by $\sim 10\%$ we simply assume a single type of nucleus in the upstream flow. We focus here on the later stages of the stalled shock phase, during which the oxygen shell is accreted. An energy $Q_{\text{O}} \simeq 14.44$ MeV must be injected to dissociate an ^{16}O nucleus into 4 α -particles (Audi et al., 2003), which corresponds to the specific dissociation energy

$$\varepsilon_{\text{O}} = \frac{Q_{\text{O}}}{m_{\text{O}}} = 0.038 M_{1.3}^{-1} \left(\frac{r}{150 \text{ km}} \right) v_{\text{ff0}}^2(r). \quad (2.3)$$

Here $m_{\text{O}} \simeq 16m_u$ is the mass of an oxygen nucleus, with m_u the atomic mass unit. The smallness of this number indicates that little oxygen survives in the post-shock flow, and so we set the equilibrium mass fraction of oxygen to zero below the shock, $X_{\text{O}}^{\text{eq}} = 0$. The binding energy of an α -particle is of course much larger, giving

$$\varepsilon_{\alpha} = \frac{Q_{\alpha}}{m_{\alpha}} = 0.295 M_{1.3}^{-1} \left(\frac{r}{150 \text{ km}} \right) v_{\text{ff0}}^2(r). \quad (2.4)$$

We find that α -particles appear in significant numbers only at relatively large radii ($\gtrsim 0.5 r_{\alpha}$) and in material that has either i) been significantly heated by electron neutrinos closer to the neutrinosphere and rises; or ii) been freshly shocked outside r_{α} . The electrons are only mildly degenerate in material that has a high entropy and α -particle content, so that neutrino heating drives the electron fraction Y_e close to ~ 0.5 (or even slightly above: see, e.g., Buras et al. 2006a). We therefore set $Y_e = 0.5$ in the Saha equation that determines the equilibrium mass fractions X_n^{eq} , X_p^{eq} and $X_{\alpha}^{\text{eq}} = 1 - X_n^{\text{eq}} - X_p^{\text{eq}}$. These quantities are tabulated as functions of the pressure p and density ρ using an ideal, finite-temperature and partially degenerate equation of state for electrons and nucleons; see

this generally occurs only after the threshold for an explosion has been reached, and makes a modest additional contribution to the recombination energy.

Appendix A for details. Specific choices must then be made for the parameters r_{s0} , M , and \dot{M} ; we generally take $M = 1.3 M_\odot$ and $\dot{M} = 0.3 M_\odot \text{ s}^{-1}$, but allow r_{s0} to vary. An investigation of how changes in Y_e feed back onto the formation of α -particles is left for future work.

2.2.2 Energy Source Terms

There are two main energy source terms in the nearly transparent region between the neutrinosphere and the shock. As the accretion flow settles onto the protoneutron star, electrons and positrons are captured onto free nucleons, emitting electron-type neutrinos and antineutrinos. The energy released per unit volume due to this process depends on density and temperature approximately as $\sim \rho T^6$ (e.g., Janka 2001). Using the fact that the temperature $T \propto p/\rho$ for both the nucleon and relativistic particle contribution to the pressure, it is possible to show that the temperature scales inversely with radius in this region (Bethe, 1993). Heating, on the other hand, is due to absorption of electron type neutrinos and antineutrinos leaking from the protoneutron star (eq. 1.1), with a minor contribution from the cooling due to accretion mentioned previously. The specific heating rate is then the specific energy flux from neutrinos times the cross section for absorption: the radial dependence arises from the geometric dilution of the neutrino flux from the protoneutron star, $\sim r^{-2}$ (e.g., Janka 2001). The normalization of both energy source terms is such that they balance each other at some radius between the neutrinosphere and the shock, conventionally called the *gain radius* (Bethe & Wilson, 1985), with heating dominating above this radius.

In our model, the rate of release of internal energy per unit volume has the basic form

$$\mathcal{L}_C = Ap^\alpha \rho^{\beta-\alpha}. \quad (2.5)$$

To make contact with previous calculations, we have adopted the same parameterization as used by Blondin & Mezzacappa (2006), $\alpha = 1.5$, $\beta = 2.5$. This choice of exponents

is consistent with cooling by the capture of non-degenerate e^+ and e^- on free nucleons when the pressure is dominated by relativistic particles. ($\mathcal{L}_C \propto \rho T^6 \propto \rho p^{3/2}$.) Inside the radius where the electrons become strongly degenerate, one has $\mathcal{L}_C \propto p_e^{3/2} n_p \propto (Y_e \rho)^3$. This gives essentially the same dependence of \mathcal{L}_C on r as eq. (2.5) when $Y_e = \text{constant}$ and $\gamma = \frac{4}{3}$ (corresponding to $\rho \propto r^{-3}$ in a nearly adiabatic settling flow). In more realistic collapse calculations, Y_e grows with radius between the neutrinosphere and the shock, but ρ tends to decrease more rapidly than $\sim r^{-3}$ (e.g. Buras et al. 2006b). Our choice of cooling function appears to widen the gain region slightly compared with these calculations, and therefore to reduce the critical heating rate for an explosion. The bulk of the cooling occurs in a narrow layer close to the accretor at $r = r_*$, and the accreted material accumulates in the first few computational cells adjacent to the inner boundary without a major effect on the rest of the flow. The constant normalization factor A determines the radius r_* at which the flow stagnates, and thus the ratio r_*/r_{s0} .

We model neutrino heating as a local energy generation rate per unit volume of the form

$$\mathcal{L}_H = H(1 - X_\alpha)\rho/r^2. \quad (2.6)$$

The normalization constant H measures the strength of the heating. The factor $(1 - X_\alpha)$ accounts for the fact that the cross section for neutrino absorption by α -particles is much smaller than that for free nucleons (Bethe, 1990). For simplicity, we do not include the flux factor due to the transition between diffusion and free-streaming. Our focus here is on the nature of the instabilities occurring in the flow near the threshold for an explosion, and we do not attempt a numerical evaluation of the critical heating rate.

An additional energy source term arises from the change in the equilibrium fraction of α -particles as they are advected in the steady state initial solution. The instantaneous adjustment of X_α to its equilibrium value, combined with eq. (2.14), yields an energy

generation rate per unit volume

$$\mathcal{L}_\alpha = \rho v_r \varepsilon_\alpha \frac{dX_\alpha^{\text{eq}}}{dr} = \rho v_r \varepsilon_\alpha \left[\frac{\partial X_\alpha^{\text{eq}}}{\partial \rho} \frac{d\rho}{dr} + \frac{\partial X_\alpha^{\text{eq}}}{\partial p} \frac{dp}{dr} \right]. \quad (2.7)$$

This energy generation rate is negative, as the temperature increases inwards and thus the α -particle fraction decreases with decreasing radius (the radial velocity v_r is negative).

2.3 Numerical Model

We perform one- and two-dimensional, time-dependent hydrodynamic simulations with FLASH2.5 (Fryxell et al., 2000). This is a second-order Godunov-type adaptive mesh refinement (AMR) code which implements the piecewise parabolic method (PPM) of Colella & Woodward (1984). The code allows for source terms in the equations of momentum and energy conservation, which represent an external gravitational field and spatially distributed heating and cooling, as well as nuclear burning. In what follows, we describe the initial conditions for our runs, and our treatment of time dependent aspects.

2.3.1 Initial Conditions

The spherically symmetric flow has a net rate of mass transfer $\dot{M} = 4\pi r^2 \rho |v_r|$ from the outer boundary to the center. A standing shock is present at $r = r_{s0}$, and the flow outside this shock, weakly bound to the protoneutron star, has a vanishing Bernoulli parameter

$$b \equiv \frac{1}{2} v_r^2 + \frac{\gamma}{(\gamma - 1)} \frac{p}{\rho} - \frac{GM}{r} = 0 \quad (r > r_{s0}), \quad (2.8)$$

which ensures a vanishing energy flux through the shock. In the above, G is Newton's constant. The flow upstream of the shock has a finite pressure p_1 and Mach number $\mathcal{M}_1 = |v_r|/c_{s1} = |v_r|(\gamma p_1/\rho_1)^{-1/2}$, which are related to the upstream density by $p_1 = (\rho_1/[\gamma \mathcal{M}_1^2])(\dot{M}/[4\pi \rho_1 r_{s0}^2])^2$. There is no cooling or nuclear dissociation above the shock, hence the conditions $\dot{M} = \text{constant}$, $b = 0$, and the equation of state completely determine the initial flow for $r > r_{s0}$.

The upstream and downstream flow profiles are connected through the Rankine-Hugoniot jump conditions that conserve mass, momentum, and energy across the shock. To account for nuclear dissociation during initialization, the equation of energy conservation (e.g., Landau & Lifshitz 1987) at $r = r_{s0}$ is modified to read

$$\frac{1}{2}v_1^2 + \frac{\gamma}{\gamma - 1} \frac{p_1}{\rho_1} = \frac{1}{2}v_2^2 + \frac{\gamma}{\gamma - 1} \frac{p_2}{\rho_2} + \varepsilon. \quad (2.9)$$

Here the subscripts 1 and 2 label the upstream and downstream flow variables, and the expression for the specific internal energy of a polytropic gas has been used, $e_{\text{int}} = (p/\rho)/(\gamma - 1)$. This yields a compression factor (Thompson, 2000)

$$\kappa \equiv \frac{\rho_2}{\rho_1} = (\gamma + 1) \left[(\gamma + \mathcal{M}_1^{-2}) - \sqrt{(1 - \mathcal{M}_1^{-2})^2 + (\gamma^2 - 1) \frac{2\varepsilon}{v_1^2}} \right]^{-1}, \quad (2.10)$$

which reduces to $\kappa \rightarrow (\gamma + 1)/(\gamma - 1)$ for $\mathcal{M}_1 \rightarrow \infty$ and $\varepsilon = 0$. Increasing ε increases the compression factor and decreases the post-shock Mach number. For the models that include NSE abundances, the dissociation energy at the shock is obtained from equation (2.14) using $X_{\text{O}} = 1$ and $X_{\alpha} = 0$ upstream of the shock:

$$\varepsilon(t = 0) = \varepsilon_{\text{O}} + (1 - X_{\alpha}^{\text{eq}}[\rho_2, p_2]) \varepsilon_{\alpha}. \quad (2.11)$$

Figure 2.1 shows how $\varepsilon(t = 0)$ and X_{α}^{eq} depend on the shock radius r_{s0} , for upstream flows composed² of pure ^{16}O and ^{56}Fe , and for different values of \dot{M} . The dissociation energy is approximately constant inside ~ 75 km, where the downstream flow is composed of free nucleons, but decreases at greater distances, remaining $\sim 40\%$ of the gravitational binding energy at the shock. The mass fraction of α -particles reaches 50% at $r = 150\text{--}175$ km, with a weak dependence on \dot{M} .

The initial flow downstream of the shock is obtained by solving the time-independent continuity, Euler, and energy equations in spherical symmetry, including the energy source terms described in §2.2.2. The details of this can be found in Appendix B.

²In the case where the upstream flow is pure ^{56}Fe , we replace ε_{O} in eq. (2.11) with $\varepsilon_{\text{Fe}} = Q_{\text{Fe}}/m_{\text{Fe}} \simeq 0.093M_{1.3}^{-1}(r/150 \text{ km})v_{\text{ff0}}^2(r)$, and set the electron fraction to $Y_e = 26/56$ in the NSE calculation behind the shock.

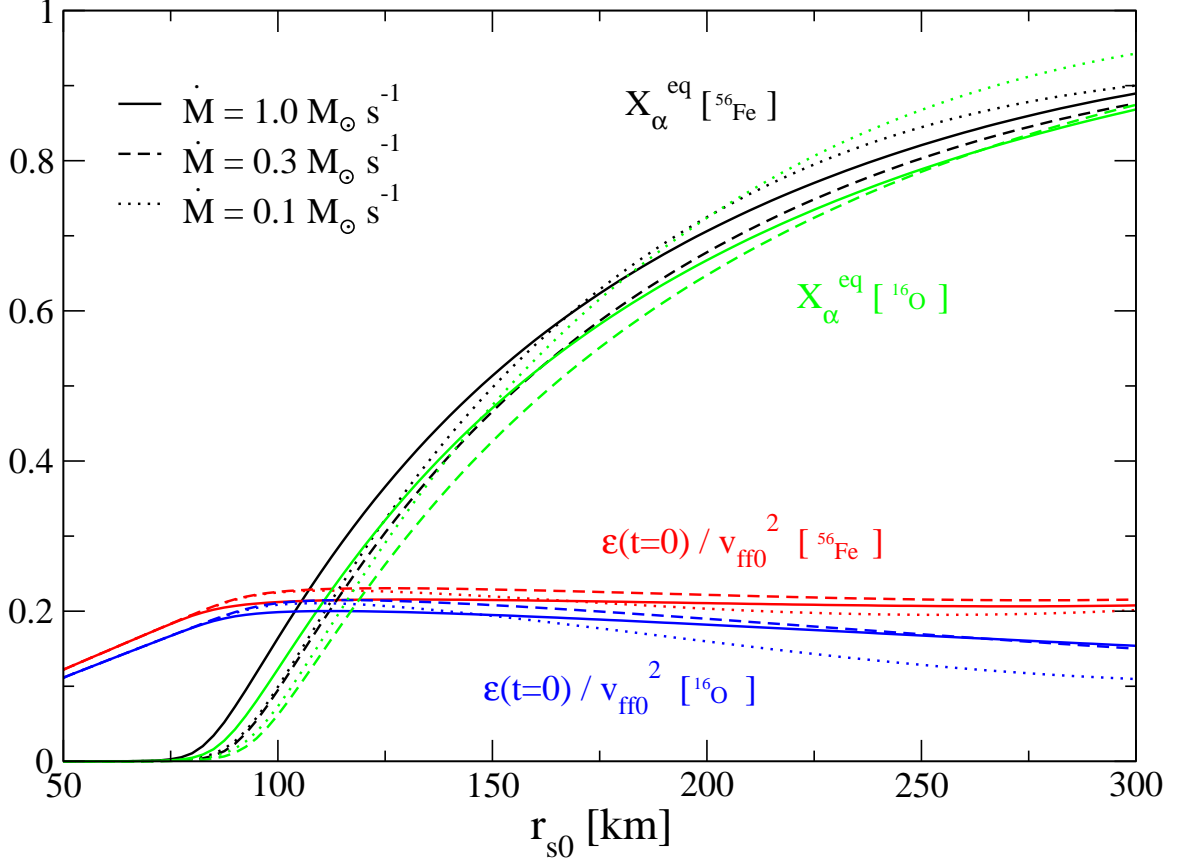


Figure 2.1: Equilibrium mass fraction of α -particles X_{α}^{eq} , and ratio of initial dissociation energy $\epsilon(t=0)$ [eq. 2.11] to v_{ff0}^2 behind a spherical shock positioned at radius r_{s0} . Curves of different shadings correspond to different mass accretion rates. The Rankine-Hugoniot shock jump conditions and dissociation energy are calculated self-consistently, as described in Appendix B. Square brackets refer to the upstream composition of the accretion flow, which for simplicity is taken to be pure ^{56}Fe or ^{16}O . The Mach number upstream of the shock is $\mathcal{M}_1 = 5$, and the central mass is $M = 1.3M_{\odot}$.

In the absence of heating, the steady-state that is obtained is similar in structure to that calculated by Houck & Chevalier (1992) for hyper-Eddington accretion onto a neutron star. For our choice of cooling exponents, and for fixed r_*/r_{s0} and γ , the main effects of increasing ε are an increase in the compression factor κ , a smaller postshock Mach number, and a steepening of the density profile (see Fig. 2.2). In going from $\varepsilon = 0$ to $\varepsilon = 0.25v_{\text{ff}0}^2$, the normalization of the cooling function is decreased by a factor of 127 (keeping r_*/r_{s0} and $\gamma = 4/3$ fixed).

The introduction of heating causes a change in the structure of the initial flow configuration. The radius r_s of the shock in the time-independent solution to the flow equations increases with heating rate; that is, $r_s \geq r_{s0}$. For our explosion calculations, we choose six sequences of models, each with a range of heating parameters $H \geq 0$, and each evolved both in spherical (1D) and axial (2D) symmetry. Their parameters are summarized in Table 2.2. In each sequence, the normalization of the cooling function is chosen so that $r_*/r_s = 0.4$ at zero heating. Three sequences have a constant dissociation energy, which take the values $\varepsilon/v_{\text{ff}0}^2 = \{0.1, 0.15, 0.2\}$. The other three sequences assume NSE below the shock, and have shock radii $r_{s0} = \{50, 75, 125\}$ km at zero heating. This means that the physical value of the cooling radius also takes on different values, namely $\{20, 30, 50\}$ km. In effect, our models are probing different sizes for the neutrinosphere, and different times following the collapse. The other parameters in the NSE models are $M = 1.3M_\odot$ and $\dot{M} = 0.3M_\odot \text{ s}^{-1}$.

For each sequence, Table 2.2 samples some properties of a few models: one with zero heating, another with H close to the critical value for an explosion, and a third with the largest heating parameter that will allow a steady solution. Note that the shock starts out at $\sim 1.3r_{s0}$ in the time-independent, spherical flow solution, and quickly saturates at $\sim (1.8-2)r_{s0}$ in the 2D models with heating just below the threshold for an explosion (see Figure 5.2). The quantity ε/v_1^2 references the dissociation energy to (twice) the kinetic energy of the upstream flow, and is the key free parameter determining the compression

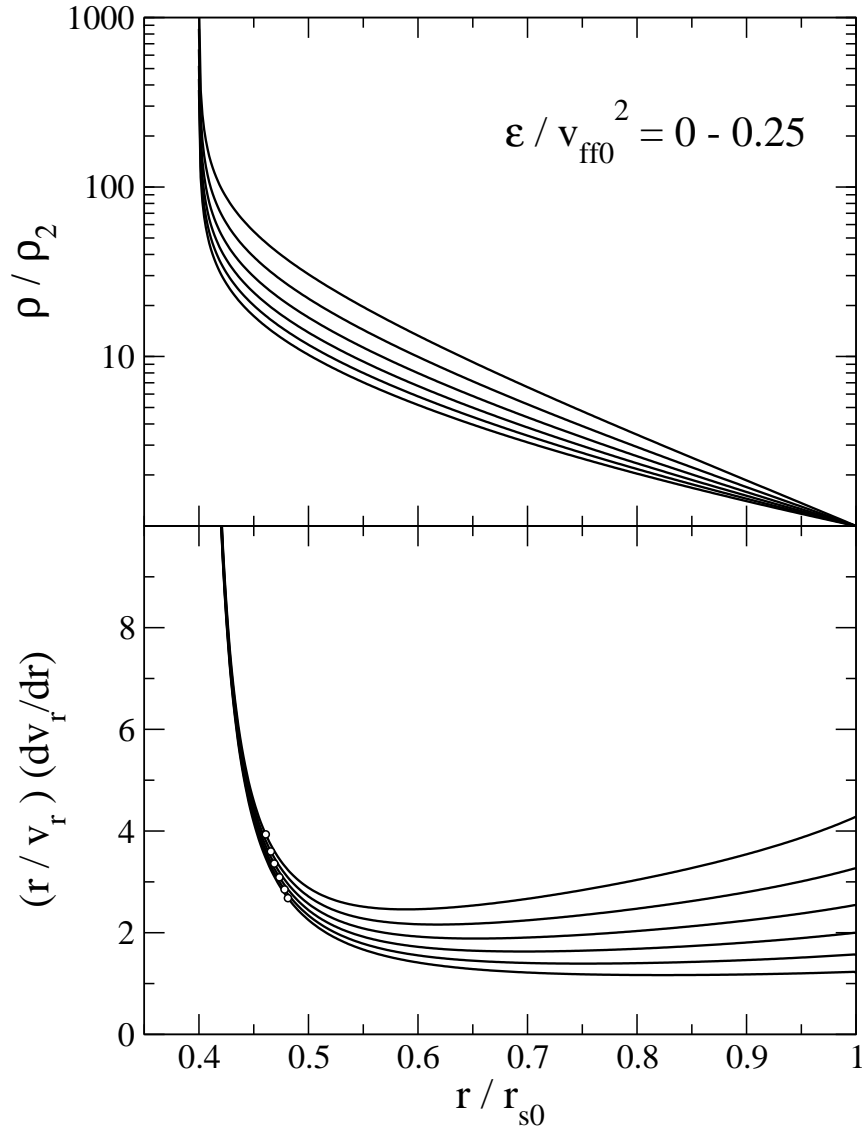


Figure 2.2: Sample initial density profiles normalized to the postshock density ρ_2 (upper panel), and normalized radial velocity gradient (lower panel), for dissociation energies in the range $\varepsilon/v_{\text{ff0}}^2 = [0, 0.25]$ and in the absence of heating. (Higher curves represent larger ε .) Increasing the dissociation energy steepens the density profile as well as strengthening the shock compression. The velocity gradient also becomes stronger just above the cooling layer (white circles denote the radius of maximum sound speed). In this particular sequence, the normalization of the cooling function A is smaller by a factor of 127 when $\varepsilon = 0.25v_{\text{ff0}}^2$ than when $\varepsilon = 0$.

rate κ across the shock (eq. [2.10]).

When examining how the prescription for nuclear dissociation influences the results of simulations with heating, we will focus on the $\varepsilon = 0.15v_{\text{ff0}}^2$ sequence and the NSE sequence with $r_{\text{s0}} = 75$ km, which have similar initial density profiles (due to the low initial α -particle abundance in the NSE model).

The six initial models at zero heating are shown in Fig. 2.3a. Panel (b) shows the sequence of initial models with $r_{\text{s0}} = 75$ km and a range of heating parameters. The model with $H = 0.007v_{\text{ff0}}^3r_{\text{s0}}$ is close to the threshold for an explosion, while the one with $H = 0.009v_{\text{ff0}}^3r_{\text{s0}}$ is well above threshold. At higher values of H , cooling by α -particle dissociation (eq. [2.7]) can be significant in a layer below the shock, causing the density profile to steepen slightly. Fig 2.3c shows how our constant- γ , ideal gas approximation to the internal energy of the flow compares with the full EOS containing finite-temperature and partially degenerate electrons (see Appendix B for details). The curves labeled “+ α ” include our prescription for heating/cooling by α -particle recombination/dissociation, and those labeled “- α ” do not. We show the sequence with the largest shock radius ($r_{\text{s0}} = 125$ km) so that NSE allows some α ’s to be present. The neglect of electron captures below the shock results in an adiabatic index between $4/3$ and $5/3$ in the zone where α -particles are absent. This causes the EOS to stiffen, so that the density profile is well approximated by an ideal gas with $\gamma \simeq 1.48$ at zero heating. Adding in heating tends to flatten the density profile even more, and with $\gamma = 1.48$ it would be much flatter than is typically seen in a realistic core collapse model. Hence we choose an EOS with $\gamma = 4/3$.

2.3.2 Time Dependent Aspects

FLASH2.5 uses a dimensionally split hydrodynamic solver, with source terms applied in an operator split way in between hydrodynamic sweeps (Fryxell et al., 2000). Our computational domain employs spherical polar coordinates, and the grid is uniformly

Table 2.2: Sample Configurations for Explosion Calculations

$\varepsilon/v_{\text{ff}0}^2$	$Hv_{\text{ff}}^{-3}r_{\text{s}0}^{-1}$	$r_{\text{s}}/r_{\text{s}0}$	ε/v_1^2	κ	χ	
0.1	0	1.00	0.10	7.3	0	
	8.00E-3	1.27	0.13	7.7	4.5	
	1.48E-2*	2.57	0.31	11.0	22	
0.15	0	1.00	0.15	8.6	0	
	7.00E-3	1.29	0.20	9.6	9.0	
	1.17E-2*	2.34	0.41	18.9	40	
0.2	0	1.00	0.20	10.1	0	
	5.50E-3	1.30	0.27	12.5	19	
	8.38E-3*	2.08	0.47	34.9	74	
$r_{\text{s}0}$ [km]	$Hv_{\text{ff}}^{-3}r_{\text{s}0}^{-1}$	$r_{\text{s}}/r_{\text{s}0}$	$\varepsilon(t=0)/v_1^2$	κ	χ	$X_{\alpha}^{\text{eq}}(r_{\text{s}})$
50	0	1.00	0.11	7.6	0	5.5E-6
	8.00E-3	1.29	0.15	8.1	5.5	6.1E-5
	1.43E-2*	3.01	0.26	8.6	27	0.43
75	0	1.00	0.17	9.0	0	4.3E-4
	6.50E-3	1.30	0.22	10.1	11	4.5E-2
	1.15E-2*	3.61	0.21	6.8	51	0.83
125	0	1.00	0.21	10.7	0	0.26
	3.50E-3	1.33	0.21	9.9	22	0.51
	7.28E-3*	3.99	0.18	6.1	120	0.99

* No-steady state heating rate (e.g., Burrows & Goshy 1993).

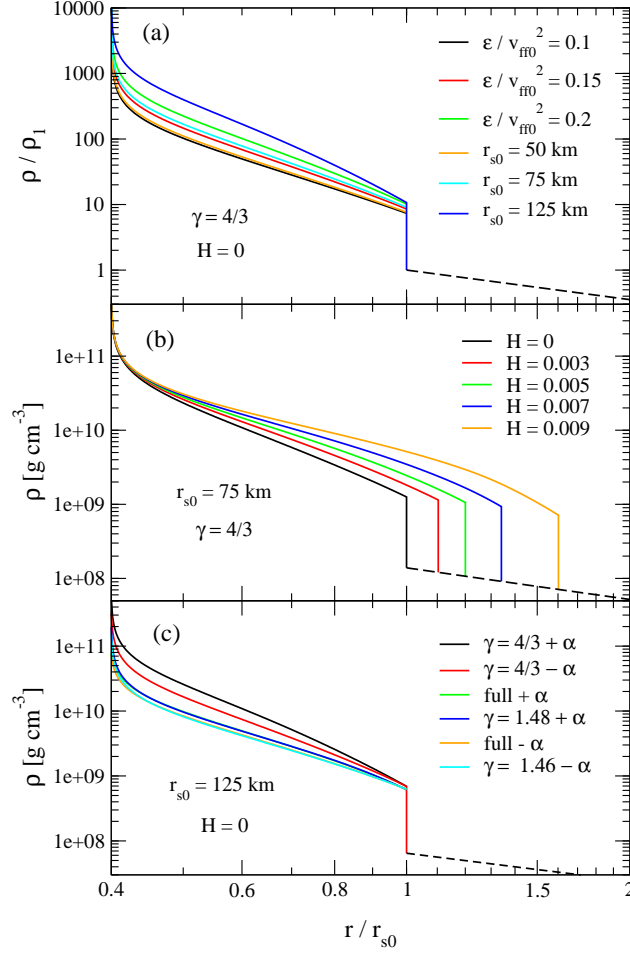


Figure 2.3: Sample initial density profiles, which are solutions to the spherically symmetric and time-independent flow equations. Panel (a) shows the zero-heating configurations for all the sequences shown in Table 2.2. Other parameters are $\gamma = 4/3$, $\mathcal{M}_1(r_{s0}) = 5$ for all configurations, and $\dot{M} = 0.3M_\odot \text{ s}^{-1}$, $M = 1.3M_\odot$ for the NSE models. Panel (b) shows a sequence with a fixed cooling function and range of heating rates (H is given in units of $r_{s0}v_{\text{ff}0}^3$). The dashed line shows the upstream flow. Panel (c) shows a sequence with different equations of state, $r_{s0} = 125$ km, and $H = 0$. The labels “+ α ” and “- α ” mean with and without α -particles included in the EOS, while “full” means that the EOS explicitly includes finite-temperature and partially degenerate electrons, black body photons, and ideal-gas ions. All other parameters are the same as in (a). Only the $\gamma = 4/3$ upstream flow is shown. See Appendix B for further details.

spaced in both r and θ . Two dimensional calculations make use of the full range of polar angles, $\theta = [0, \pi]$. We employ a baseline resolution $\Delta r_{\text{base}} = r_{\text{s0}}/320$ and $\Delta\theta_{\text{base}} = \pi/192$. To better resolve the cooling layer, one extra level of mesh refinement is added to all blocks satisfying $r < r_* + 0.1(r_{\text{s0}} - r_*)$. To avoid excessively large gradients in this region and enhanced cooling due to discreteness effects, we adjust the normalization A of the cooling function to satisfy

$$\left| \sum_i (\mathcal{L}_{H,i} - \mathcal{L}_{C,i} + \mathcal{L}_{\alpha,i}) V_i \right| \simeq 0.995 \left[\frac{GM}{r_*} - \varepsilon(t=0) \right] |\dot{M}|, \quad (2.12)$$

where the sum is taken over the computational cells below the shock at our fixed resolution, V_i is the volume of each computational cell, and the source terms are evaluated at the inner radial cell face. The numerical coefficient on the right hand side depends on the radial resolution, and is chosen empirically to prevent runaway cooling due to discreteness effects in time-dependent calculations. This results in an initial Mach number $\sim 10^{-3} - 10^{-2}$ at the inner boundary. The default FLASH2.5 Riemann solver is used, which we find can support high incident Mach numbers $\mathcal{M}_1 \lesssim 10^2$. We have not witnessed the appearance of the odd-even decoupling instability at the shock (Quirk, 1994), which allows us to avoid using a hybrid Riemann solver. (We find that the hybrid solver in FLASH2.5 has problems for $\mathcal{M}_1 \gtrsim 10$ in our setup.)

In all simulations reported in this paper, we use a reflecting inner boundary in the radial direction. The flow at the outer radial boundary (situated at $7r_{\text{s0}}$ for explosion calculations) is given by the upstream steady state solution. The angular boundaries at $\theta = 0$ and $\theta = \pi$ are also reflecting in 2D simulations. Our choice of a static and reflecting inner boundary is made for computational simplicity. In a real core collapse, the radius of the neutrinosphere decreases with time. The effect of such a dynamic inner boundary on the linear growth of shock perturbations has been examined by Scheck et al. (2008) in a semi-realistic collapse simulation. They found that it facilitated growth by increasing the strength of the velocity gradient above the neutrinosphere. In addition, Burrows et al. (2006) reported evidence for a transient SASI instability in the first 100 ms of their

full 2D collapse simulations. The analysis of the SASI by Scheck et al. (2008), like ours, used a reflecting inner boundary, albeit one positioned inside the neutrinosphere. Our results provide strong evidence that linear growth depends on the structure of the flow between the shock and the cooling layer, which suggests (but does not prove) that a more realistic mass distribution below the cooling layer will not have a large impact on the growth of linear perturbations above the cooling layer. Yamasaki & Yamada (2007) find that a zero-gradient inner boundary condition ($d\delta v_r/dr = 0$) has a quantitative but not a qualitative effect on the form of the linear eigenmodes.

At our baseline resolution, the accretion flow in 2D remains spherically symmetric for several tens or even hundreds of dynamical times at the shock. To excite specific oscillatory modes of the shock, we introduce an overdense shell in the flow upstream of the shock, with an angular dependence given by a Legendre polynomial of a single order ℓ . In the absence of this perturbation, the flow still experiences a small startup error that is composed of two spherically symmetric transients: an outgoing sound wave due to the finite (albeit small) Mach number at the inner reflecting boundary, and an ingoing entropy wave due to the initial discontinuity at the shock (see, e.g., Leveque 1998). Since these initial transients do not affect non-spherical modes, we made no attempt to suppress them by increasing the numerical dissipation (as is done by Blondin et al. 2003 and Blondin & Mezzacappa 2006), and instead use PPM in its default FLASH2.5 configuration [see Colella & Woodward (1984); Fryxell et al. (2000) for details]. The spherical transients can be minimized (but never completely eliminated) by locally increasing the resolution at the shock, and by simultaneously decreasing the innermost Mach number and increasing resolution at the inner boundary. To trigger convection below the shock, we introduce random cell-to-cell velocity perturbations in v_r and v_θ at $t = 0$, with an amplitude 1% of the steady state radial velocity.

For the adopted scaling of our cooling function \mathcal{L}_C with p and ρ , the ratio of cooling time to flow time decreases with decreasing entropy. The post-shock fluid then undergoes

runaway cooling in time-dependent simulations, and the shock collapses within a few sound crossing times. We have therefore implemented a cutoff in entropy in the net energy source term due to neutrinos,

$$\mathcal{L}_{\text{net}} = (\mathcal{L}_H - \mathcal{L}_C) \exp[-(s/s_{\text{min}})^2], \quad (2.13)$$

where \mathcal{L}_H and \mathcal{L}_C are the heating and cooling functions without cutoff (eq. 2.5 and 2.6), respectively, $s = (\gamma - 1)^{-1} \ln(p/\rho^\gamma)$ an entropy function, and s_{min} the value of s at $r = r_*$ that is obtained in the initial solution using $\mathcal{L}_{\text{net}} = (\mathcal{L}_H - \mathcal{L}_C)$. The result is that the accreted fluid accumulates in the first few computational cells outside r_* , with a minimal modification in the outer post-shock flow structure.

In models implementing NSE abundances, a specific energy

$$e_{\text{nuc}} = -X_{\text{O}}(\varepsilon_{\text{O}} + \varepsilon_{\alpha}) - (X_{\alpha} - X_{\alpha}^{\text{eq}}[\rho, p]) \varepsilon_{\alpha}, \quad (2.14)$$

is either released to or absorbed from the internal energy of the fluid below the shock within a single time step (it can be of either sign). Here X_{O} is non-vanishing only for fluid elements that have just passed across the shock, and we have set $X_{\text{O}}^{\text{eq}} = 0$. The quantity (2.14) is introduced as an energy source term in FLASH, and from it one readily obtains a rate of release of nuclear binding energy per unit mass,

$$\frac{de_{\text{nuc}}}{dt} \equiv \frac{e_{\text{nuc}}}{\Delta t}, \quad (2.15)$$

where Δt is the simulation time step. For constant dissociation runs, we set $X_{\alpha} = X_{\alpha}^{\text{eq}} = 0$ below the shock at all times and leave the total dissociation energy $\varepsilon = \varepsilon_{\text{O}} + \varepsilon_{\alpha}$ as a free parameter, so that eq. (2.14) is always a sink term at the shock, $e_{\text{nuc}} = -X_{\text{O}}\varepsilon$. We aim to choose a threshold for “burning” (that is, nuclear dissociation) which maintains a composition of nearly 100% heavy nuclei upstream of the shock, and 100% α -particles and nucleons downstream. The composition of the fluid is divided this way in the initial condition, with all fluid injected at later times through the outer radial boundary being

entirely heavy nuclei. Details of our implementation of nuclear burning and modifications to the original FLASH2.5 module are discussed in Appendix C.

An explosion is defined as either i) a collision between the shock and the outer boundary of the simulation volume ($r = 7r_{s0}$) within $1000t_{\text{ff0}}$ of the start of the simulation; or ii) in the special case of the 1D constant- ε models, a transient expansion that breaks a quasi-steady pattern within the same timeframe (see §5.2). Even in the 1D simulations, very small changes in heating rate can lead to dramatic changes in shock behavior, and so this definition of explosion is good enough for our purposes.

Potential numerical instabilities result from a combination of a high cooling rate and a low Mach number in the cooling layer. We find that the time integration is stable when the cutoff (2.13) is imposed on \mathcal{L}_{net} , because the cooling time is never smaller than the Courant time. (FLASH2.5 automatically restricts the timestep so as to satisfy the Courant-Friedrichs-Levy condition.) Our implementation of nuclear dissociation also avoids introducing instabilities, since the energy extracted from the flow in one time step is kept smaller than the internal energy (Appendix C).

The hydrodynamics module in FLASH has undergone extensive testing (Calder et al., 2002), and so we focus our efforts on verifying our setup and on the interaction of the different physics modules with the hydrodynamic solver. The most basic and complete test we can think of is the reproduction of the linear growth rates of the SASI. The results are given in the next chapter. We have tested the implementation of our NSE model by verifying that, in the absence of initial perturbations, our steady state initial conditions remain steady. Spherical transients present in the initial data die out in a few $\ell = 0$ oscillation cycles, and are present even when nuclear burning is omitted.

2.4 Diagnostic Methods

2.4.1 Procedure for Obtaining SASI Eigenfrequencies from a Hydrodynamical Simulation

To excite a particular SASI mode in our simulations, we add an overdense shell upstream of the shock with the desired angular dependence and a sinusoidal radial profile (amplitude $\sim 10\%$, width $\sim 0.2r_{s0}$). This generates an initial shock displacement with very small amplitude (negligible compared with the spherically symmetric displacement described in § 2.3.2), followed by a growth of the SASI mode on the advection timescale.

To measure the growth rate ω_{grow} and oscillation frequency ω_{osc} of a mode associated with a given Legendre- ℓ , we project the shock surface onto the corresponding Legendre polynomial, obtaining a time-dependent Legendre coefficient,

$$a_\ell(t) = \frac{2\ell + 1}{2} \int_0^\pi R_s(\theta, t) P_\ell(\theta) \sin \theta d\theta, \quad (2.16)$$

where P_ℓ is the Legendre polynomial and $R_s(\theta, t)$ is the shock surface, defined as the locus of points with pressure $p_{\text{shock}} = \sqrt{p_1 p_2}$. For the strong shock simulations, this has a numerical value $p_{\text{shock}} \simeq 0.01\rho_1 v_{\text{ff0}}^2$.

The time-dependent Legendre coefficient is then fitted with the functional form

$$a_\ell(t) = c_1 + c_2 e^{\omega_{\text{grow}} t} \sin(\omega_{\text{osc}} t + c_3) + c_4 t, \quad (2.17)$$

where ω_{grow} is the growth rate, ω_{osc} the oscillation frequency, and the c_i are constants. This fitting function works well whenever there is only a single unstable harmonic, usually the fundamental, for a given ℓ (see, e.g., lower-left panel in Fig. 4.2 during the first $\sim 100t_{\text{ff0}}$). The fitting is performed with a Levenberg-Marquardt algorithm (Press et al., 2006).

For the fitting we choose a temporal range that begins when the Legendre coefficient starts a clean sinusoidal oscillation, and which ends when $a_\ell(t) = (r_{s0} - r_*)/10$ for $\ell \geq 1$,

corresponding to a shock displacement of 10% of the unperturbed value at the poles. Our temporal sampling interval is $t_{\text{ff0}}/2$, about a quarter of the radial sound crossing time from r_* to r_{s0} .

To estimate the uncertainty in the fitted eigenfrequencies, we assign a ‘‘measurement error’’ to $a_\ell(t)$, which we compute as follows. The error in $R_s(\theta, t)$ is taken to be one-half the size of the baseline resolution, $\Delta r_{\text{base}}/2$. The size of the angular cell $\Delta\theta_{\text{base}}$ enters through the computation of the integral in eq. (2.16) as a discrete sum. Errors adding up in quadrature then yield

$$\delta a_\ell = \frac{2\ell + 1}{4} \Delta r_{\text{base}} \Delta\theta_{\text{base}} \sqrt{\sum_i P_\ell^2(\theta_i) \sin^2 \theta_i}, \quad (2.18)$$

where the sum is performed over all the angular cells. This result is then used as the input error in the Levenberg-Marquardt algorithm. The error bars shown in Fig. 3.2 are the 1-sigma errors that output from the fitting routine, multiplied by 3.

2.4.2 Linear Stability Analysis with Nuclear Dissociation Downstream of the Shock

Foglizzo et al. (2007) formulate SASI eigenvalue problem assuming a constant- γ ideal gas equation of state. Generalizing this formalism to account for a constant dissociation energy ε is straightforward when thermal energy is removed from the flow only immediately below the shock. The background flow solution is modified, but the algebraic form of the perturbation equations is not. We therefore use the differential system given in eqns. (10)-(13) of Foglizzo et al. (2007), which employs the variables

$$f = v_r \delta v_r + \frac{2c_s \delta c_s}{(\gamma - 1)}, \quad (2.19)$$

$$h = \frac{\delta(\rho v_r)}{\rho v_r}, \quad (2.20)$$

$$\delta S = \frac{1}{\gamma - 1} \left(\frac{\delta p}{p} - \gamma \frac{\delta \rho}{\rho} \right), \quad (2.21)$$

$$\delta K = r^2 \mathbf{v} \cdot (\nabla \times \delta \boldsymbol{\omega}) + \ell(\ell + 1) \frac{c^2}{\gamma} \delta S, \quad (2.22)$$

where $\boldsymbol{\omega} = \nabla \times \mathbf{v}$. All quantities are projected onto spherical harmonics Y_ℓ^m . A complex eigenvalue $\omega \equiv \omega_{\text{osc}} + i\omega_{\text{grow}}$ is obtained by enforcing $\delta v_r = 0$ at $r = r_* + 10^{-4}(r_{s0} - r_*)$. The eigenfrequencies obtained are nearly insensitive to the radius at which this boundary condition is applied, so long as it lies inside the cooling layer.

A subtlety in the treatment of the boundary conditions at the shock is worth discussing. When the shock is perturbed to a position $r_{s0} + \Delta r$ and velocity Δv , the equation of energy conservation across the discontinuity becomes

$$\frac{1}{2}(v_1 - \Delta v)^2 + \frac{c_{s1}^2}{\gamma - 1} = \frac{1}{2}(v_2 + \delta v_r - \Delta v)^2 + \frac{\gamma}{\gamma - 1} \left(\frac{p_2}{\rho_2} + \frac{\delta p_2}{\rho_2} - \frac{p_2 \delta \rho_2}{\rho_2^2} \right) + \frac{\partial \varepsilon}{\partial \rho} \delta \rho_2 + \frac{\partial \varepsilon}{\partial p} \delta p_2. \quad (2.23)$$

Here, as before, 1 and 2 label the upstream and downstream flows in the frame of the accretor. When $\varepsilon = \text{constant}$, the algebraic form of this equation is unchanged from the case $\varepsilon = 0$. Although the Bernoulli parameter b of the background flow below the shock is reduced, the perturbation $f = \delta b$ does not receive additional terms. The boundary conditions on f , h , δS , and δK therefore have the same algebraic form as eqns. (B10)-(B12), (A6) and (B15) of Foglizzo et al. (2007). By contrast, the shock boundary conditions on the perturbation variables $\delta \rho_2$, δp_2 and δv_r do acquire additional terms resulting from the changing compression ratio κ (eq. [2.10]). We have checked that these additional terms cancel out in the boundary conditions on f , h , δS , and δK .

To account for heating and our entropy cutoff (eq. 2.13) in the linear stability calculation, one needs to add additional terms to the perturbation to the cooling term in the energy equation (eq. A7 of Foglizzo et al. 2007),

$$\delta \left(\frac{\mathcal{L}_{\text{net}}}{\rho v_r} \right) = \left\{ \left(\frac{\mathcal{L}_H}{\rho v_r} \right) \frac{\delta \rho}{\rho} - \left(\frac{\mathcal{L}_C}{\rho v_r} \right) \left[\beta \frac{\delta \rho}{\rho} + \alpha \frac{\delta c^2}{c^2} \right] \right\} e^{-(s/s_{\text{min}})^2} - \left(\frac{\mathcal{L}_{\text{net}}}{\rho v} \right) \left[\frac{\delta \rho}{\rho} + \frac{\delta v_r}{v_r} + 2 \frac{s}{s_{\text{min}}^2} \right]. \quad (2.24)$$

The precise analytic eigenfrequencies are somewhat sensitive s_{min} , so this parameter needs to be the same in both linear stability and simulation for proper comparison. The difference between including and excluding the entropy cutoff in the linear stability can

be seen from Fig. 3.1, where results obtained without entropy cutoff are shown as dashed lines.

2.4.3 Residency Time

In order to track the residency time of the fluid in the gain region, we assign a scalar to each spherically symmetric mass shell in the upstream flow. This scalar is passively advected by FLASH2.5. Through this technique, we are able to assign a “fluid” time to each element in the domain, corresponding to the time at which the mass shell would cross the instantaneous angle averaged shock position if advected from the outer boundary at the upstream velocity:

$$t_F = t_{\text{OB}} + \int_{\langle r_s(t) \rangle_\theta}^{r_{\text{OB}}} \frac{dr}{|v_r|}. \quad (2.25)$$

Here t_{OB} is the time at which the fluid enters through the outer radial boundary at $r = r_{\text{OB}}$, and $\langle r_s(t) \rangle_\theta$ is the angle averaged shock position. Initially, $t_{\text{OB}} = 0$ and all the fluid below the shock is set to $t_F = 0$. This prescription works well for statistical studies (§5.3.2), tracing large scale fluid patches, despite some inevitable turbulent mixing among neighboring fluid parcels.

Chapter 3

Linear Phase of the SASI

3.1 Overview

In this chapter, we focus on the linear growth of perturbations of the accretion flow below the shock. Previous investigations of the linear Standing Accretion Shock Instability (SASI) have employed simplified physical models (Blondin & Mezzacappa, 2006; Foglizzo et al., 2007; Laming, 2007), or made use of semi-realistic simulations (Yamasaki & Yamada, 2007; Ohnishi et al., 2006; Scheck et al., 2008) to measure its rate of growth and oscillation frequency. The presence of the linear instability in more realistic simulations is not clear, however, given the highly nonlinear behavior of the system (e.g., Buras et al. 2006b,a; Burrows et al. 2007b). Nevertheless, it is of interest to gain a better understanding of the physical mechanism driving an intrinsic fluid instability of the accretion shock (that is, independent of convective motions), and studying its development from a laminar accretion flow. A study of the non-linear phase of the instability is deferred to Chapter 4.

The nature of the linear instability mechanism has been clearly demonstrated in the WKB regime (Foglizzo et al., 2007): the growth of higher radial overtones is due to the “advective-acoustic” cycle first described by Foglizzo & Tagger (2000). This cycle involves

a non-spherical deformation of the shock, which creates entropy and vortex waves in the downstream flow. These perturbations become partly compressive as they are advected toward the star, thereby creating an outgoing sound wave that interacts with the shock. There is growth if the secondary shock oscillation is larger in amplitude than the initial perturbation. The instability is aided if the flow is strongly decelerated somewhere below the shock. There is no purely acoustic instability.

The linear stability analysis of Foglizzo et al. (2007) found approximate agreement with the real frequencies and growth rates measured in the axisymmetric hydrodynamical simulations of Blondin & Mezzacappa (2006) – which involve low-order modes of the shock – and good agreement for the $\ell = 0$ modes in particular. Yamasaki & Yamada (2007) solved the eigenvalue problem in an accretion flow with a realistic equation of state and strong neutrino heating. They also found that the eigenfrequencies most closely matched the advective-acoustic cycle. Hydrodynamical simulations show that the oscillation period scales with the advection time at moderate to large shock radius (Ohnishi et al., 2006; Scheck et al., 2008).

The mechanism driving fundamental, low order angular modes of the flow has not yet been conclusively found. These modes happen to be the most unstable ones, having the greatest influence on the symmetry of the flow. In addition, the effects of a finite rate of nuclear dissociation at the shock on the instability have not yet been studied in isolation. The increased density jump and low Mach number of the flow are expected to have an important effect on the modes of the flow regardless of whether they involve advected or purely acoustic perturbations.

In what follows, we examine the linear phase of the SASI in three steps. First, we show detailed agreement between eigenfrequencies measured from our time-dependent hydrodynamic simulations with those from a solution to the modified linear stability analysis of Foglizzo et al. (2007) over a moderate parameter range (§3.2). We then use this verified linear stability calculation to explore the effects of nuclear dissociation,

incident Mach number, and adiabatic index on the eigenmodes over a wider parameter range (3.3). We finally use the eigenmode calculation to further probe the mechanism behind the fundamental modes of the flow, by looking at the dependence of the growth rate on the characteristic timescales of the flow (3.4). A summary of the most important results of this chapter follows in §3.5.

3.2 Comparison of Hydrodynamical Simulation and the Solution to the Eigenvalue Problem

Our method for generating a perturbation and measuring its growth in a hydrodynamical simulation is described in §2.4.1; and our method for calculating the linear eigenmodes of the accretion flow is summarized in §2.4.2. The three basic parameters of the flow are the ratio r_*/r_{s0} of cooling radius to shock radius, the adiabatic index γ , and the dissociation energy $\varepsilon/v_{\text{ff0}}^2$.

It is possible to make a clean measurement of an individual SASI mode in a hydrodynamical simulation when the fundamental is the only unstable mode (at a given ℓ). We have run simulations both in regions of parameter space where this condition is satisfied – as predicted by linear stability analysis – and where it is not. The presence of unstable overtones can be gleaned from the time evolution of a particular coefficient in the Legendre expansion of the shock radius, which deviates from a sinusoid of exponentially increasing amplitude.

First we reconsider the stability of the zero-energy accretion flow ($\varepsilon = 0$), and specialize to an adiabatic index $\gamma = 4/3$. In the parameter range relevant to core-collapse supernovae, we find that the most unstable modes are $\ell = 1$ and $\ell = 2$, in agreement with the work of Blondin & Mezzacappa (2006) and Foglizzo et al. (2007). The eigenvalue analysis of Foglizzo et al. (2007) correctly predicts the location of critical stability points of the fundamental and first radial overtone, for $\ell = 0 - 3$. We have also solved the dif-

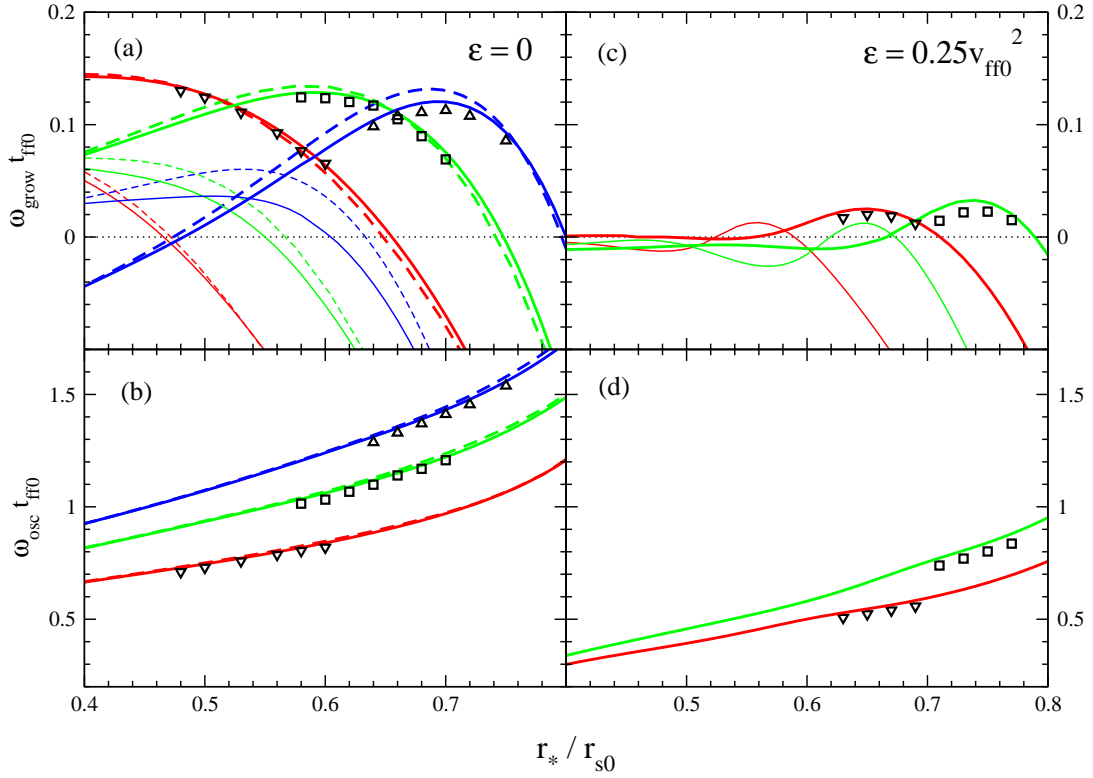


Figure 3.1: Growth rates ω_{grow} (upper panels) and oscillation frequencies ω_{osc} (lower panels) of the SASI, in units of inverse free-fall time at the shock, versus the ratio of stellar radius to shock radius r_*/r_{s0} . In the left panels, the unperturbed flow has zero energy flux ($\varepsilon = 0$) and upstream Mach number $\mathcal{M}_1 \simeq 87$. In the right panels, specific internal energy $\varepsilon = 0.25v_{\text{ff0}}^2$ is removed from the flow just below the shock; and $\mathcal{M}_1 = 5$. The lines give the solution to the eigenvalue problem of Foglizzo et al. (2007) for different spherical harmonics: $\ell = 1$ (red), $\ell = 2$ (green), and $\ell = 3$ (blue), with thick lines representing the fundamental mode and thin lines the first radial overtone. The dashed lines show the effect of neglecting the cutoff in the cooling function (eq. [2.13]). (See §2.4.2 for details.) Symbols show the eigenfrequencies obtained from time-dependent hydrodynamic simulations: for $\ell = 1$ (down-triangles), $\ell = 2$ (squares), and $\ell = 3$ (up-triangles). Uncertainties in the fitted parameters are smaller than the symbol size. (See §2.4.1 for details.)

ferential system of Houck & Chevalier (1992), finding that not only the critical stability points but also the growth rates do not agree with what we measure in our simulations (although results for $\ell = 0$ are identical to those of Foglizzo et al. 2007). In the remainder of this subsection, we refer to simulation results for which only the fundamental is unstable.

The left panels of Fig. 3.1 show growth rates and oscillation frequencies¹ for the modes $\ell = 1, 2, 3$, in the case where the flow upstream of the shock has a high Mach number $\mathcal{M}_1 \approx 87$. There is very good agreement between the calculated eigenfrequencies and the output of the hydrodynamic simulation: $1 - 3\%$, $1 - 2\%$, and $1 - 2\%$ for the real frequencies of the $\ell = 1, 2$, and 3 modes, respectively, and $2 - 4\%$, $2 - 8\%$, and $5 - 8\%$ for the growth rates. Our method for estimating the uncertainty in the measured mode frequencies is detailed in §2.4.1. The most important systematic errors arise from the discreteness of the mesh, the discrete summation involved in the Legendre projection, and the discrete time sampling. The error bars are comparable to or smaller than the size of the symbols in Fig. 3.1, typically $\delta\omega t_{\text{ff0}} \sim 5 \times 10^{-3}$.

The agreement between the two methods of calculating the growth rates becomes worse at larger ℓ . We attribute this to the better sampling of the lower- ℓ modes by the grid, which results in weaker numerical dissipation. (The effects of numerical dissipation in PPM typically depend on the ratio of cell width to wavelength: Porter & Woodward 1994.)

When the dissociation energy is increased to $\varepsilon = 0.25v_{\text{ff0}}^2$, the agreement between the two calculational methods is reduced a bit, to $4 - 5\%$ for the oscillation frequencies for both $\ell = 1$ and $\ell = 2$, and $18 - 30\%$ and $20 - 42\%$ for the growth rates, respectively.² A more extensive exploration of the influence of finite ε and a reduced upstream Mach

¹We have chosen to plot eigenfrequencies in units of the inverse free-fall time t_{ff0} at r_{s0} , since this is directly related to simulation time when both the stellar mass and the shock radius are held fixed.

²The absolute value of the discrepancy between the two sets of growth rates is similar to that found for $\varepsilon = 0$, namely $(10^{-3} - 10^{-2})t_{\text{ff0}}^{-1}$.

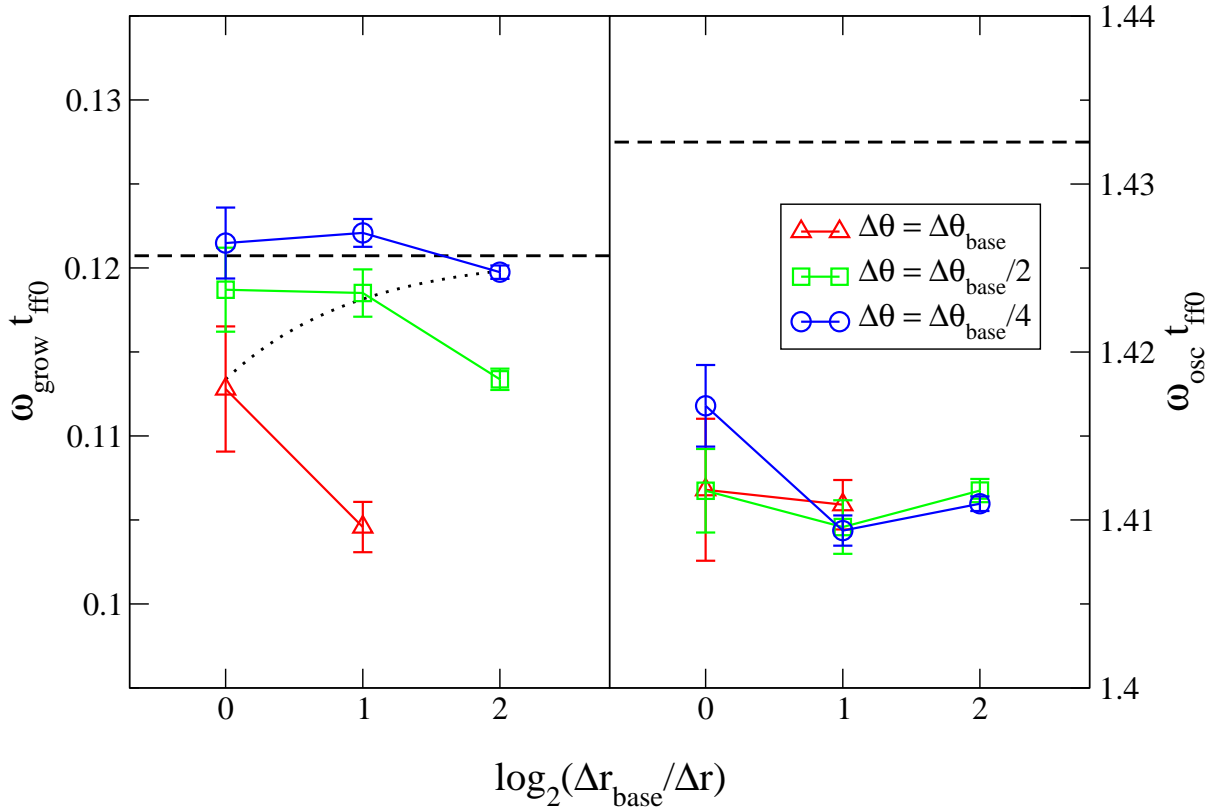


Figure 3.2: Growth rates (left) and oscillation frequencies (right) as a function of resolution, for the $\ell = 3$ mode in a flow with $r_*/r_{s0} = 0.7$ (see panels a,b of Fig. 3.1). The dashed line in each panel shows the solution to the linear stability problem, and symbols represent measurements from hydrodynamical simulations at different radial and angular resolutions. See §2.3.2 for a description of the grid spacing, and §2.4.1 for an explanation of the error bars. The dotted line shows the best power-law fit to the difference of growth rate error on resolution: $\Delta\omega_{\text{grow}} \propto (\Delta r \Delta\theta)^{-0.75 \pm 0.10}$.

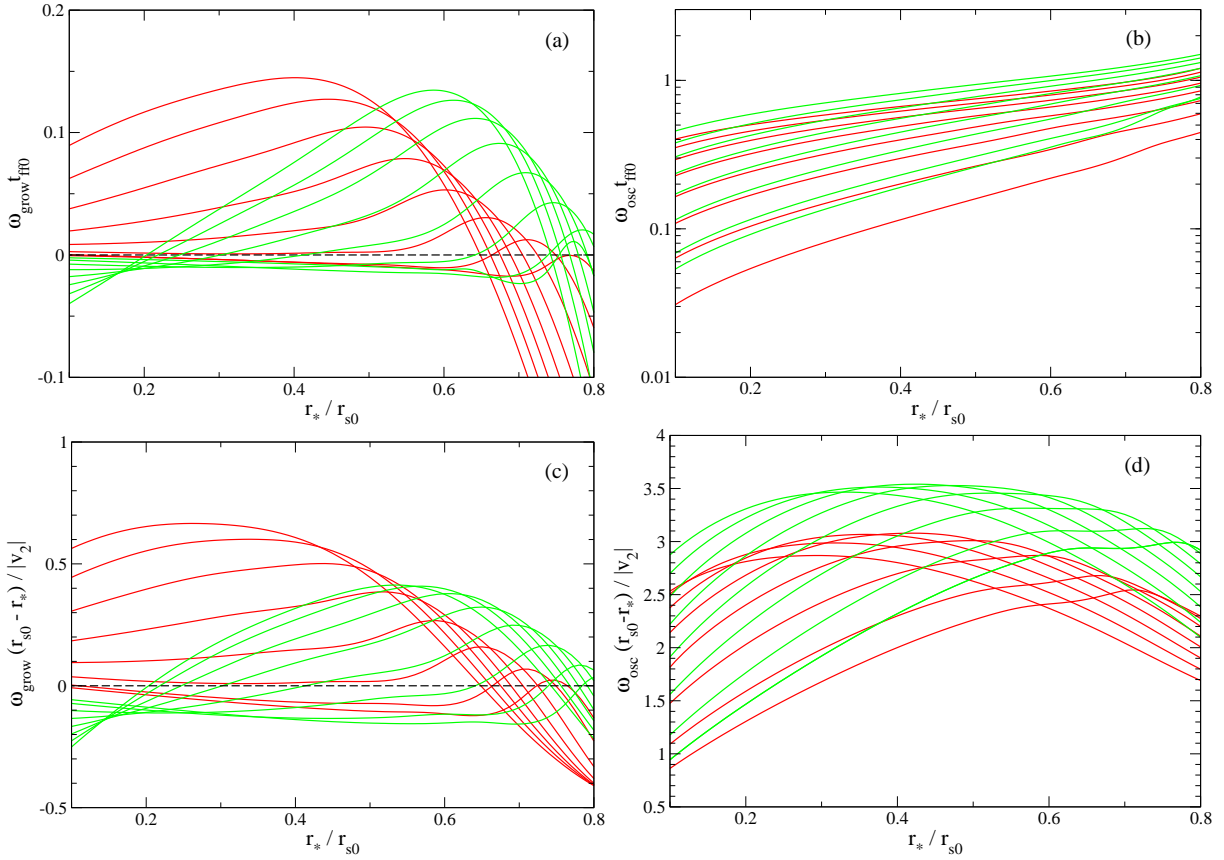


Figure 3.3: Growth rates (left) and oscillation frequencies (right) of the fundamental $\ell = 1$ (red) and $\ell = 2$ (green) modes as a function of r_*/r_{s0} , for dissociation energies $\varepsilon/v_{\text{ff0}}^2 = 0, 0.05, 0.1, 0.15, 0.2, 0.25, 0.3, \text{ and } 0.33$. Panels (a) and (b) show eigenfrequencies in units of the inverse free-fall timescale t_{ff0} . Lower curves correspond to higher dissociation energy. Panels (c) and (d) show the same curves, but in units of the inverse of the time required to traverse the postshock cavity at the postshock speed, $(r_{s0} - r_*)/|v_2|$. In panel (d), increasing dissociation makes the peak of the curves move to the right. Other parameters of the sequence are $\gamma = 4/3$ and $\mathcal{M}_1 \rightarrow \infty$. See text for description.

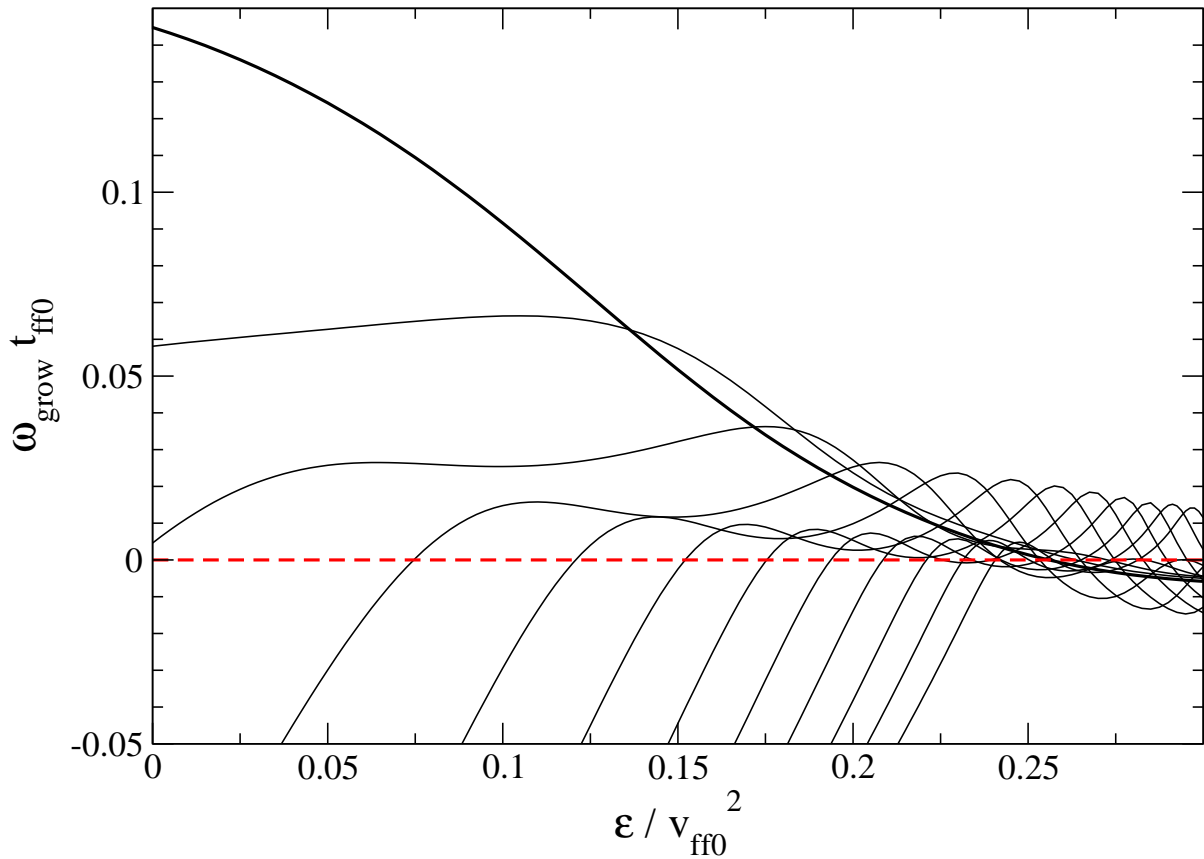


Figure 3.4: Radial overtones of the $\ell = 1$ mode as a function of nuclear dissociation energy ε . The bold line denotes the fundamental mode, and the thin lines the first 11 overtones. Other parameters are $r_*/r_{s0} = 0.4$, $\gamma = 4/3$, and $\mathcal{M}_1 \rightarrow \infty$. Even though nuclear dissociation significantly decreases the growth rate, there is always an unstable overtone.

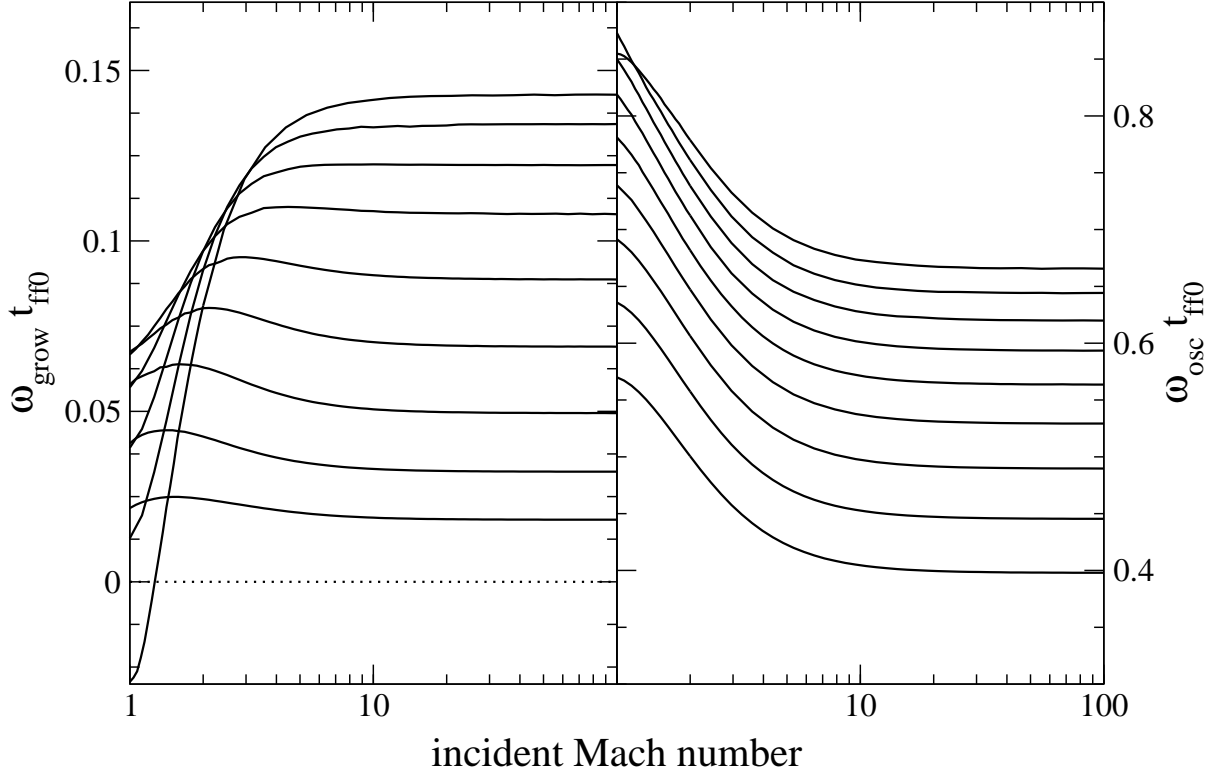


Figure 3.5: Growth rates (left) and oscillation frequencies (right) of the fundamental $\ell = 1$ mode as a function of incident Mach number, for $\varepsilon/v_{\text{ff0}}^2 = 0, 0.025, 0.05, 0.075, 0.1, 0.125, 0.15, 0.175,$ and 0.2 , with decreasing curves for higher dissociation energy. Other parameters are $r_*/r_{s0} = 0.4$ and $\gamma = 4/3$. Eigenfrequencies are modified significantly when $\mathcal{M}_1 \lesssim 5$. The normalization of the cooling function A is bigger by a factor 4 – 5 for $\mathcal{M}_1 = 2$ relative to $\mathcal{M}_1 = 100$ throughout the range in ε .

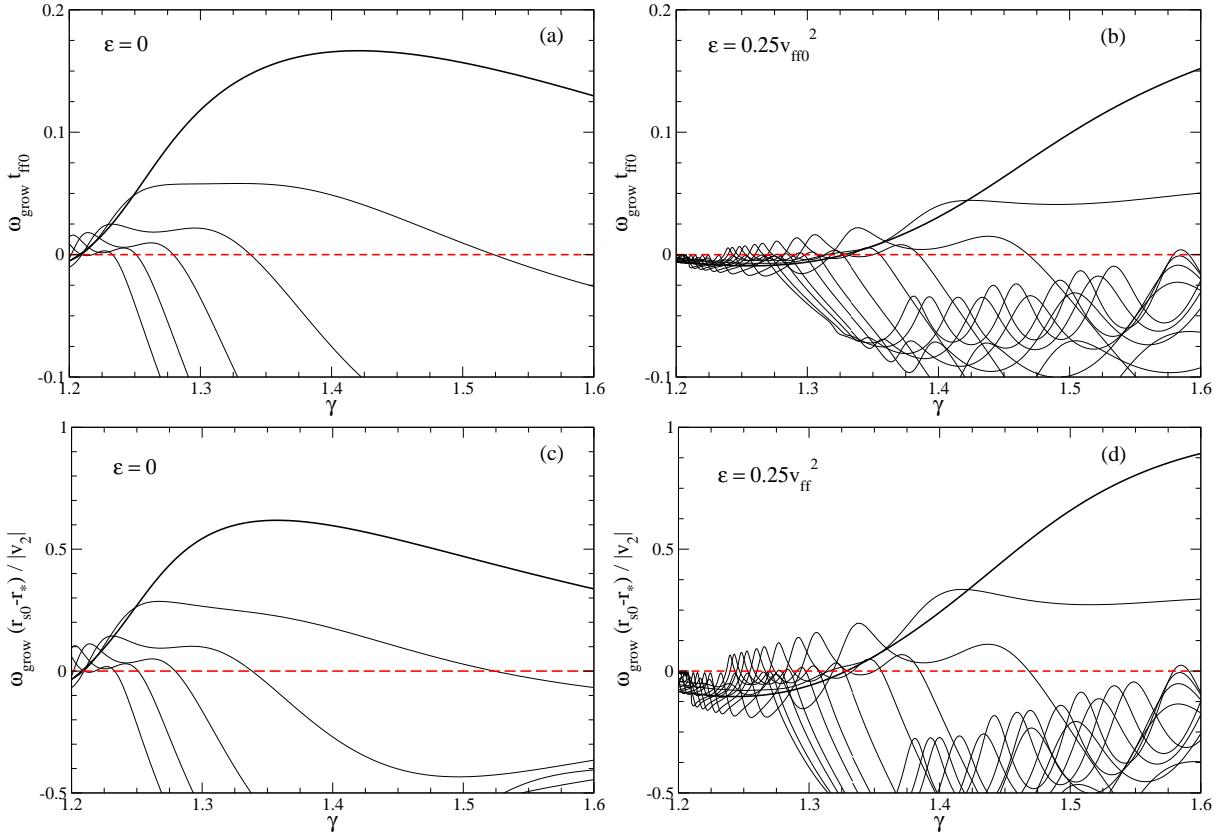


Figure 3.6: Radial overtones of the $\ell = 1$ mode as a function of adiabatic index γ , for a vanishing energy accretion flow [$\varepsilon = 0$, panels (a) and (c)] and a flow with internal energy $\varepsilon = 0.25v_{\text{ff0}}^2$ removed below the shock [panels (b) and (d)]. The upper row shows results in units of the inverse free-fall time t_{ff0} , whereas the lower row shows eigenfrequencies in units of the inverse of the time required to traverse the shock cavity at the postshock velocity, $(r_{\text{s0}} - r_*)/|v_2|$. The bold line denotes the fundamental mode, the thin lines the first 5 (a,c) and 11 (b,d) overtones. Growth rates generally decrease toward smaller γ , but there is always an unstable overtone. This qualitative result is independent of the size of the density jump at the shock. Other parameters are $r_*/r_{\text{s0}} = 0.4$, $\varepsilon = 0$, and $\mathcal{M}_1 \rightarrow \infty$.

number on the mode frequencies is made in the next subsection. For now, we emphasize the good agreement between analytics and numerics.

We have also checked the effects of resolution. Fig. 3.2 shows results for $r_*/r_{s0} = 0.7$ and $\ell = 3$ [see panels (a) and (b) of Fig. 3.1]. The growth rates show the expected behavior, with increasing agreement between the two methods with increasing radial and angular resolution. We observe a greater sensitivity to the angular width $\Delta\theta$ of the grid cells than to their radial width. The real frequencies show a much weaker trend. In sum, a four-fold decrease in Δr and $\Delta\theta$ improves the agreement in the two sets of growth rates from 7% to 0.8%, while the disagreement in the real frequencies stays nearly constant within uncertainties at 1.5%. Part of this difference in behavior with resolution may be due to the fact that lateral sound waves are involved in setting the growth rate (§3.4), and our baseline grid resolves the radial distances much better than meridional ones, therefore a small improvement in angular resolution leads to significant improvement in the growth rate accuracy.

3.3 Dependence of Eigenfrequencies on Nuclear Dissociation and Adiabatic Index

We now turn to the effect of nuclear dissociation on the oscillation frequencies and growth rates. As is observed in the right panels of Fig. 3.1, there is a substantial reduction in growth rate when the dissociation energy is raised to $\varepsilon = 0.25v_{\text{ff}}^2$ (and the Mach number upstream of the shock is reduced to $\mathcal{M}_1 = 5$). One also observes a significant drop in the real frequency. This effect is further illustrated in Figs. 3.3a,b for the fundamental $\ell = 1$ and $\ell = 2$ modes, as the rate of nuclear dissociation is gradually increased.

Both trends can be partially explained in terms of an increase in the advection time below the shock. A finite nuclear dissociation energy at the shock increases the compres-

sion factor κ (eq. 2.10) and decreases the post-shock Mach number

$$\mathcal{M}_2 = \left[\kappa \left(\gamma + \frac{1}{\mathcal{M}_1^2} \right) - \gamma \right]^{-1/2}. \quad (3.1)$$

The advection time scales as $r_{s0}/v_2 \propto \kappa$, whereas the lateral sound-travel time has a weak dependence on κ . As a result, the advection time increases relative to the lateral sound travel time. The growth rate of a mode of fixed ℓ peaks when the advection time is comparable to the period of a lateral sound wave within the settling zone between the shock and the surface of the accretor (see §3.4). This makes it more difficult for the pressure perturbation at diametrically opposite points on the shock to maintain the correct relative phase. The peak growth rate therefore moves to higher r_*/r_{s0} for fixed ℓ , or to a lower Legendre index for fixed r_*/r_{s0} , as ε is increased. This can be observed in Figs. 3.1 and 3.3a,c.

The advective-acoustic cycle yields a WKB growth rate scaling as $\omega_{\text{grow}} \sim \ln|Q|/t_Q$, where Q is the efficiency of the cycle and $t_Q \sim 2\pi/\omega_{\text{osc}}$ its duration (Foglizzo et al., 2007). For larger dissociation energies, t_Q is dominated by the advection time, and t_Q increases somewhat faster than linearly³ in κ . The oscillation frequencies depend mainly on the flow time, as can be seen by scaling them to $|v_2|/(r_{s0} - r_*)$ (Fig. 3.3d). On the other hand, Fig. 3.3c shows that the growth rates decrease with increasing ε even after this first-order effect is removed.

The growth rate also depends on the coefficients for the conversion of an outgoing sound wave to an ingoing entropy or vortex wave at the shock; and for the linear excitation of an outgoing sound wave by the ingoing mode. As is shown in Appendix D of Fernández & Thompson (2009b), the first coefficient *increases* with increasing dissociation energy. In the limit of strong shock compression, it is given by

$$\frac{\delta\rho_2^S}{\delta\rho_2^-} = -\frac{2(\gamma-1)(1-\mathcal{M}_2)}{\mathcal{M}_2(1+\gamma\mathcal{M}_2)} \sim \gamma^{1/2}(\gamma-1)\kappa^{1/2}. \quad (3.2)$$

³For large values of ε , the density profile steepens relative to $\rho \sim r^{-3}$ and thus the velocity decreases faster than linearly with radius. The advection time (3.3) is then dominated by the innermost part of the flow (see, e.g., Figure 2.2).

We therefore conclude that the reduction in growth rate signals a decreasing efficiency for the conversion of an ingoing entropy-vortex perturbation into a sound wave.

We also observe that the velocity gradient at the base of the settling flow becomes stronger with increasing shock compression: the gradient scale $v_r/(dv_r/dr)$ is reduced by a factor of ~ 2 as ε is raised from 0 to $0.25v_{\text{ff0}}^2$. We suspect that this second effect has a weaker influence on the growth rate, given our observation that that rapid growth depends on an approximate equality between the radial flow time and the lateral sound travel time in between the cooling layer and the shock (see §3.4).

The fundamental mode can be stabilized for sufficiently high ε , as is apparent in Fig. 3.3. Nonetheless an unstable mode can always be found among the higher radial overtones. Figure 3.4 shows the growth rates of the first 11 overtones of the $\ell = 1$ mode as a function of ε , for $r_*/r_{\text{s0}} = 0.4$.

Our ability to find linearly unstable modes stands in contrast to the analysis of Yamasaki & Yamada (2007), which employed a single, more realistic equation of state, and found no unstable modes in the absence of neutrino heating. But the comparison between both studies is made difficult by the fact that we are keeping the ratio r_*/r_{s0} fixed, whereas in the absence of heating Yamasaki & Yamada (2007) obtain a very small shock radius. It should also be emphasized that our unstable modes undergo a weak non-linear development: the position of the shock is perturbed only slightly when $\varepsilon \geq 0.15 v_{\text{ff0}}^2$ (see §4.3). Neutrino heating therefore plays a crucial role in maintaining large-amplitude oscillations of the shock for realistic values of the dissociation energy ε (§4.4).

A reduction in the upstream Mach number has a measurable effect on the frequency and growth rate of the SASI (see Fig. 3.5). When $\mathcal{M}_1 > 10$, one reaches the asymptotic, strong-shock regime, and the eigenfrequencies are essentially constant. Lower values of \mathcal{M}_1 push up the post-shock velocity and the real frequency of the mode (at fixed value of r_*/r_{s0}). Growth is substantially reduced for a weak shock when ε is close to zero, but is only modestly affected when ε is large.

The dependence of the growth rate ($\ell = 1$) on the adiabatic index γ is shown in Fig. 3.6 for $\varepsilon = 0$ and $0.25v_{\text{ff0}}^2$, in units of t_{ff0}^{-1} as well as $|v_2|/(r_{\text{s0}} - r_*)$. Reducing γ has some similar effects to increasing ε at fixed γ : the flow slows down below the shock, and the density profile steepens⁴. The growth rate is therefore reduced, and the peak growth rate is found at higher radial overtones (see §3.4). When the radius of the shock is allowed to vary, the peak growth rate moves to a higher value of r_*/r_{s0} as γ is decreased.

3.4 On the linear instability mechanism

Here we provide further insight into the mechanism driving the fastest growing, low-frequency modes of a spherical shock. We show that growth involves the radial advection of entropy and vortex perturbations, and the lateral propagation of sound waves in the settling flow below the shock. This explains the observation by Blondin & Mezzacappa (2006) that the communication of pressure perturbations by lateral sound waves plays a role in the SASI, but disagrees with their inference that the mechanism may be purely acoustic.

To this end, we calculate the growth rate as a function of the size of the settling region by solving the eigenvalue problem as formulated by Foglizzo et al. (2007) for several spherical harmonics in a zero-energy accretion flow ($\varepsilon = 0$). The basic configuration of the flow is the same as described in §2. By changing the ratio of r_* to r_{s0} , we are able to change the radial advection time relative to the time for a sound wave to propagate laterally within the flow.

The upper panel of Fig. 3.7 shows the growth rates of the fundamental (thick lines) and first radial overtone (thin lines) of the $\ell = 1 - 4$ modes, as a function of r_*/r_{s0} . The lower panel compares the advection time of the flow from the (unperturbed) shock in to

⁴In near hydrostatic equilibrium and for an adiabatic flow, $p/\rho \propto \rho^{\gamma-1} \propto r^{-1}$, thus $\rho \propto r^{-1/(\gamma-1)}$ and the profile steepens when γ decreases.

r_* ,

$$t_{\text{adv}} = \int_{r_*}^{r_{s0}} \frac{dr}{|v_r|}, \quad (3.3)$$

with the period of a meridional sound wave of Legendre index ℓ . The acoustic period is plotted at two different radii: right below the shock,

$$t_{\text{max},\ell} = \frac{2\pi r_{s0}}{\ell c_{s,2}}, \quad (3.4)$$

and at the base of the settling flow,

$$t_{\text{min},\ell} = \frac{2\pi r_*}{\ell c_{s,*}} \approx t_{\text{max},\ell} \left(\frac{r_*}{r_{s0}} \right)^{3/2}. \quad (3.5)$$

Here $c_{s,2}$ is the sound speed downstream of the shock, and $c_{s,*} = c_{s,2}(r_{s0}/r_*)^{1/2}$ is a good approximation to the sound speed at the top of the cooling layer. The self-gravity of the accreting material is assumed negligible, and most of the post-shock region is essentially adiabatic for the chosen cooling function. Hence, $t_{\text{max},\ell}$ corresponds to the longest possible period of a lateral sound wave of spherical harmonic ℓ outside the cooling layer. The shortest acoustic period ($\sim t_{\text{min},\ell}$) is found at the base of the settling flow.

For any given ℓ , the peak of the growth rate of the fundamental mode is always found where $t_{\text{min},\ell} < t_{\text{adv}} < t_{\text{max},\ell}$; the growth rate of the first radial overtone peaks where $t_{\text{min},\ell} < t_{\text{adv}}/2 < t_{\text{max},\ell}$. The basic result does not depend on whether one uses the radial advection timescale, or the sum of the advection time and the radial sound travel time (which is significantly shorter). Fig. 3.8 focuses on the radial overtones of $\ell = 1$, which have significant growth at large values of r_{s0}/r_* . The peak of the n -th radial overtone satisfies $t_{\text{min},1} < t_{\text{adv}}/(n+1) < t_{\text{max},1}$.

The main conclusion that we draw from Figs. 3.7 and 3.8 is that the radial flow time controls the overtone of the fastest-growing mode, while the period of the meridional sound wave controls the angular order. The situation is illustrated in Figure 3.9 for an $n = 0$ and $\ell = 2$ mode. This interplay between the two timescales points to the advective-acoustic cycle as the mechanism driving the instability.

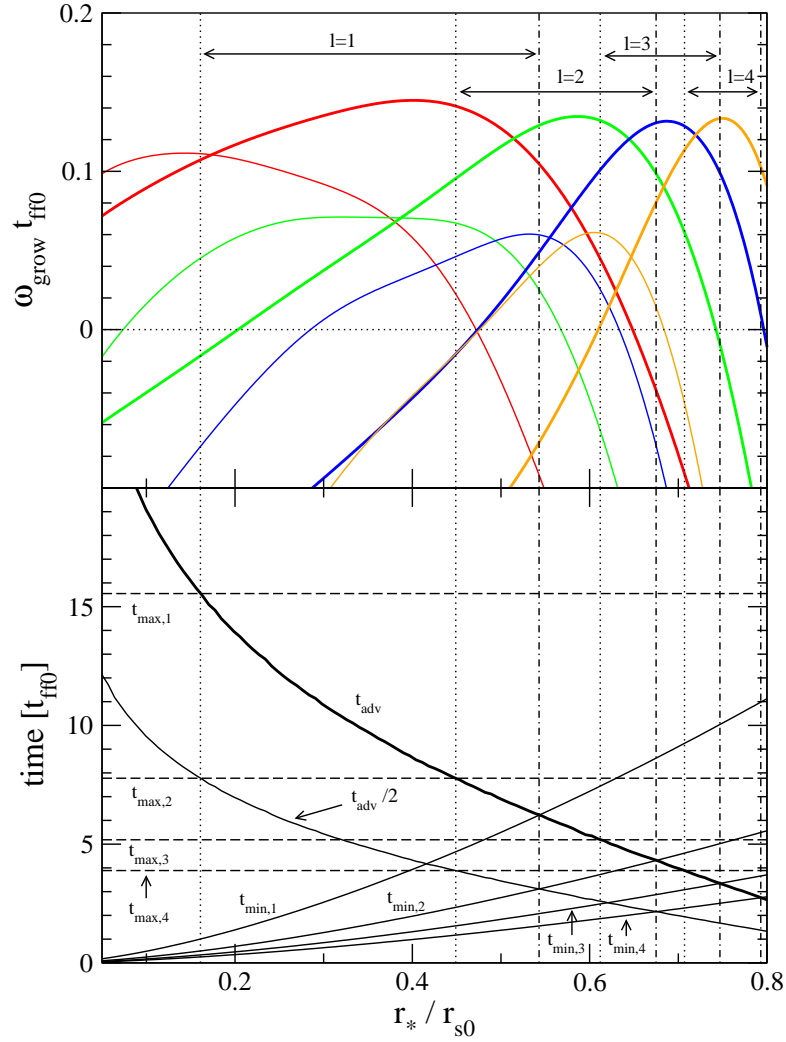


Figure 3.7: Upper panel: grow rates of linear modes of the shock, versus r_*/r_{s0} for various spherical harmonics: $\ell = 1$ (red), $\ell = 2$ (green), $\ell = 3$ (blue) and $\ell = 4$ (orange). Thick curves denote the fundamental mode; thin curves the first radial overtone. Lower panel: various timescales in the flow below the shock: advection time t_{adv} from shock to star; period $t_{\text{max},\ell}$ of lateral sound wave just below the shock; and period $t_{\text{min},\ell}$ of lateral sound wave just above the cooling layer. Dotted lines show the intersection between t_{adv} and $t_{\text{max},\ell}$, and dot-dashed lines the intersection between t_{adv} and $t_{\text{min},\ell}$. Growth of the fundamental mode is concentrated where $t_{\text{min},\ell} < t_{\text{adv}} < t_{\text{max},\ell}$, and similarly $t_{\text{min},\ell} < t_{\text{adv}}/(n+1) < t_{\text{max},\ell}$ for the n^{th} radial overtone.

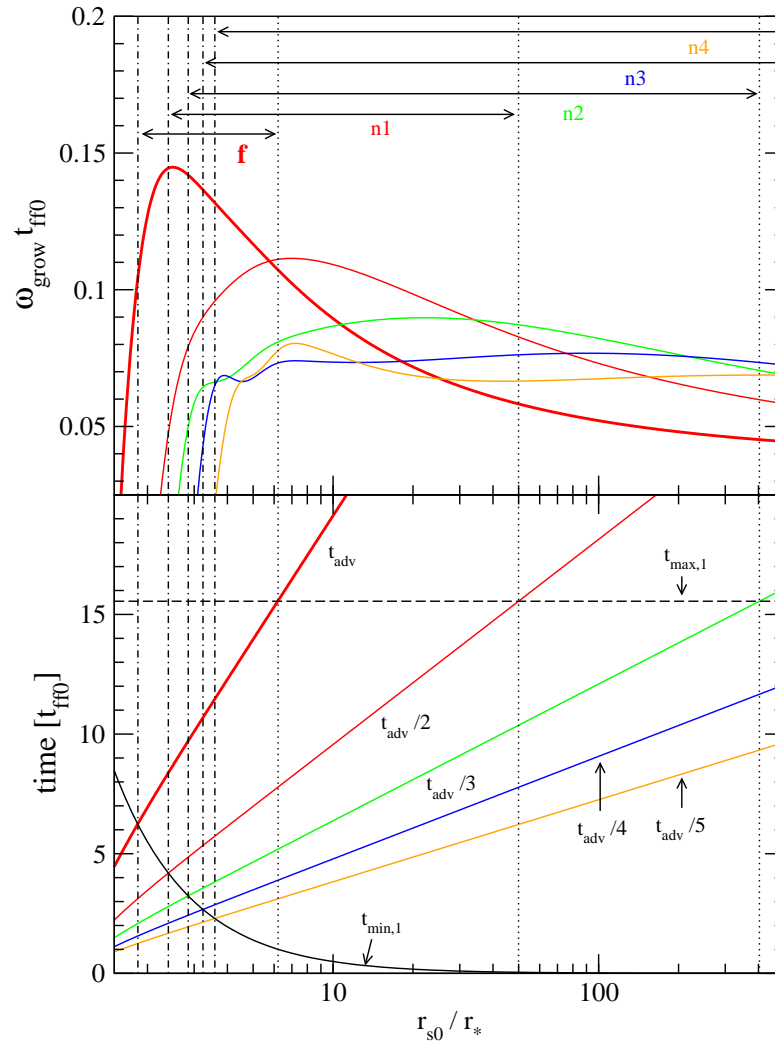


Figure 3.8: Same as Fig. 3.7, but now focusing on the radial overtones of $\ell = 1$ at large r_{s0}/r_* . We denote by **f**, **n1**, **n2**, **n3**, and **n4** the fundamental and first four overtones, respectively. Other quantities have the same meaning as in Fig. 3.7.

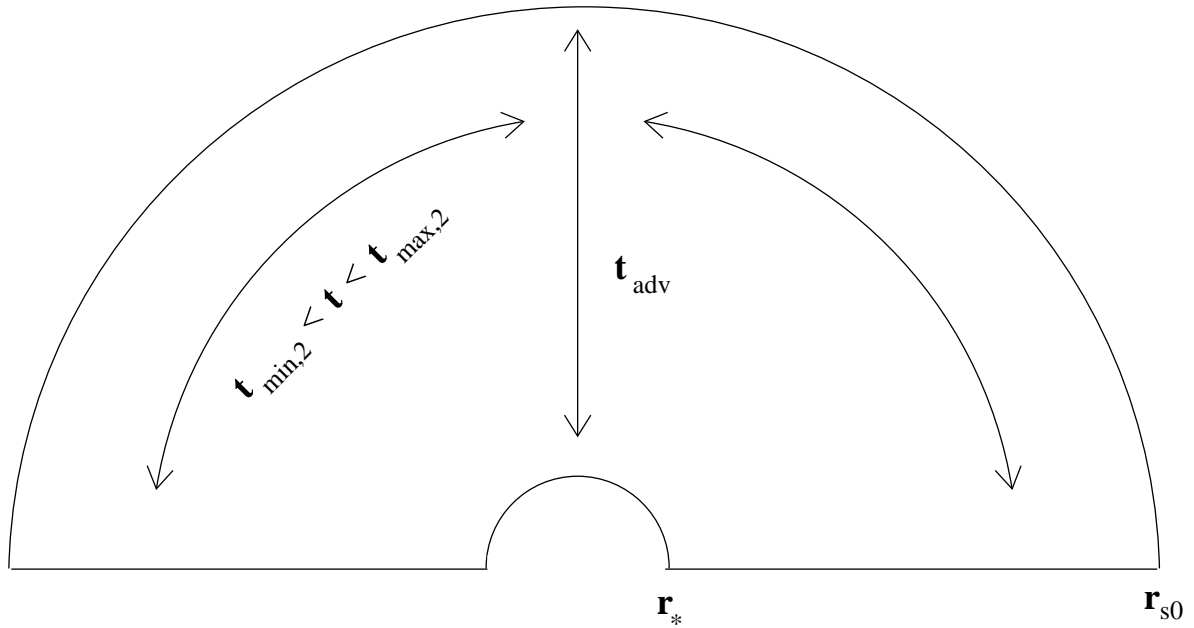


Figure 3.9: The linear growth rate of a given SASI mode is maximal for a mode with Legendre index ℓ and overtone n when the radial advection time across a distance $(r_{s0} - r_*)/(n + 1)$ is equal to the period of a lateral sound wave of wavelength $2\pi r/\ell$ at a radius r in between the shock and stellar radius. The Figure illustrates the case of the fundamental ($n = 0$) $\ell = 2$ mode.

The $\ell = 0$ mode deserves special comment. We find that its oscillation period is nearly twice the duration of the advective acoustic cycle, $2(t_{\text{adv}} + t_{\text{s,up}})$, where $t_{\text{s,up}}$ is the time taken for a sound wave to travel radially from r_* to r_{s0} . This is demonstrated for a wide range of shock radii in Fig. 3.10. A purely spherical perturbation of the shock will excite a downgoing entropy wave. For example, a stationary shock displacement $\Delta\xi$ will generate, for a strong shock with $\gamma = 4/3$ and negligible cooling, an entropy perturbation (Foglizzo et al., 2007)

$$\delta S = -\frac{\Delta\xi}{2r_{\text{s0}}} \left(\frac{5 - 3\gamma}{\gamma - 1} \right). \quad (3.6)$$

The corresponding pressure perturbation below the shock has the opposite sign (Foglizzo et al., 2007),

$$\frac{\delta p}{p} = -\frac{[1 + (\gamma - 1)\mathcal{M}_2^2]}{(1 - \mathcal{M}_2^2)} \delta S. \quad (3.7)$$

When the entropy wave reaches the cooling layer, the sign of the change in the (negative) cooling rate per unit volume (eq. [2.5]) is the same as the sign of the entropy perturbation (at constant pressure),

$$\frac{\delta \mathcal{L}_C}{\mathcal{L}_C} = -\frac{(\gamma - 1)}{\gamma} (\beta - \alpha) \delta S. \quad (3.8)$$

As a result, a positive pressure perturbation at the shock⁵ generates an increase in the cooling rate at the base of the settling flow, and therefore a negative pressure perturbation that is communicated back to the shock on the radial acoustic time. This secondary pressure perturbation is in phase with the pressure perturbation at the shock if the mode period is twice the period of the advective-acoustic cycle. This analysis of the $\ell = 0$ mode helps to explain the importance of lateral acoustic waves in the growth of non-radial perturbations.

⁵As measured at its unperturbed position.

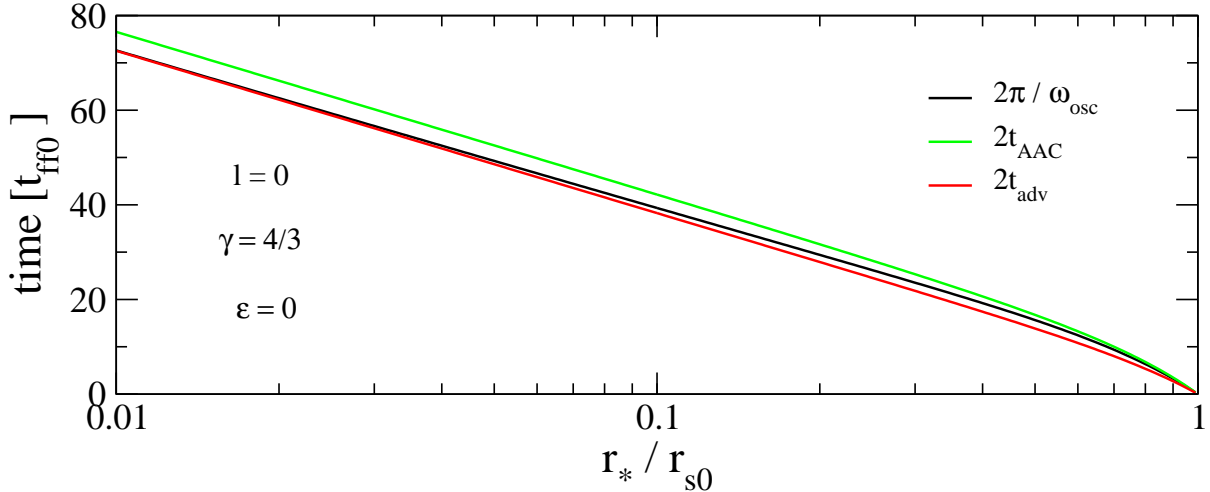


Figure 3.10: Period of the $\ell = 0$ fundamental mode (black curve), which is very close to twice the advection time (red) and twice the duration of the advective-acoustic cycle (green). Parameters of the flow: $\gamma = 4/3$ and $\varepsilon = 0$.

3.5 Summary

In this chapter we have investigated the linear phase of the Standing Accretion Shock Instability through a combination of time-dependent hydrodynamic simulations and linear stability analysis. The main results reported here are the following:

1. — The growth rate of the Standing Accretion Shock Instability (SASI) is significantly reduced when $\sim 20 - 50\%$ of the gravitational binding energy of the flow is absorbed by nuclear dissociation. A lowering of the adiabatic index of the flow (or, equivalently, a steepening of the density profile above $\rho(r) \sim r^{-3}$) has a similar effect. Introducing dissociation to the flow causes a strong reduction in growth rates even for relatively large adiabatic indices ($\gamma = 1.4 - 1.45$). The lower growth rates appear to result from a weaker coupling between the ingoing entropy-vortex wave and a sound wave that acts back on the shock. This reduced coupling is caused in part by a lengthening of the radial flow

time in comparison with the time for a sound wave to propagate laterally below the shock. Increasing the dissociation energy also pushes the strongest instability to lower ℓ at fixed r_*/r_{s0} , and to higher n at fixed ℓ .

2. — By solving the eigenvalue problem, we do find some unstable modes for all values of ε . By contrast, the linear stability analysis of Yamasaki & Yamada (2007) found no unstable modes for radial overtones ≤ 2 at vanishing neutrino luminosity (but evidence for very strong growth of $n = 3$ modes, which we do not find), albeit with small shock radii since their cooling function was fixed.

3. — The strongest growth of shock perturbations of spherical harmonic ℓ and radial overtone n is encountered when the radial flow time across a distance $\sim (r - r_*)/(n + 1)$ equals the period $2\pi r/\ell c_s(r)$ of a lateral sound wave, at some radius r in between the cooling layer and the shock. This provides a compelling argument as to why the linear instability involves a feedback between a radially propagating entropy-vortex perturbation, and a laterally propagating acoustic perturbation.

4. — The period of a spherical ($\ell = 0$) mode is nearly twice the radial flow time, that is, approximately double the period of the fundamental non-radial modes. This is due to a change in sign between the pressure perturbation at the shock, and the pressure perturbation that is induced in the cooling layer at the base of the accretion flow by the advected entropy perturbation.

Chapter 4

Non-Linear Phase of the SASI

4.1 Overview

This chapter addresses the non-linear development of the Standing Accretion Shock Instability in axisymmetry. Previous nonlinear studies have employed simplified adiabatic flows (Blondin et al., 2003; Blondin & Mezzacappa, 2006), included neutrino heating and a complete equation of state in a semi-realistic way (Ohnishi et al., 2006; Scheck et al., 2008; Iwakami et al., 2008), or made use of results from full collapse calculations (Buras et al., 2006b,a; Burrows et al., 2007b; Marek & Janka, 2009). With the exception of Ohnishi et al. (2006) and Scheck et al. (2008), most studies have addressed the problem in a descriptive, phenomenological way, focusing on the period of the oscillations, the relative strength of different modes, and the amount of instantaneous meridional kinetic energy generated. Ohnishi et al. (2006) examined the spherical harmonic spectrum of the shock during the saturated phase, showing that it follows a power-law and that there is mode coupling. Scheck et al. (2008) showed that the period of the instability closely follows the advection time, and explored its interplay with convection. These studies have, however, made use of a complete equation of state, and in one case employed a moving inner boundary (Scheck et al., 2008).

Work on the three-dimensional version of the instability has also been performed (Blondin & Mezzacappa 2007, Blondin & Shaw 2007 Iwakami et al. 2008, Yamasaki & Foglizzo 2008). At the time of this writing, this work is still in the descriptive stage, and focuses on the potential development of a spiral mode. Since there are fundamental differences in two- and three-dimensional hydrodynamics, we refrain from comparing our results to these studies (see Iwakami et al. 2008 for a comparison of the saturation amplitudes in 2D and 3D). This will be a subject for future study.

As with the linear phase, no systematic study has been performed to understand the effects of nuclear dissociation on the saturation amplitude, and thus the energy budget of the instability. We are also interested in understanding the extent to which the nonlinear shock oscillations observed during more realistic simulations, where convection is vigorous, are the consequence of an intrinsic instability of the fluid (i.e., the SASI) or arise as a consequence of forcing by convection.

In what follows, we present results from our time-dependent numerical experiments. We begin with a description of the transition from a laminar accretion flow to a turbulent, quasi-steady state (§4.2). We then explore some time-averaged properties of this state, such as angle-averaged profiles, saturation amplitudes, and energies (§4.3) when either dissociation at the shock or the size of the envelope are changed. Finally, we address the behavior of the SASI as heating is gradually introduced into the flow (§4.4).

4.2 From Linear Instability to Saturation

The oscillation of the shock, and the fluid below it, remains coherent during the initial linear phase. Consider the $\ell = 1$ SASI mode. The shocked fluid in the expanding pole has an increased energy density relative to the surrounding fluid. As a result, the expanding pole is the source of a sound wave that propagates laterally to the other pole. When the radial advection time is comparable to this lateral sound travel time, this pressure

enhancement reaches the opposite pole just as the phase of the oscillation has reversed, thereby reinforcing the outward expansion of the shock. The standing wave observed by Blondin & Mezzacappa (2006) can be interpreted in this way (instead of the purely acoustic phenomenon proposed by these authors).

The non-linear development of the SASI, in the absence of nuclear dissociation or in the presence of neutrino heating, involves relatively large shock deformations that generate non-radial flows and shock kinks (e.g, Blondin & Mezzacappa 2006; Scheck et al. 2008). On the other hand, when nuclear dissociation takes a significant fraction of the accretion kinetic energy and the SASI is not forced by convection, shock oscillations saturate at a much lower amplitude and shock kinks do not form. Nevertheless, nonlinear coupling between different modes still takes place and the shock thus acts as a generator of vorticity.

In the longer term, the axisymmetric flow reaches a quasi-steady state, with a broad range of oscillation frequencies. One could draw a parallel between this behavior and that of confined 2D turbulence, which reaches a quasi-steady state in which the vorticity accumulates on the largest spatial scales, decaying on the very long viscous timescale (Davidson, 2004).

4.3 Time-Averaged Properties

Since none of our simulated flows explode, we are able to average the properties of the fluid over a fairly long period of time ($T \sim 10^2 - 10^3$ dynamical times at the unperturbed position of the shock). In a turbulent system that displays a quasi-steady state behavior, a time average is equivalent to an ensemble average (e.g. Davidson 2004). The mean and r.m.s. fluctuation of a quantity $f(r, \theta, t)$ are defined in the usual way,

$$\langle f(r, \theta) \rangle \equiv \frac{1}{T} \int_0^T f(r, \theta, t) dt, \quad (4.1)$$

and

$$\Delta f(r, \theta) \equiv (\langle f^2 \rangle - \langle f \rangle^2)^{1/2}. \quad (4.2)$$

Fig. 4.1 shows the velocity field and sound speed, averaged over time and angle θ , in accretion flows with $\varepsilon = 0$ and $0.15v_{\text{ff}}^2$. At any given moment one can define minimum and maximum shock radii, which allows the construction of time averages $\langle r_{s,\text{min}} \rangle$, $\langle r_{s,\text{max}} \rangle$ and fluctuations $\Delta r_{s,\text{min}}$, $\Delta r_{s,\text{max}}$. One can distinguish four different zones in the flow, from the inside out: (1) the cooling layer, extending from the inner boundary to roughly the point of maximum of $\langle c_s \rangle$; (2) the adiabatic envelope, which is bounded above approximately by $\langle r_{s,\text{min}} \rangle - \Delta r_{s,\text{min}}$; (3) the shock oscillation zone, extending from this radius out to $\langle r_{s,\text{max}} \rangle + \Delta r_{s,\text{max}}$; and (4) the supersonic accretion flow. It is immediately evident that, as expected from the quasi-steady state behavior, accretion proceeds almost the same as in the unperturbed case, with $\langle v_r \rangle$ and $\langle v_\theta \rangle$ closely following the unperturbed velocity profile. The fluctuations Δv_r and Δv_θ are comparable in magnitude and much larger than the mean flow, although they remain below $\langle c_s \rangle$. As expected, the angle average of $\langle v_\theta \rangle$ vanishes. Notice also that the sound speed in the mean flow is everywhere lower than in the initial configuration, a point that we explore below.

A dramatic feature of Fig. 4.1 is the reduction in the amplitude of the shock oscillation as the effect of nuclear dissociation is introduced into the flow. It is important to understand the extent to which the oscillations seen in core collapse simulations are the result of an intrinsic fluid instability, as opposed to a coupling of the shock to the convective motions that are maintained by neutrino heating. To this end, we have run a series of simulations with ε increasing from 0 to $0.25v_{\text{ff}}^2$, and analyzed the change in the character of the turbulence. Since the growth rate of the SASI is strongly reduced by nuclear dissociation, we have chosen a ratio of accretion radius to shock radius for which the growth rate of the fundamental peaks when $\varepsilon = 0$ (namely $r_*/r_{s0} = 0.4$, the same value used for our explosion calculations, see §2.3.1). A fraction $1 - 2\varepsilon/v_{\text{ff}0}^2$ of the accre-

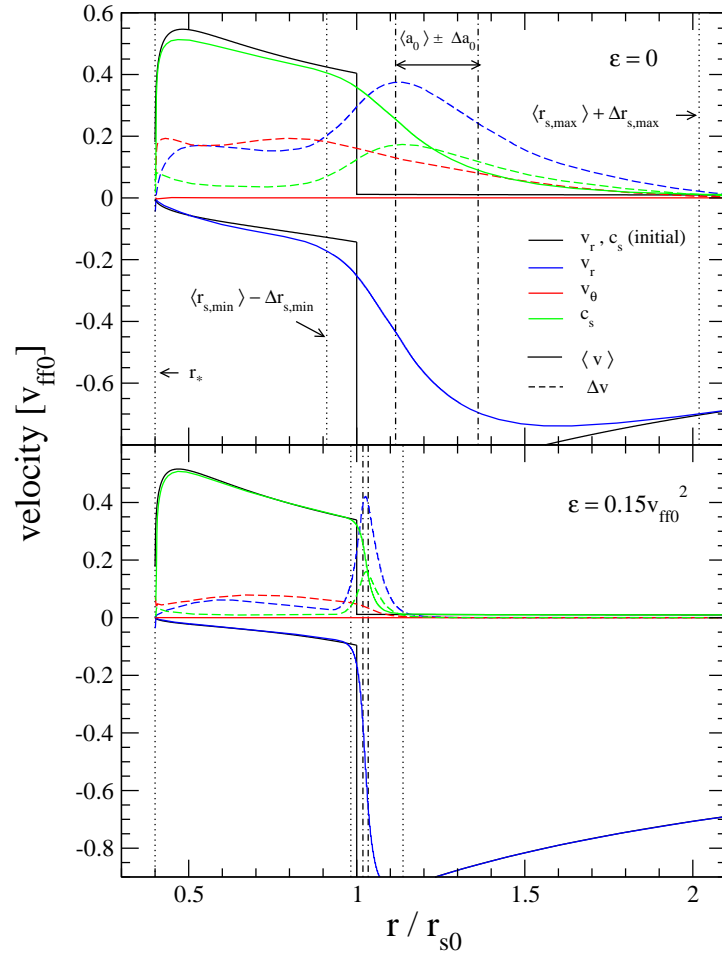


Figure 4.1: Time-averaged profiles of velocity and sound speed in the fully developed, nonlinear phase of the SASI. Upper panel represents a zero-energy flow ($\varepsilon = 0$), and lower panel a flow in which internal energy $\varepsilon = 0.15v_{\text{ff0}}^2$ is removed below the shock. Notice that the shock moves over a smaller range of radii in the second case. Spherical and temporal averages are given by the solid lines, and r.m.s. fluctuations by the dashed lines, for: radial velocity (blue), radial velocity in the unperturbed flow (lower black); meridional velocity (red), sound speed (green) and sound speed in the unperturbed flow (upper black). Vertical lines denote: the inner boundary (left dotted); the inner excursion of the shock (middle dotted); the outer excursion of the shock (right dotted); the r.m.s. range of the $\ell = 0$ component of the shock radius (dot-dashed). See the text for definitions of these quantities. Other parameters are $r_*/r_{s0} = 0.4$, $\gamma = 4/3$, $\mathcal{M}_1 = 87$.

tion energy at the shock is available for exciting turbulent motions below the shock. This corresponds to 50% – 100% of the accretion energy for the flows that we are examining.

The results of this study are summarized in Figs. 4.2 and 4.3, and Table 4.1. The first figure shows the amplitude of the $\ell = 0, 1$ Legendre coefficients $a_{0,1}$ of the shock radius, as a function of time, for a few runs. Their amplitude drops dramatically as ε increases above $0.15 v_{\text{ff}}^2$. Some configurations display significant intermittency in the oscillations, as exemplified by the case $\varepsilon = 0.1 v_{\text{ff}}^2$.

The following figure shows the time-average $\langle a_{0,1} \rangle$ and r.m.s. $\Delta a_{0,1}$ of the Legendre coefficients ($\langle a_1 \rangle \approx 0$). These quantities have been normalized to the time-average of the steady shock position for a 1D run with the same parameters. This procedure allows us to remove a small offset from r_{s0} in $\langle a_0 \rangle$ that is caused by the finite initial velocity at the inner boundary of the simulations, as can be seen in the upper panels of Fig. 4.2. The $\ell = 0$ mode, being stable, settles to a steady value within a few oscillation cycles. For the lower values of ε , a modest monopole shift in the shock radius remains in 2D, as compared with 1D, but this becomes insignificant for $\varepsilon \geq 0.15 v_{\text{ff}}^2$. The time-averaged $\ell = 1$ coefficient nearly vanishes when half of the accretion energy is removed by dissociation ($\varepsilon = 0.25 v_{\text{ff}}^2$).

In a real core collapse, the protoneutron star contracts by more than a factor of two in radius while the shock is still stalled. We have therefore run a series of simulations with different r_*/r_{s0} , to check whether the envelope size has a significant influence on the properties of the saturated state. Figure 4.4 shows the $\ell = 0, 1$ Legendre coefficients for these runs, which have vanishing dissociation energy. As the envelope size increases by a factor of two, the fractional $\ell = 0$ expansion of the shock nearly doubles, increasing from $1.15 \langle r_s \rangle_{1\text{D}}$ to $1.29 \langle r_s \rangle_{1\text{D}}$, where $\langle r_s \rangle_{1\text{D}}$ is the steady shock position in 1D. On the other hand, the rms amplitude of the $\ell = 1$ oscillations only increases by $\sim 20\%$.

The partitioning of the energy of the fluid below the shock into different components is explored in the lower panels of Figs. 4.3 and 4.4. Since our 1D runs do not display any growing mode, and settle into a well-defined steady state configuration, we use them

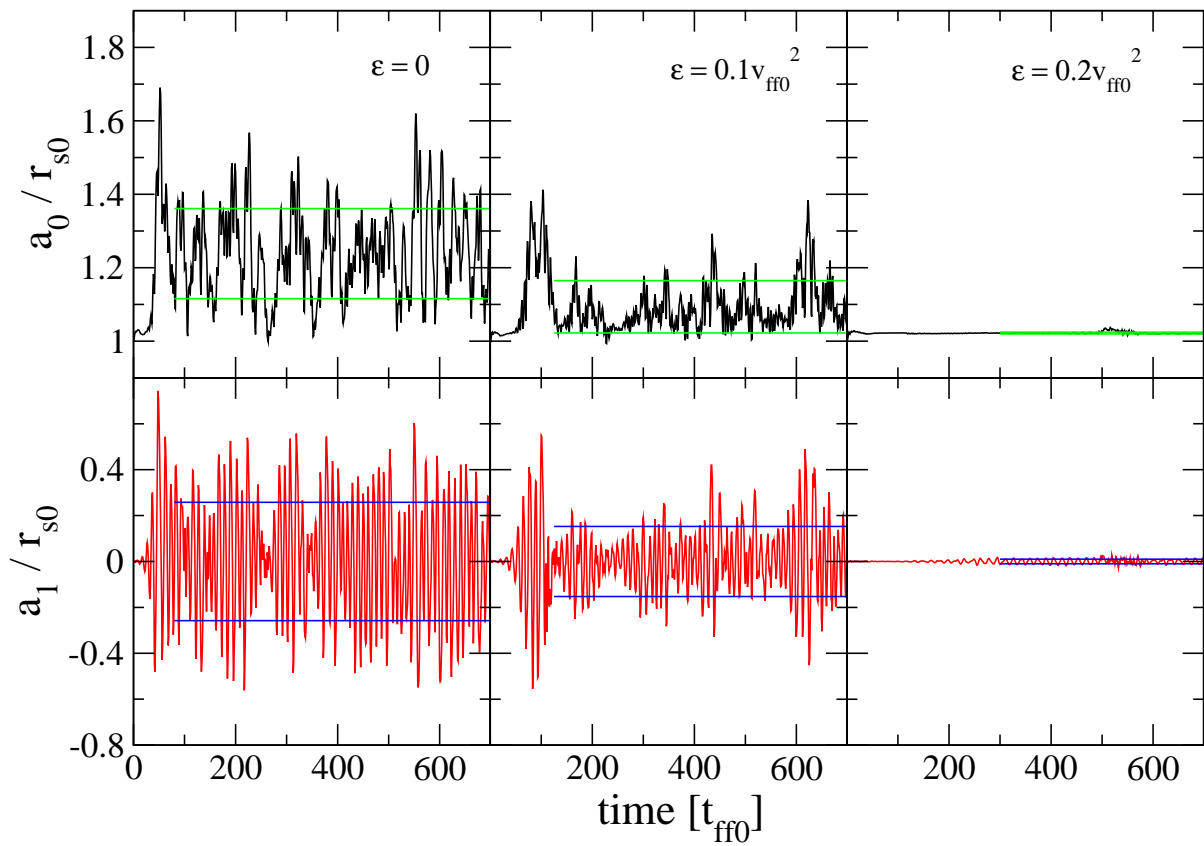


Figure 4.2: Amplitudes of $\ell = 0$ (upper) and $\ell = 1$ (lower) components of the shock radius, versus time. Panels from left to right represent flows with increasing dissociation energies: $\varepsilon = 0$, $0.1v_{\text{ff0}}^2$, and $0.2v_{\text{ff0}}^2$. The horizontal lines bound the r.m.s. fluctuation of each Legendre coefficient.

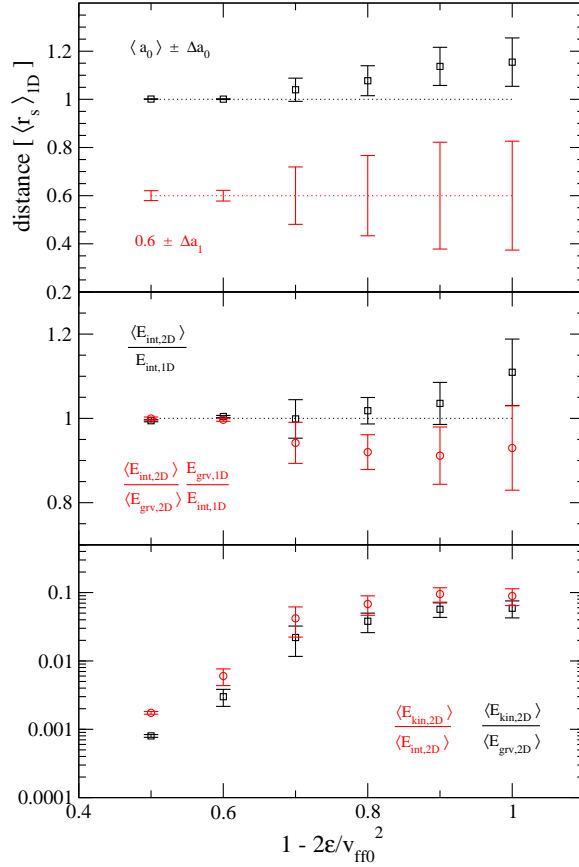


Figure 4.3: Time-averaged properties of the shocked flow. Horizontal axis labels the fraction of the gravitational energy that is available for exciting oscillations of the shock. Upper panel: r.m.s. fluctuation of the $\ell = 0$ and $\ell = 1$ components of the shock radius, with points denoting mean values. Radius has been scaled to the equilibrium shock radius in the 1D solution (which is stable). Middle panel: various components of the energy of the 2D flow below the shock, averaged over time, relative to the 1D flow. Black symbols denote internal energy and red symbols denote ratio of internal to gravitational energy. Error bars represent the r.m.s. fluctuation. Lower panel: time average of the fluid kinetic energy below the shock, relative to the internal energy (red symbols) and gravitational energy (black symbols). Notice the dramatic drop in these ratios with increasing dissociation energy. The system expands mainly as a result of the growth of turbulent kinetic energy, with a smaller net change in internal energy.

to calculate reference values of the kinetic, internal, and gravitational potential energies. These quantities are denoted by $E_{\text{kin},1\text{D}}$, $E_{\text{int},1\text{D}}$, and $E_{\text{grav},1\text{D}}$, respectively, with the spatial integral being carried out between the radius at which c_s peaks and $\langle r_s \rangle_{1\text{D}}$. The analogous quantities $\langle E_{\text{kin},2\text{D}} \rangle$, $\langle E_{\text{int},2\text{D}} \rangle$, and $\langle E_{\text{grav},2\text{D}} \rangle$ are obtained by integrating over volume and averaging over time¹. Table 4.1 displays the time averaged energies and their rms fluctuations for both sequences of runs. By increasing ε and thus the shock compression factor κ , the mass in the adiabatic layer increases and so does the gravitational binding energy. The internal energy also increases with increasing dissociation energy, because approximate hydrostatic equilibrium needs to be maintained.

Table 4.1: Time-Averaged Energy^a of Flow below Shock (2D)

r_*/r_{s0}	$\varepsilon/v_{\text{ff0}}^2$	$ \langle E_{\text{grv}} \rangle $	$\langle E_{\text{int}} \rangle$	$\langle E_{\text{kin},r} \rangle$	$\langle E_{\text{kin},\theta} \rangle$
0.4	0	62 ± 4	40 ± 3	1.8 ± 0.6	1.7 ± 0.5
	0.05	74 ± 3	45 ± 2	1.6 ± 0.7	1.7 ± 0.6
	0.1	95 ± 3	55 ± 2	1.4 ± 0.7	1.4 ± 0.7
	0.15	129.1 ± 0.9	74 ± 1	0.4 ± 0.2	0.4 ± 0.2
	0.2	200.0 ± 0.7	107.6 ± 0.6	0.2 ± 0.1	0.1 ± 0.1
	0.25	320.3 ± 0.7	159.6 ± 0.3	0.21 ± 0.02	0.13 ± 0.03
0.5	0	39 ± 3	26 ± 2	1.2 ± 0.5	1.1 ± 0.4
0.375	0	70 ± 6	46 ± 4	1.8 ± 0.7	1.6 ± 0.5
0.25	0	123 ± 7	80 ± 4	3.1 ± 1.0	2.5 ± 0.7

^a Energies are measured in units of $\rho_1 v_{\text{ff0}}^2 r_{\text{s0}}^3 \approx 3.4 \times 10^{48} \dot{M}_{0.3} M_{1.3}^{1/2} (r_{\text{s0}}/150\text{km})^{1/2}$ erg. Error bars denote the r.m.s. fluctuation.

The internal energy measured in the 2D simulations generally overlaps that in the 1D flow, with some increase for $\varepsilon = 0$ and $\varepsilon = 0.2v_{\text{ff0}}^2$. Its ratio to the gravitational

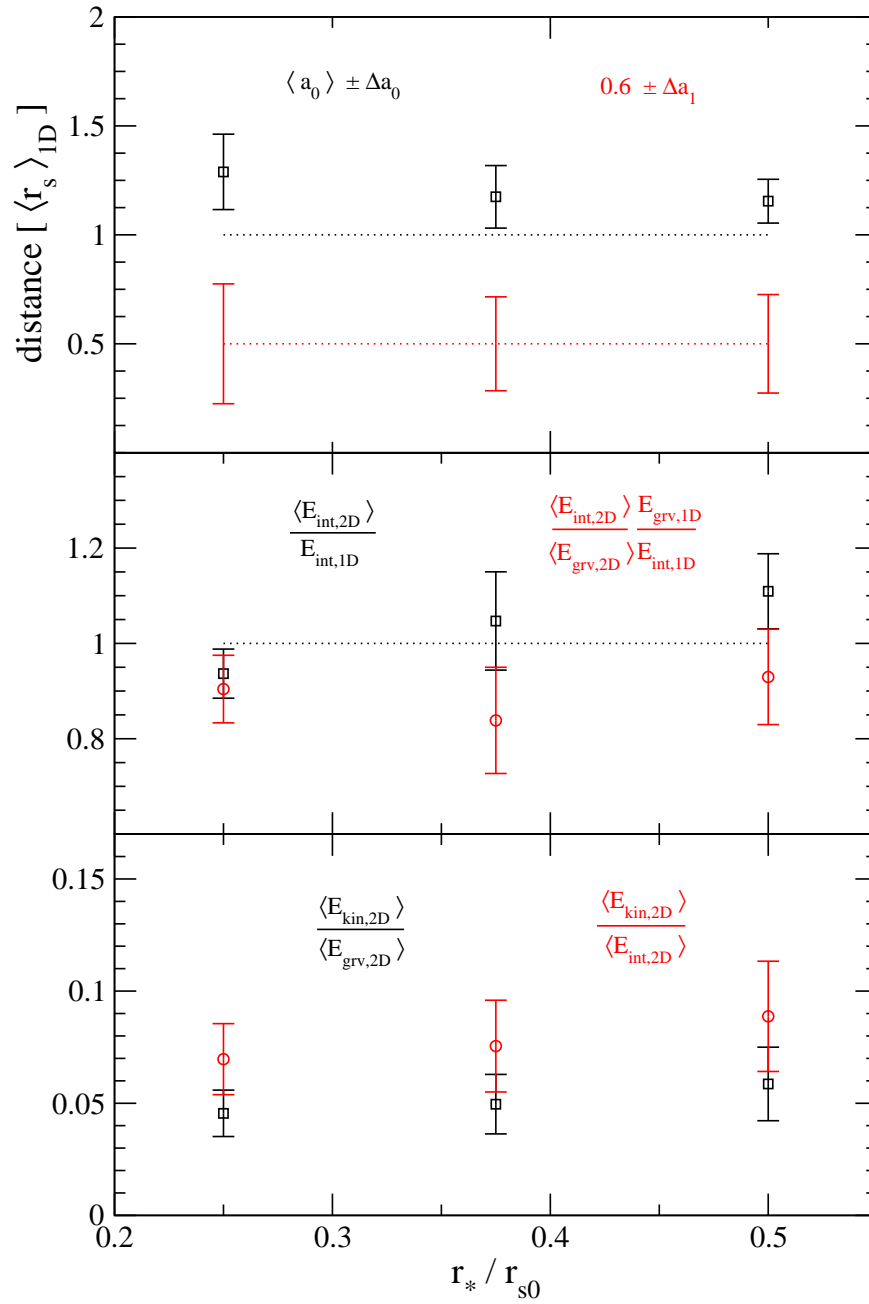
¹The integration over volume is performed from the radius at which the angle and time average of c_s peaks to the instantaneous shock surface.

energy, however, drops by about 10% relative to the 1D flow for $\varepsilon = 0 - 0.2v_{\text{ff}0}^2$, which is compensated by the increase in kinetic energy (see also Table 4.1). So our results point to a scenario in which the post-shock envelope expands as a result of the onset of turbulence, keeping its internal energy nearly constant. The fraction of the accretion energy that is converted to turbulent kinetic energy decreases with increasing ε , from $\sim 10\%$ of the internal energy for $\varepsilon = 0$ to about 0.1% for $\varepsilon = 0.2v_{\text{ff}0}^2$. From Table 4.1 one can see that the total turbulent kinetic energy is very close to the fluctuation in the internal energy. As regards the dependence on r_*/r_{s0} , we note that the fraction of the internal energy going to turbulence decreases with increasing envelope size, but the absolute value of the turbulent kinetic energy more than doubles.

4.4 Convection and the SASI

Overturms of the fluid below the shock can be triggered in two distinct ways: through the development of Schwarzschild convection in the presence of a strong negative entropy gradient, or via the non-linear development of the SASI (§4.3). We now show that the amplitude of the dipolar mode that is excited in the shock is strongly tied to the level of neutrino heating, and so depends on a balance between non-linear excitation and damping mechanisms. To a certain extent, this distinction is of secondary importance, in the sense that memory of the linear phase of the instability is lost once the inflow of fresh material below the shock bifurcates from older shocked fluid. Nonetheless, the origin of the convective motions does have implications for the stability of $\ell = 1$ and 2 modes in 3D simulations: one expects that large scale oscillations will change shape and direction more rapidly if they are triggered primarily by neutrino heating.

We can ask whether a heating parameter H that yields an explosion will also form an unstable entropy gradient below the shock. Convection develops through a competition between inward advection and neutrino heating. A detailed analysis by Fogliizzo et al.

Figure 4.4: Same as Fig. 4.3, but now varying r_*/r_{s0} for fixed $\varepsilon = 0$.

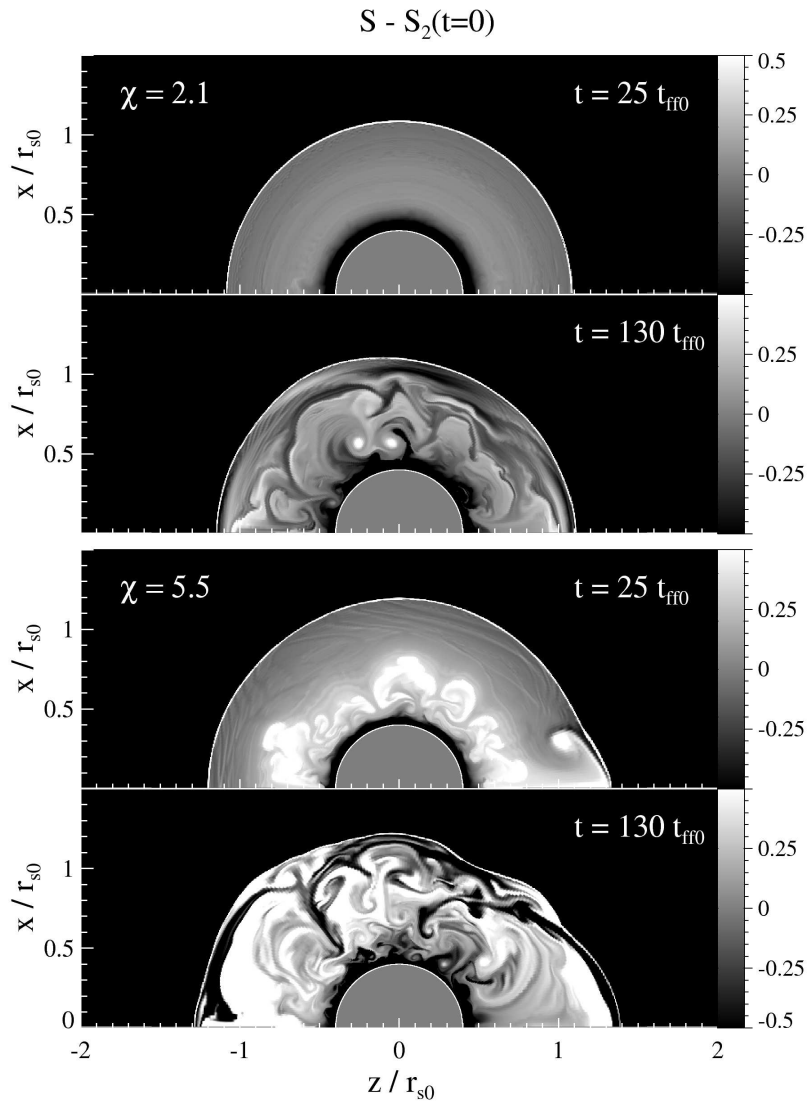


Figure 4.5: The development of a convective instability is strongly limited when the parameter $\chi \lesssim 3$. These panels show snapshots of entropy (normalized to initial postshock value) in a NSE run ($r_{s0} = 75$ km) with two different heating rates. When $\chi = 2.1$, convective cells of a limited extent are triggered in the layer where the net heating rate is strongest, but they do not propagate into the upper parts of the gain region. Convection becomes much more vigorous and widespread when $\chi = 5.5$. Note that both of these models are non-exploding.

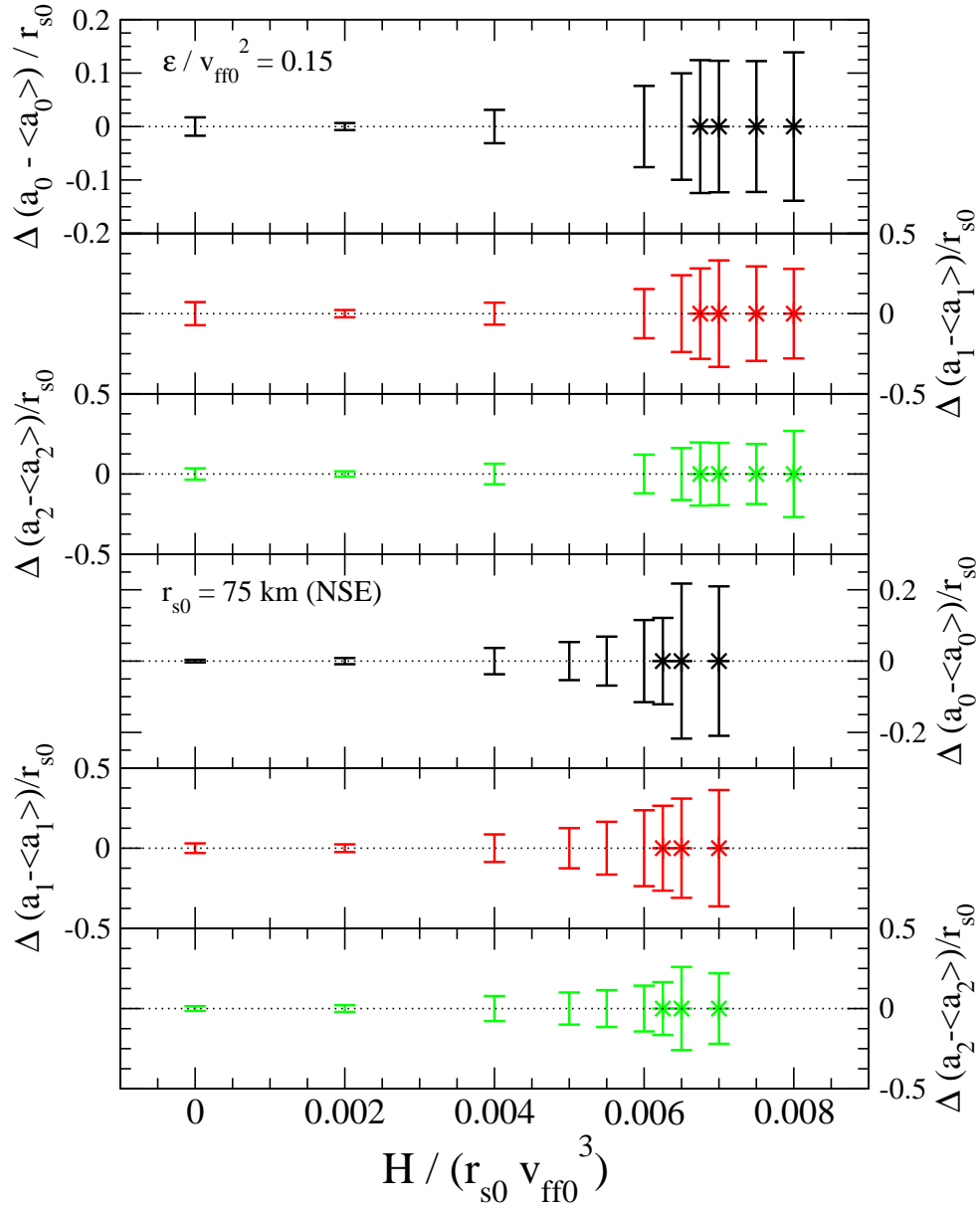


Figure 4.6: Amplitude (r.m.s.) of $\ell = 0, 1, 2$ modes of the shock in two model sequences with varying heating parameter H . Stars indicate exploding runs. We show the r.m.s. fluctuation of the difference between the instantaneous Legendre coefficient a_ℓ and a running average $\langle a_\ell \rangle_{50t}$ that is computed over a window of width $50t_{\text{ff0}}$ (see text). This subtracts the secular movement of the shock in runs that are close to or above the threshold for explosion. Note that the amplitude is measured in absolute units (r_{s0}).

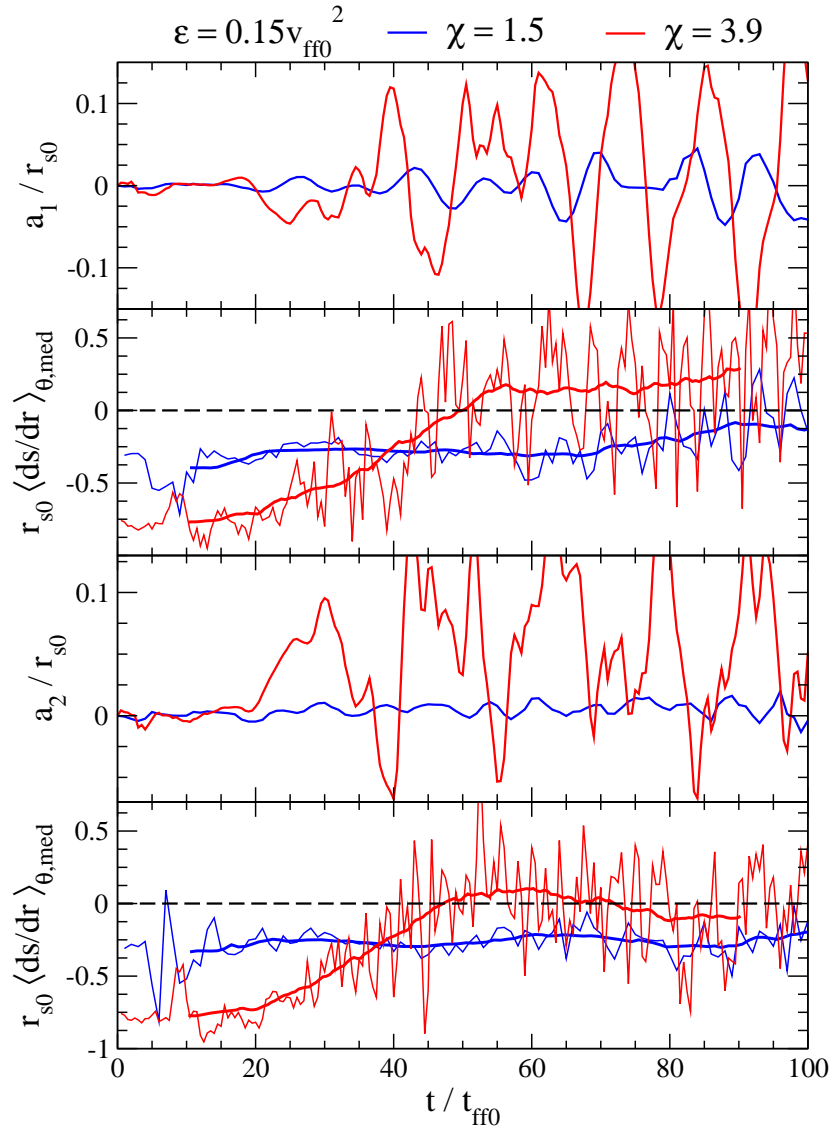


Figure 4.7: Principal shock Legendre coefficient and the radial median of the angle-averaged entropy gradient for the $\varepsilon = 0.15v_{\text{ff0}}^2$ model and two different heating rates, corresponding to $\chi = 1.5$ ($H = 0.002 r_{s0} v_{\text{ff0}}^3$, blue curves) and $\chi = 3.9$ ($H = 0.004 r_{s0} v_{\text{ff0}}^3$, red curves). Both runs are below the threshold for an explosion, but vigorous convection is established throughout the gain region in the run with the higher heating rate. Top (bottom) two panels: seed perturbation is a shell with $\ell = 1$ ($\ell = 2$) density profile. A running average of the entropy gradient (temporal width $20t_{\text{ff0}}$) appears as thick solid lines.

(2006) shows that the parameter

$$\chi \equiv \int \left| \frac{\omega_{\text{BV}}}{v_r} \right| dr, \quad (4.3)$$

must exceed a critical value $\simeq 3$ for unstable convective plumes to grow before being advected downward through the gain region below the shock. Here ω_{BV} is the Brunt-Väisälä frequency (e.g., Kippenhahn & Weigert 1994),

$$\omega_{\text{BV}}^2 = \frac{1}{\gamma} \left(\frac{GM}{r^2} \right) \left(\frac{\partial \ln p}{\partial r} - \gamma \frac{\partial \ln \rho}{\partial r} \right) = \frac{(\gamma - 1)}{\gamma} \left(\frac{GM}{r^2} \right) \frac{\partial S}{\partial r}. \quad (4.4)$$

Using our initial flow models, we can translate H into a value for χ , and find (Table 2.2) that typically $\chi \sim 5 - 20$ at the threshold for a neutrino-driven explosion. The implication for convection below the shock is illustrated in Fig. 4.5, which shows two snapshots for models with $\chi = 2.1$ and 5.5, neither of which explodes. At the lower heating rate, the time required for convection to develop depends on the strength of the seed perturbation, whereas at the higher heating rate convective overturns develop rapidly within the layer of strong neutrino heating and spread throughout the post-shock region over a few dozen dynamical times. (The figure shows the result in the case where the seed perturbation is dominated by a small spherical startup error in the initial model.) A larger growth rate of the SASI does not change this qualitative result, as its growth requires at least a few oscillations with period comparable to an advection timescale, thus being implicitly accounted for in the definition of χ . The quantitative difference would be that, below the critical value, the SASI would grow faster and to larger amplitudes. We conclude that, near the threshold for a neutrino-driven explosion and for our given set of physical assumptions, convection is driven primarily through the development of a strong, negative entropy gradient within the gain region, rather than through the non-linear development of SASI modes.

In §4.3 we considered the non-linear, saturated state of the SASI in the absence of neutrino heating, and showed that the amplitude of the shock oscillations drops significantly as the dissociation energy ε is increased. We now explore how the r.m.s. amplitude

of the shock oscillations correlates with the strength of heating. To eliminate the effect of secular shock motions around or above the threshold for explosion, we first calculate the running average $\langle a_\ell \rangle_{50t}$ of the shock Legendre coefficients a_ℓ over an interval $50t_{\text{ff0}}$, and then calculate the r.m.s. fluctuation of $\hat{a}_\ell \equiv a_\ell - \langle a_\ell \rangle_{50t}$ over the duration of each simulation. The result is plotted in Fig. 4.6 as a function of H for two model sequences ($\varepsilon = 0.15v_{\text{ff0}}^2$ and NSE with $r_{\text{s0}} = 75$ km).

There is a clear trend of increasing $\ell = 1, 2$ mode amplitude with increasing heating rate. This confirms our previous suggestion that large-amplitude shock oscillations require strong heating when the dissociation energy behind the shock exceeds $\sim 0.15v_{\text{ff0}}^2$. The models with $H = 0$ reveal a slight exception to the overall trend: the r.m.s. amplitude of the shock oscillations appears larger than it does in models with small but finite heating rate, because the oscillations are strongly intermittent at $H = 0$ (see middle panels of Figure 4.3). The shock oscillations grow much stronger just below the threshold for explosion (exploding runs are marked by stars), above which they seem to saturate. Note also that their amplitudes do not vary much with the choice of dissociation model. The r.m.s. amplitudes relative to the running average of a_0 at the threshold for explosion are $\{5\%, 12\%, 8\%\}$ for the $\ell = 1, 2, 3$ modes in the $\varepsilon/v_{\text{ff0}}^2 = 0.15$ sequence, and $\{6\%, 12\%, 7\%\}$ in the NSE $r_{\text{s0}} = 75$ km sequence.

We have performed an additional sequence of runs in which we drop an overdense shell with a given Legendre index ℓ through the shock (see §2.3.2). This has the effect of selectively triggering individual SASI modes. Figures 4.7 and 4.8 display the Legendre coefficients of the shock alongside the radial median (over the gain region) of the angle-averaged entropy gradient. We find that the amplitude of the $\ell = 1$ and 2 modes is strongly tied to the strength of convection. For both types of dissociation models, convection is quenched by the accretion flow when $\chi < 3$: it grows intermittently in strength, but never reaches large enough amplitudes to significantly distort the shock surface. As a consequence, the entropy gradient remains shallow and negative most

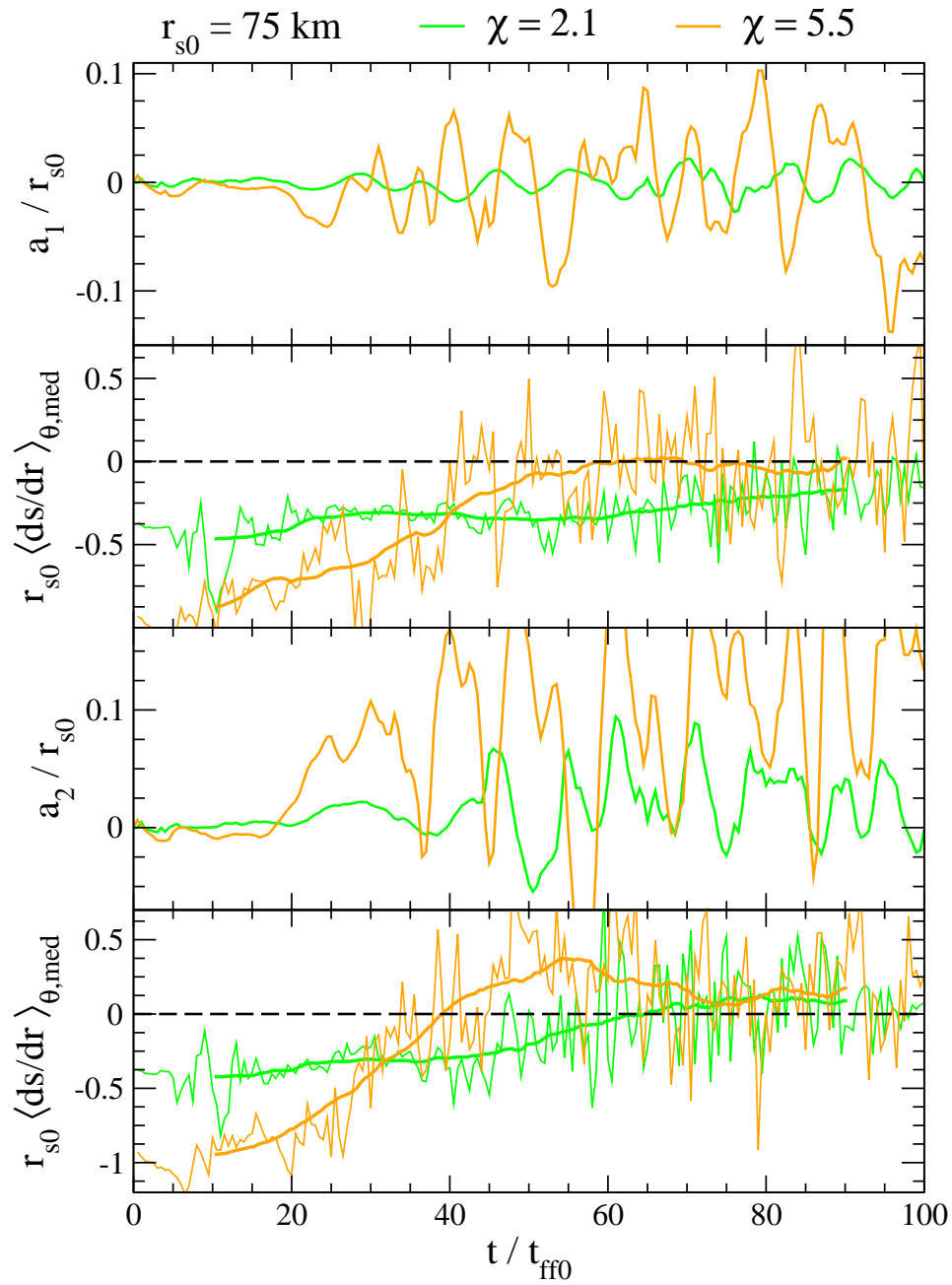


Figure 4.8: Same as Fig. 4.7, but for NSE models with α -particles and $r_{s0} = 75$ km.

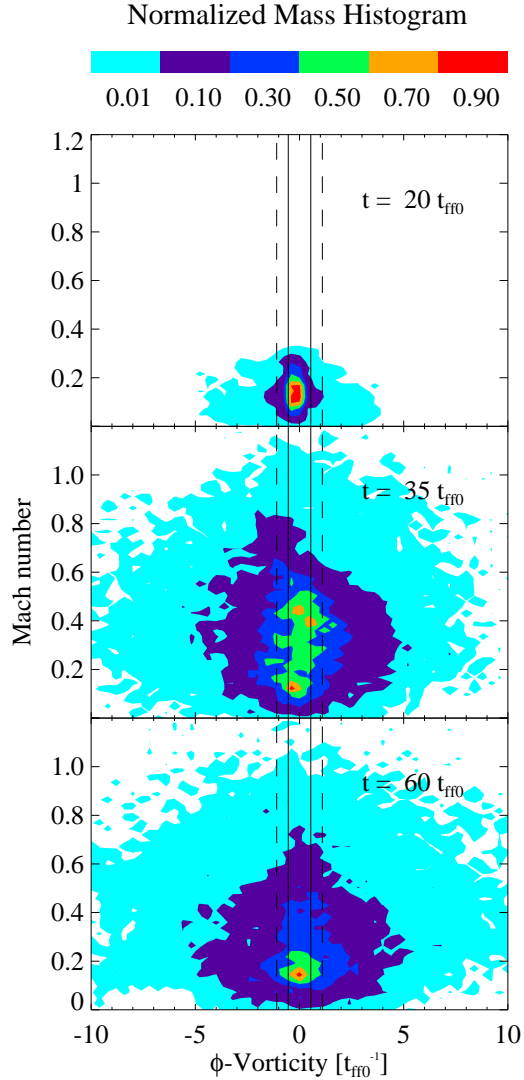


Figure 4.9: Histogram of vorticity vs. Mach number in the gain region, weighted by mass, at three different instants in the evolution of the run with $\varepsilon = 0.15v_{\text{ff0}}^2$, $\ell = 1$ seed perturbation, and $\chi = 3.9$ (corresponding to the upper two panels in Fig. 4.7). The distribution broadens once convection is fully developed, but before the dipolar shock mode shows significant growth. The vertical lines show the vorticity of a convective flow with period equal to (solid) the mean radial advection time and (dashed) the period of a lateral sound wave at the midpoint between r_* and r_s .

of the time, with coherent shock oscillations taking place simultaneously. The shock oscillations have a low amplitude due to the large dissociation energy.

Convection grows much more rapidly when $\chi > 3$, distorting the shock surface before the SASI has the chance to execute a few oscillations. In this case, the entropy gradient is initially more negative, but quickly flattens. Indeed, the $\ell = 1, 2$ amplitudes only become large in models where neutrino-driven convection is strong enough to flatten the entropy gradient.

Another way of seeing that convection is the forcing agent behind shock oscillations when $\chi > 3$ is to analyze the distribution of vorticity in the gain region. Figure 4.9 shows a histogram of vorticity vs. Mach number at three different instants in the evolution of the run with $\varepsilon = 0.15v_{\text{ff0}}^2$, $\ell = 1$ seed perturbation, and $\chi = 3.9$ (upper two panels in Figure 4.7). At $t = 20t_{\text{ff0}}$, convection is just getting started and the vortical motions are restricted to Mach numbers $\lesssim 0.3$. However, by $t = 35t_{\text{ff0}}$ the Mach number distribution extends up to $\mathcal{M} \gtrsim 0.5$ and has almost reached its asymptotic form ($t = 60t_{\text{ff0}}$), at the same time that convection has filled the region below the shock. The dipolar mode of the shock develops a large amplitude only after this fully developed convective state has been reached. The convective rolls are a source of acoustic radiation (e.g. Goldreich & Kumar 1988), which will drive a dipolar oscillation of the shock if the overturn frequency is comparable to the frequency of the $\ell = 1$ mode, $|\nabla \times \mathbf{v}| \sim 2 \times 2\pi/t_{\text{adv}}$. This zone is marked by the vertical solid lines in Fig. 4.9, and indeed encompasses most of the mass.

4.5 Summary

In this chapter we have studied the nonlinear properties of the SASI when a finite rate of nuclear dissociation is allowed to take place behind the accretion shock, and when neutrino heating is gradually added into the fluid, driving convective motions. The main results can be summarized as follows:

1. — The nonlinear development of the SASI in two dimensions and without heating is characterized by a quasi-steady state that is reached after the linear modes have saturated. As the dissociation energy is increased, the fluctuations of the shock about its unperturbed position are greatly reduced in amplitude. We infer that strong neutrino heating is needed to drive large-amplitude, dipolar oscillations of the shock in a realistic core collapse environment.

2. — The expansion of the shock that we observe appears to be driven mainly (but not entirely) by the action of turbulent pressure; we observe a smaller absolute positive change in the internal energy of the flow below the shock. The turbulent kinetic energy saturates at $\lesssim 10\%$ of the internal energy. A large expansion of the shock therefore is possible only if the flow has nearly vanishing total energy.

3. — The amplitude of the $\ell = 1$ and 2 modes correlates strongly with the value of the heating parameter, and is coupled to the appearance of vigorous neutrino-driven convection below the shock. In agreement with the work of Foglizzo et al. (2006) and Scheck et al. (2008), we find that $\chi \approx 3$ marks the transition from a strong linear instability in a nearly laminar flow below the shock, to a volume-filling convective instability. In all of our simulations, the threshold for explosion lies well within the latter regime. This highlights a basic difference between 1D and 2D explosions: the mechanism is fundamentally non-linear in two dimensions.

4. — Vortical motions with a Mach number ~ 0.3 - 0.5 first appear at the onset of convective instability around the radius of maximal neutrino heating, but before the dipolar mode of the shock reaches its limiting amplitude. These vortices are a source of acoustic waves, which have a similar period to the large-scale oscillation of the shock. Near the

threshold for an explosion, the turbulence in the gain region becomes supersonic, as the existence of widespread secondary shocks attests. These shocks convert turbulent kinetic energy to internal energy, increasing the effective heating rate.

Chapter 5

Explosion Hydrodynamics in One and Two Dimensions

5.1 Overview

In this chapter we explore the dynamics of one- and two-dimensional accretion shocks with neutrino heating, around the threshold for an explosion. We are interested in understanding aspects of the phenomenology observed in more complete collapse calculations which, due to the large number of physical effects involved, are hard to attribute to a single mechanism. In the process, we introduce a number of new methods for measuring the physical properties of the accretion flow.

The literature analyzing explosion hydrodynamics in 1D is extensive and dates back to the very first supernova simulations (see §1.3). The existence of an upper limit to the neutrino heating rate for a steady accretion flow was first pointed out by Burrows & Goshy (1993). More recent parametric collapse calculations have shown that the heating rate required to cause an explosion is generally lower than this upper limit in 2D, and in some cases also in 1D (Murphy & Burrows, 2008). This and other studies have found that the behavior of the system around the critical heating rate for explosion involves a series of

transient fluid motions involving global hydrodynamic instabilities (Buras et al., 2006b; Ohnishi et al., 2006; Scheck et al., 2008). Aside from phenomenological descriptions, these transients in the system are so far not well understood in terms of basic physical principles. A linear stability analysis by Thompson (2000) found that large scale shock expansions are due to a finite amplitude buoyant instability of the postshock flow, but occurrence of this effect has not yet been probed in time-dependent calculations.

Here we report results of numerical experiments performed with our simplified accretion shock model. Starting from the setup previously employed to explore shock oscillations, we gradually add neutrino heating (modelled via eq. 2.6) until an explosion is uncovered.

The plan of the chapter is as follows. In §5.2 we study the behavior of 1D systems, including an explanation for overstable oscillations that precede explosion, the onset of explosion, and the origin of the critical heating rate in spherical symmetry. In §5.3 we address two-dimensional simulations, focusing on the operation of a heat engine in the heating region, the residency time of the fluid, and the morphology of explosion in 2D.

5.2 One-Dimensional Simulations

An explosion in spherical symmetry involves the development of an unstable $\ell = 0$ SASI mode. We showed in §3.4 that, in the absence of neutrino heating, the period of this mode is essentially twice the post-shock advection time. As heating is introduced into the flow, we find that this relation is maintained. The $\ell = 0$ mode is damped until the heating rate is pushed above a critical value, which we now discuss.

It should be emphasized that this critical heating rate is generally lower than that defined by Burrows & Goshy (1993), which marked the disappearance of a steady, spherically symmetric solution to the flow equations. Large amplitude 1D shock oscillations have been witnessed near the threshold for explosion in calculations by Ohnishi et al.

(2006) and Murphy & Burrows (2008). Both calculations employed a realistic EOS, but like us included neutrino heating as a local source term in the energy equation. Oscillations have also been seen by Buras et al. (2006a) in more elaborate calculations with Boltzmann neutrino transport.

The nature of the 1D SASI oscillation was discussed in §3.4. The cycle is stable for $\gamma = 4/3$ and $r_*/r_{s0} = 0.4$. When heating is added, the density profile flattens. This is analog to an increase in γ , which increases the linear growth rates and thus pushes the system towards instability (§3.3). There is a critical heating rate for which the damping effect of the 1D SASI is neutralized and there is no net growth. We find that, once the heating rate exceeds this critical value, the system always explodes.

We therefore define the critical heating rate in our 1D simulations to be the minimum heating rate for growing shock oscillations.¹ Figure 5.1 shows linear eigenfrequencies as a function of heating rate for our 1D initial configurations with constant dissociation. These values were obtained by solving the differential system of Foglizzo et al. (2007), modified to account for a constant rate of nuclear dissociation (§2.4.2) as well as incorporating the heating function in eq. (2.6). The runs marked by stars explode within a time $1000t_{\text{ff0}}$, and so require a small, but finite, positive growth rate.

In an exploding run, expansions become longer and contractions shorter as the shock oscillations become nonlinear. In each contraction, the heating from compression adds to that from neutrinos (which increases with density) and causes an even greater bounce; the behavior is akin to a ball bouncing from the floor which on each bounce receives a greater impulse. Eventually the accretion flow is halted during a contraction. This marks the point of explosion, beyond which the oscillating feedback between the shock and the cooling layer is broken. Material then tends to pile up in the gain region, is further heated, and more material reverses direction. The net effect is to push the shock

¹We define our critical heating parameter H_{cr} to be the average of the values in the exploding and non-exploding runs that are closest to the threshold for explosion, within our fiducial $1000t_{\text{ff0}}$ cutoff.

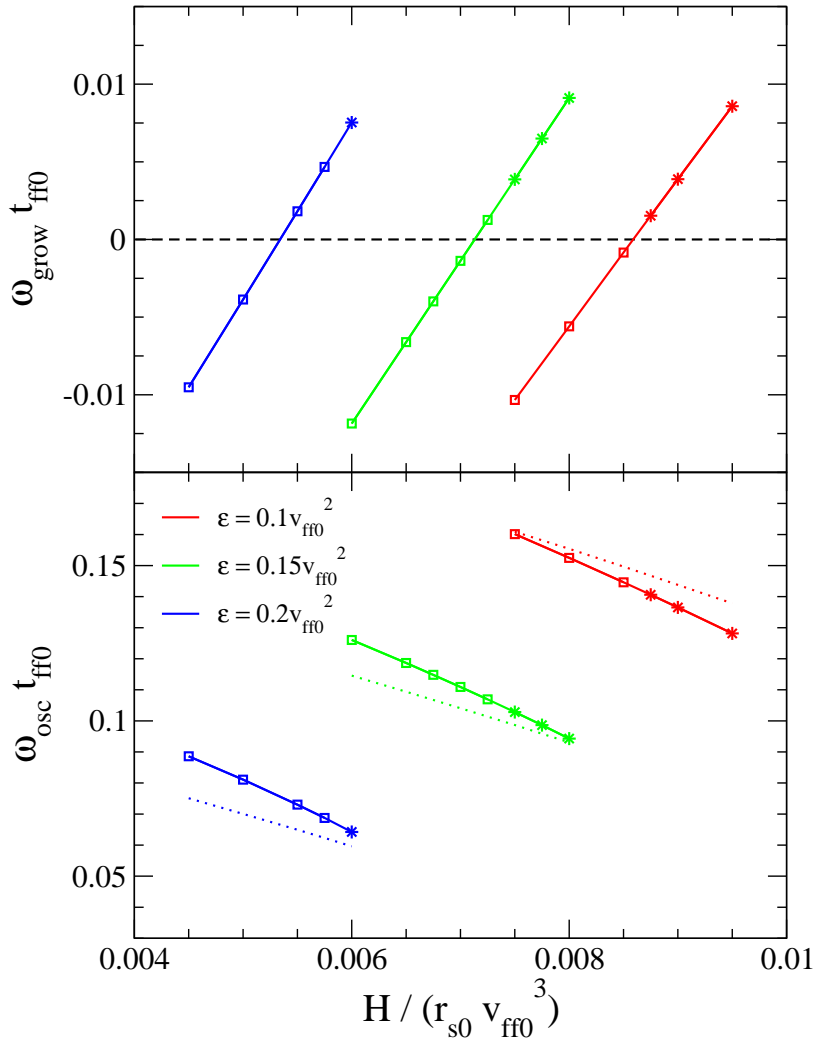


Figure 5.1: Linear growth rates (top) and oscillation frequencies (bottom) of 1D models with constant dissociation energy ϵ , as a function of heating parameter H around the threshold for explosion. Stars denote configurations that explode within $1000t_{\text{ff0}}$. Increased heating makes the system more unstable because the density profile flattens, akin to an increase in γ . Dotted lines show the frequency $\omega_{\text{osc}} = 2\pi/(2t_{\text{adv}})$. Oscillation frequencies decrease with increasing heating rate because r_s moves out relative to r_* , so that the advection time t_{adv} (eq. [3.3]) increases. Increasing the dissociation energy implies a higher relative growth rate for an explosion, because the oscillation period increases with ϵ , and so few oscillations are possible in our fixed time limit.

outward.

We find that this onset of explosion is entirely mediated by neutrino and compressional heating, being independent on whether α -particles are allowed to recombine. This changes as the shock starts running outward; we discuss the details in the next chapter.

5.3 Two-Dimensional Simulations

Extending the flow calculation to two dimensions reveals some subtle patterns of behavior. The time evolution of the shock is shown in the left panel of Fig. 5.2 for a range of heating rates near the threshold for explosion. In contrast with the 1D runs, the breakout of the shock looks similar in models with constant dissociation energy and with NSE between neutrons, protons, and α -particles below the shock (we elaborate on the effects of α -particle recombination in the next chapter). Both types of models are subject to buoyancy-driven instabilities, which allow cold material below the shock to interchange position with hotter material within the gain region. As a result, the shock is highly asymmetric at breakout in both cases.

Around the threshold for explosion, all of our runs develop vigorous convective motions before the SASI has a chance to undergo even a few oscillations. At high heating rates, we find that the convective instability is driven by the negative entropy gradient within the layer of neutrino heating. In non-exploding runs, the shock settles to a quasi-equilibrium state with oscillations taking place over a range of angular (Legendre) index ℓ , as previously seen by Ohnishi et al. (2006), Scheck et al. (2008), and Murphy & Burrows (2008). The amplitude of the $\ell = 1$ and 2 modes remains small until the heating parameter H has begun to exceed about one half the critical value for an explosion.

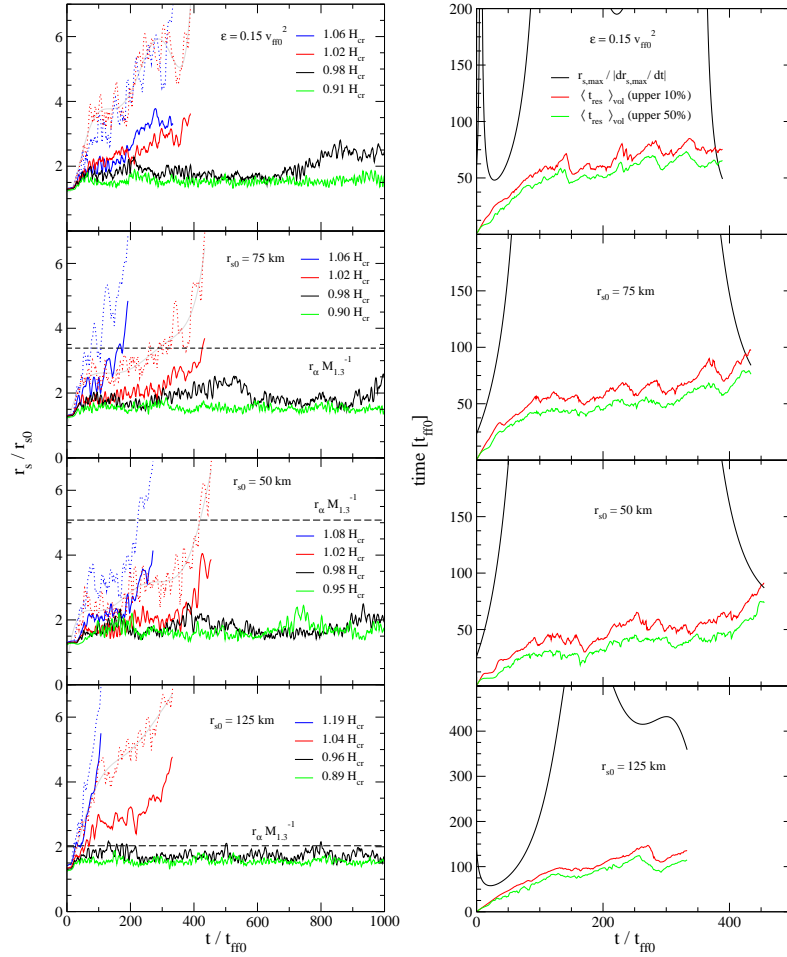


Figure 5.2: Left panel: Angle-averaged shock radius (solid lines) and maximum shock radius (dotted lines) for various 2D models around the threshold for explosion. Upper panel shows runs with constant dissociation energy $\epsilon = 0.15 v_{ff0}^2$, while lower panels displays NSE runs with r_{s0} as labeled. Critical heating rates H_{cr} are different for each configuration, and can be found in Figure 6.10. Right panel: Black lines show expansion timescale of maximum shock radius $t_{exp} \sim r_{s,max} / |dr_{s,max}/dt|$, computed using a polynomial fit for the runs just above the threshold for explosion (corresponding to the grey solid lines on the right panels). Green and red lines show the average residency time over the 50% and 10% of the gain region volume with highest t_{res} , respectively (see §5.3.2 for the definition of this timescale). Shock breakout occurs whenever $t_{exp} \sim \langle t_{res} \rangle_{vol}$, except in the model where recombination heating is dominant ($r_{s0} = 125$ km).

5.3.1 Heat Engine in a Two-Dimensional Explosion

Fresh material that is accreted through an oblique shock has a relatively low entropy, but once it reaches the base of the gain region it is exposed to an intense flux of electron-type neutrinos and is heated. A buoyancy force will push some of this heated material upward, and force an overturn of the fluid below the shock. Material with a longer residency time may therefore undergo multiple episodes of heating. On this basis, Herant et al. (1992, 1994) suggested that a convective flow would mediate a heat engine below the shock that would drive a secular increase in the energy of the shocked fluid.

We now investigate whether a heat engine operates in our simulations, and how it depends on the heating parameter H . We focus on a model with a constant nuclear dissociation energy, $\varepsilon = 0.15v_{\text{ff}0}^2$. In this class of models, the infalling heavy nuclei are completely broken up below the shock, and no heating by the reassembly of α -particles is allowed. As a first step, we average the convective flow over windows of width $50 t_{\text{ff}0}$, which de-emphasizes short term fluctuations in the averaged velocity field $\langle \mathbf{v} \rangle_t$. Figure 5.3 shows $\langle \mathbf{v} \rangle_t$ and $\langle b \rangle_t$ (eq. [2.8]) at four different times in the run with H just above the threshold for explosion ($H = 1.02H_{\text{cr}}$). Two prominent convection cells fill the postshock domain, being separated from each other by a single accretion plume. This configuration is a direct consequence of the artificial symmetries of the flow, since two-dimensional turbulence is known to result in the accumulation of vorticity on the largest spatial scales (e.g., Davidson 2004).

The radius of maximum heating ($r \simeq 0.66r_{\text{s}0}$) coincides with the lower boundary of the convective cells, across which material flows horizontally. Heated fluid is lifted by buoyancy forces and accumulates in the region in between the top of convective cells and the shock. A strong deformation of the shock allows the plume of fresh material to descend diagonally between the convective cells. The tilt of this cold downflow intermittently flips in sign, and the averaged circulation pattern typically has an “ ∞ ” shape. The heating of fluid parcels in the two hemispheres is also intermittent, and sometimes two circulation

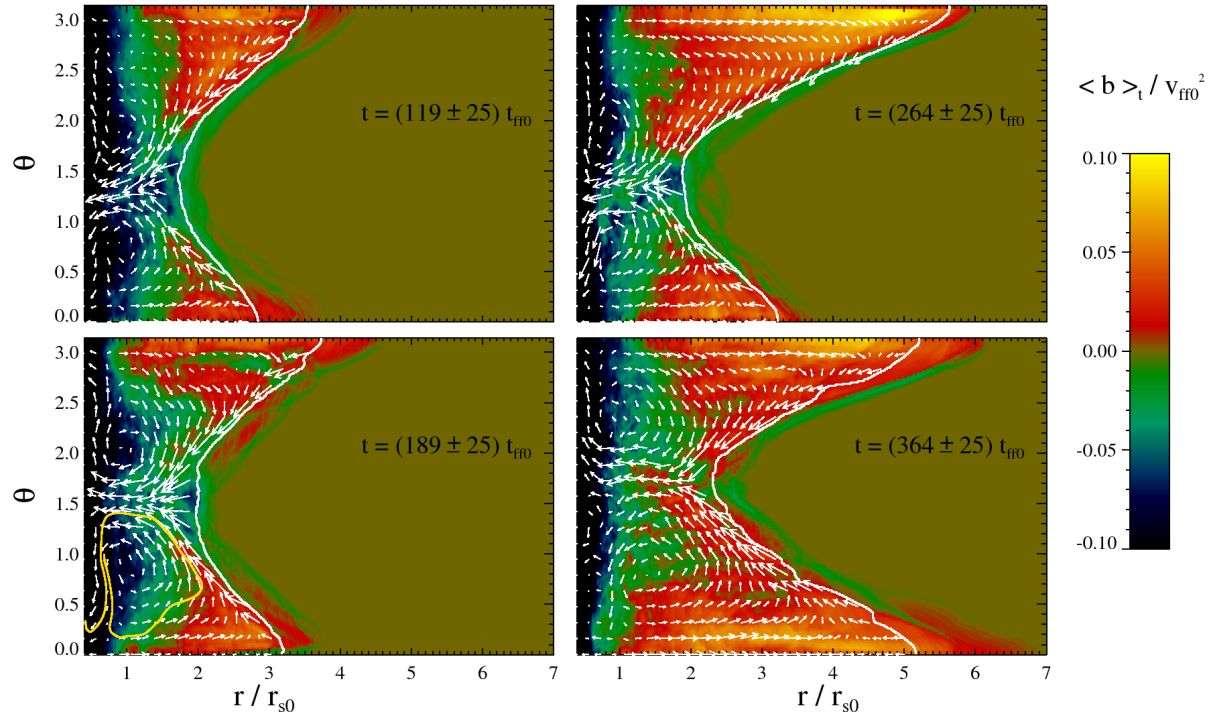


Figure 5.3: Four snapshots of the exploding model with $\varepsilon = 0.15v_{ff0}^2$ and $H = 1.02H_{cr}$. The Bernoulli parameter (color map) and the velocity field (white arrows) are averaged over intervals of duration $50 t_{ff0}$. The thick white contours show the surface with 50% mass fraction in heavy nuclei (time-averaged). The yellow curve in the lower-left panel shows the result of integrating a streamline of this time-averaged velocity field, starting from a point just above the radius of maximum heating. The curve performs an overturn after $\simeq 45t_{ff0}$, and takes an extra $\simeq 8t_{ff0}$ to reach the inner boundary.

flows are established simultaneously, thereby causing a bipolar expansion of the shock.

The accumulation of a bubble of hot material right behind the shock is a consequence of the balance of the buoyancy force acting within the bubble, and the ram pressure of the preshock material. The ratio of force densities is (Thompson, 2000)

$$\frac{F_{\text{buoy}}}{F_{\text{ram}}} \simeq \left(\frac{\rho - \rho_{\text{bubble}}}{\rho} \right) \left(\frac{2GM/r_s}{v_r^2} \right) \Delta\Omega_{\text{bubble}}, \quad (5.1)$$

where r_s is the shock radius, v_r is the ambient radial flow speed, ρ is the ambient density, ρ_{bubble} the density of the bubble, and $\Delta\Omega_{\text{bubble}}$ is its angular size. A low-density bubble

$(\rho - \rho_{\text{bubble}} \sim \rho)$ can resist being entrained by the convective flow once it grows to a size $\Delta\Omega_{\text{bubble}} \sim \mathcal{M}_{\text{con}}^2$ Sr, where \mathcal{M}_{con} is the convective Mach number. On the other hand, the bubble must attain a much larger angular size $\Delta\Omega_{\text{bubble}} \sim 1$ Sr if the buoyancy force is to overcome the upstream ram ($|v_r| \sim v_{\text{ff}}$) and force a significant expansion of the shock surface. Figure 5.3 shows that the extent of the shock expansion is indeed correlated with the angular width of the region where hot material accumulates.

We have identified a useful figure of merit which connects a secular increase in the shock radius to the strength of neutrino heating at the base of the gain region. Figure 5.4 shows the absolute value of the Bernoulli parameter b at the radius of maximum heating ($r_{\text{H,max}} \simeq 0.66r_{\text{s0}}$) as a function of polar angle θ . In the top panel, the four sets of thin solid lines correspond to the four snapshots of Fig. 5.3, and the bottom panel shows the analogous results for a non-exploding run. Overplotted as thick solid lines is the quantity

$$\Theta = \left\langle \frac{\mathcal{L}_H - \mathcal{L}_C}{\rho} \right\rangle_{t, \theta^*, r=r_{\text{H,max}}} \frac{r_{\text{H,max}}}{|\langle v_\theta \rangle_{t, \theta^*}|}. \quad (5.2)$$

This measures the specific energy that is absorbed from neutrinos by the material that flows laterally along the lower boundary of the convective cells. In eq. (5.2), the angular average of the heating rate and meridional velocity is restricted to a single convective cell.²

In non-exploding models, the circulation in the gain region settles to a quasi-steady state, with no net amplification of the mass in material with positive b . The heat absorbed at the base of the convective cells is of the same order of the Bernoulli parameter of the fluid, that is, $\Theta \lesssim |b|$. In an exploding model, Θ will often exceed $|b|$ by a factor 2-3. As is shown in the upper panel of Fig. 5.4, Θ grows with time as the system approaches the explosion.

²To identify the range of angles comprising the lower boundary of a convective cell ($r = r_{\text{H,max}}$), we first average $\langle v_\theta \rangle_t$ over all polar angles, and then define a single cell as a zone where $|\langle v_r \rangle_t| < |\langle v_\theta \rangle_{t, \theta}|$ and v_θ has the same sign. Once the convective cells have been so identified, the angular average is repeated within each cell. The quantity $|\langle v_\theta \rangle_{t, \theta^*}|$ appearing in eq. (5.2) represents this more restricted average, which typically covers ~ 1 rad in the polar direction (e.g., Fig. 5.3).

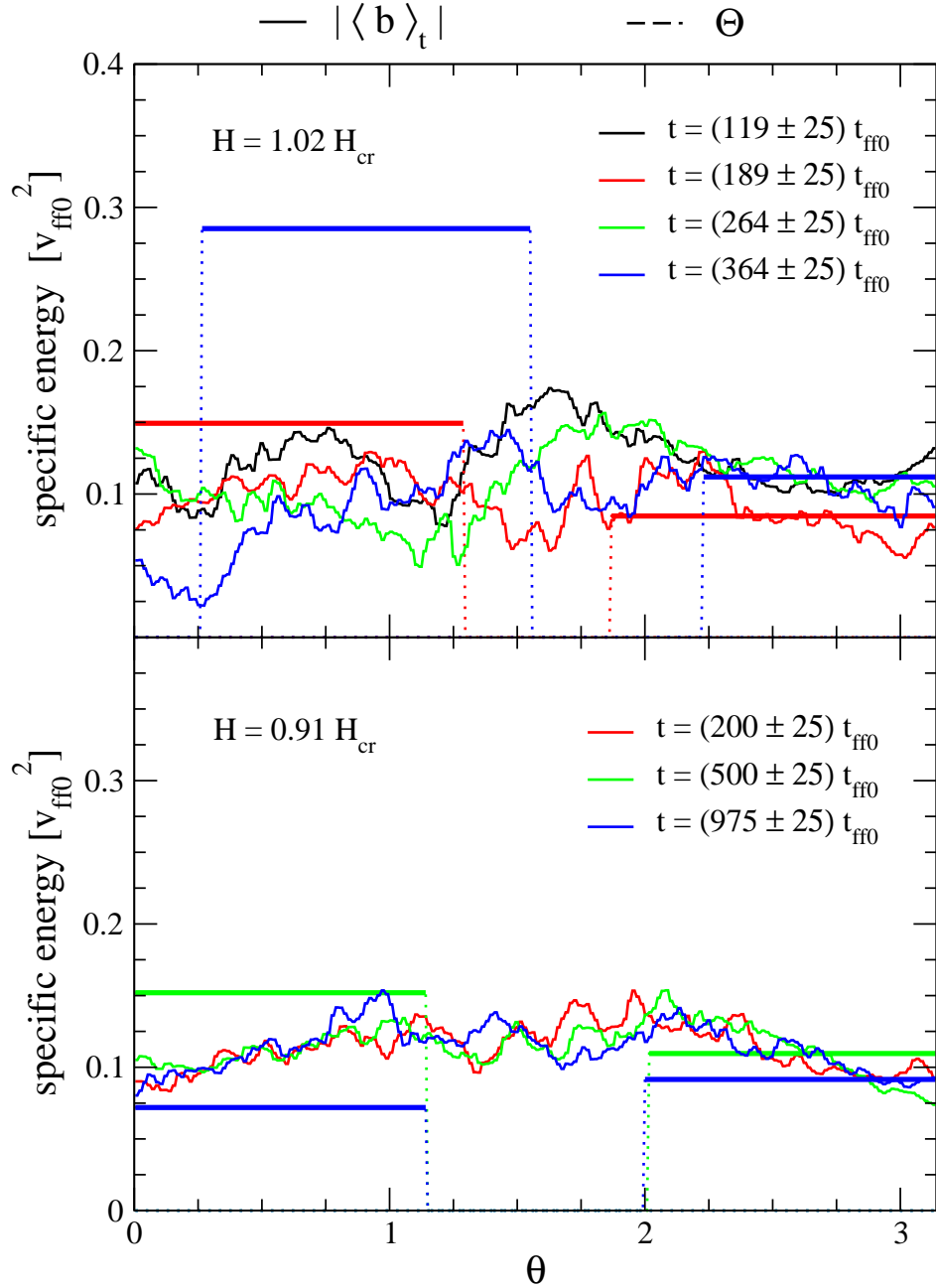


Figure 5.4: Bernoulli parameter (thin solid lines) and specific energy absorbed during lateral advection Θ (eq. [5.2], thick lines) at the radius of maximum heating $r_{H,\max}$ (dotted lines show the boundaries of convective cells). These quantities are averaged over intervals of duration $50 t_{\text{ff}0}$. The upper panel shows the exploding run with $\varepsilon = 0.15 v_{\text{ff}0}^2$ and $H = 1.02 H_{\text{cr}}$ (the same as in Fig. 5.3), and the lower panel shows the non-exploding run with $\varepsilon = 0.15 v_{\text{ff}0}^2$ and $H = 0.91 H_{\text{cr}}$.

Our observation that the bulk of the neutrino heating takes place within horizontal flows suggests that the ratio of heating timescale to radial advection time in the gain layer, usually employed as a measure of closeness to explosions in two-dimensional simulations (e.g., Thompson et al. 2005; Buras et al. 2006a; Scheck et al. 2008; Murphy & Burrows 2008), may be a less precise diagnostic of the conditions for explosion in 2D: the horizontal convective velocity is typically low compared with the downward velocity of the main accretion plume. We do observe that the main accretion plume becomes strongly distorted near the threshold for an explosion, so that a significant fraction of the plume material enters one of the convection cells. This effectively decreases the amount of material that accretes to the protoneutron star and thus increases the overall advection timescale across the gain region.

5.3.2 Residency Time

A long residency time of material in the gain region is commonly viewed as a key ingredient in a successful neutrino-driven explosion. Here we are interested in probing the lifetime of the large scale parcels of hot fluid identified in the previous section. To calculate t_{res} , we use the method described in §2.4.3: we first assign a unique “fluid time” t_F (eq. [2.25]) to each infalling radial mass shell in the simulation, which is effectively the time at which it passes the shock. We then define³ the residency time of the fluid as

$$t_{\text{res}} = t - t_F, \quad (5.3)$$

where t is the present time. A related method (tracer particles) is used by Murphy & Burrows (2008) to calculate the residency time in collapse simulations with a more realistic EOS.

³Since t_F is defined in terms of the angle-averaged radius of the shock, there is a modest error in t_F due to non-radial deformations of the shock. Given the lack of substantial large-scale mixing between the single accretion funnel and convective cells, this prescription serves well as a tracer of different fluid populations.

As material with positive Bernoulli parameter accumulates below the shock, we indeed find that its t_{res} grows larger. The shock starts running outward if the energy of this unbound material grows on a timescale shorter than the convective time. The right panel of Figure 5.2 shows the characteristic expansion time of the shock $t_{\text{exp}} \sim r_{s,\text{max}}/|dr_{s,\text{max}}/dt|$ (as measured at its outermost radius), alongside $\langle t_{\text{res}} \rangle_{\text{vol}}$ (as measured within the material comprising the upper part of the residency time distribution). The final breakout of the shock seen in the left panel of Fig. 5.2 corresponds to the time when $t_{\text{exp}} \sim \langle t_{\text{res}} \rangle_{\text{vol}}$. The breakout is a bit more gradual in the $r_{s0} = 125$ km model with heating just above threshold for an explosion ($H = 1.04H_{\text{cr}}$). In this case, the expansion time of the shock remains somewhat longer than the residency time of material below the shock, which implies that the breakout depends on the continuing release of nuclear binding energy as well as on the separation of positive-energy fluid from the accretion flow.

The lengthening of the mean residency time can largely be ascribed to the increased dynamical time of the expanding shock. What changes most dramatically during breakout is the *ratio* of the expansion time to the dynamical time. Note that large changes in the distribution of t_{res} are concentrated in regions of positive b . In Fig.5.5, we plot the distribution of b and t_{res} in the $\varepsilon = 0.15v_{\text{ff0}}^2$ run that is just above the threshold for an explosion (see Fig. 5.3). Regions with small or negative residency time represent freshly injected fluid. The distribution is stratified in b around $t_{\text{res}} \sim 40t_{\text{ff0}}$ (which is approximately an overturn period of a convective cell, see §5.3.1 and Figure 5.3). Material with more negative b resides on average at a smaller radius. Fluid with a longer residency time has mostly positive b , corresponding to material transported upwards by convective cells.

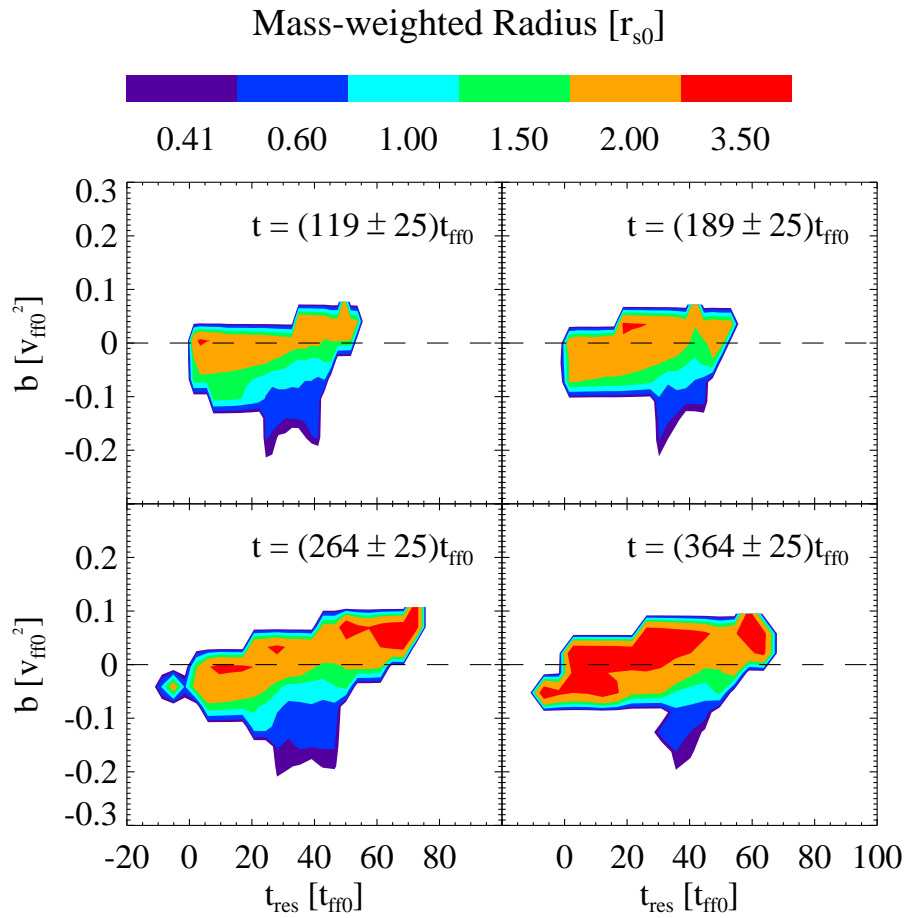


Figure 5.5: Histogram of Bernoulli parameter b and residency time t_{res} in the exploding run with $\varepsilon = 0.15v_{\text{ff0}}^2$ (see also Fig. 5.3). The colors label the mass weighted radius, and we include all material experiencing a net excess of neutrino heating over cooling.

5.4 Summary

In this chapter we have investigated the dynamics of one- and two-dimensional time dependent simulations of an accretion shock with neutrino heating around the threshold for an explosion. Our main results are the following:

1. – The large-amplitude oscillations that are seen in 1D runs near an explosion are the consequence of the $\ell = 0$ SASI as modified by heating. In contrast with the $\ell = 1, 2$ modes of a laminar accretion flow, the period of these oscillations is close to twice the post-shock advection time. The critical heating rate for an explosion (assuming constant mass accretion rate, neutrino luminosity, and inner boundary) corresponds to neutral stability for the $\ell = 0$ mode.
2. – Non-spherical deformations of the shock are tied to the formation of large-scale plumes of material with positive energy. Our two-dimensional explosions with a super-critical heating rate involve a large-scale convective instability that relies on the accumulation of vorticity on the largest spatial scales. Volume-filling convective cells are apparent in a time-averaged sense. Transient heating events create positive-energy material that accumulates in between the convective cells and the shock. A significant fraction of the heating occurs in horizontal flows at the base of the convective cells, which are fed by a dominant equatorial accretion plume. If the heating parameter is large enough, this results in an amplifying cycle and explosion.

Chapter 6

Effects of Alpha-Particle

Recombination on Explosion

Hydrodynamics

6.1 Overview

In this chapter we examine the effect of alpha particle recombination on the dynamics and critical neutrino heating rate in one- and two-dimensional systems. Even though the finite-temperature equations of state used in core-collapse calculations include the effect of nuclear dissociation and recombination in the internal energy of the fluid (e.g., Lattimer & Swesty 1991), the effect of this energy source on the dynamics of the postshock flow has received little attention in numerical studies.

Bethe (1993) pointed out that when the shock expands to a radius close to r_α (equation 2.1), its temperature decreases below $T \sim 1$ MeV and nucleons recombine into α -particles. This releases enough energy to unbind the fluid and propel the shock outwards (see also Bethe 1996). This effect is enhanced due to the fact that the ram pressure upstream of the shock decreases with increasing distance from the collapsed core (Bethe,

1997). More recently, Marek & Janka (2009) have found evidence for a neutrino-driven explosion of a $15M_{\odot}$ progenitor at late times (~ 0.6 s), powered in part by the recombination of α -particles, in a 2D simulation. The two-dimensional semi-realistic collapse calculations of Murphy & Burrows (2008) show a sudden acceleration of the shock in exploding runs when the shock reaches a radial position ~ 250 km.

Here we intend to quantify the effect of nuclear energy generation in the shock dynamics by comparing models with constant nuclear dissociation, which do not allow recombination, and the more realistic NSE prescription (see §2.2.1). We focus on the relative contributions of neutrino heating and α -particle recombination to shock breakout, their spatial distribution, and the dependence of the critical neutrino heating rate for explosion on the nuclear energy generation rate.

The chapter is organized as follows: §6.2 addresses one-dimensional simulations, §6.3 the dynamics in 2D, and §6.4 the critical heating rate in both cases.

6.2 One-Dimensional Simulations

The onset of explosion in our model is controlled entirely by neutrino and compressional heating (§5.2). Here we focus on the dynamics of the flow once the shock has started moving away from the star. Shock breakout is controlled by the build-up of positive-energy fluid downstream of the shock, and therefore is sensitive to the density profile. Heating by neutrinos is concentrated fairly close to the protoneutron star, inside a distance $\sim (2 - 3)r_*$. Heating by α -particle recombination is concentrated at a greater distance $\sim r_{\alpha}$ (eq. [2.1]), but still can reach a comparable amplitude.

The dependence of shock breakout on heating rate is displayed in Fig. 6.1 for two accretion models and several values of H close to H_{cr} (see Table 2.2). The initial expansion of the shock during the explosion phase is very similar for models with constant ε and with NSE in the shocked fluid. However, the time evolution bifurcates near the radius

r_α .

Figure 6.2 shows successive profiles of the shocked flow in the exploding run with $H = 1.09H_{\text{cr}}$ and $r_{s0} = 75$ km. The α -particle fraction approaches unity as the shock reaches the radius r_α . The second panel shows the specific nuclear energy generation rate [eq. (2.15)] normalized to the adiabatic rate of change of the enthalpy,

$$w_{\text{ad}} = \frac{1}{\rho} \frac{dp}{dt} = -c_s^2 \nabla \cdot \mathbf{v}. \quad (6.1)$$

Here $c_s = (\gamma p/\rho)^{1/2}$ is the sound speed. The third panel compares the amplitude and distribution of neutrino and recombination heating, and the bottom panel plots the radial velocity in the postshock region.

We can summarize this behavior as follows: during the initial expansion phase, fluid below the shock continues to move inward, and the dissociation of α -particles removes energy from the flow (as expected from eq. [2.7]). Some fluid behind the shock begins to move outward around $300t_{\text{ff0}}$, but nuclear dissociation still causes a net loss of internal energy. However, the recombination of α -particles sets in above r_α , especially in regions where $X_\alpha \lesssim 0.5$. By the time the shock hits the outer boundary, de_{nuc}/dt exceeds one-half of $|w_{\text{ad}}|$.

The dependence of the density contrast κ (eq. [2.10]) on radius also has an influence on the details of breakout. When the dissociation energy ε is held fixed, κ increases toward larger radius. This has the effect of creating a dense layer of fluid below the shock when r_s is such that $\varepsilon \sim v_{\text{ff}}^2/2$. In spherical symmetry, the breakout of the shock is then impeded by the accumulation of a dense layer of material that cannot exchange position with the lighter material below it. It can happen that the energy in the expanding region is no longer able to sustain the heavier material above, and the shock collapses, as shown in Fig. 6.1 for the constant ε run with $H = 1.08H_{\text{cr}}$. This obstruction is avoided when statistical equilibrium between neutrons, protons, and α -particles is maintained below the shock, because ε/v_1^2 and κ both decrease gradually as the shock expands to distances much larger than r_{s0} (Fig. 2.1). This limit to the shock expansion does not occur in

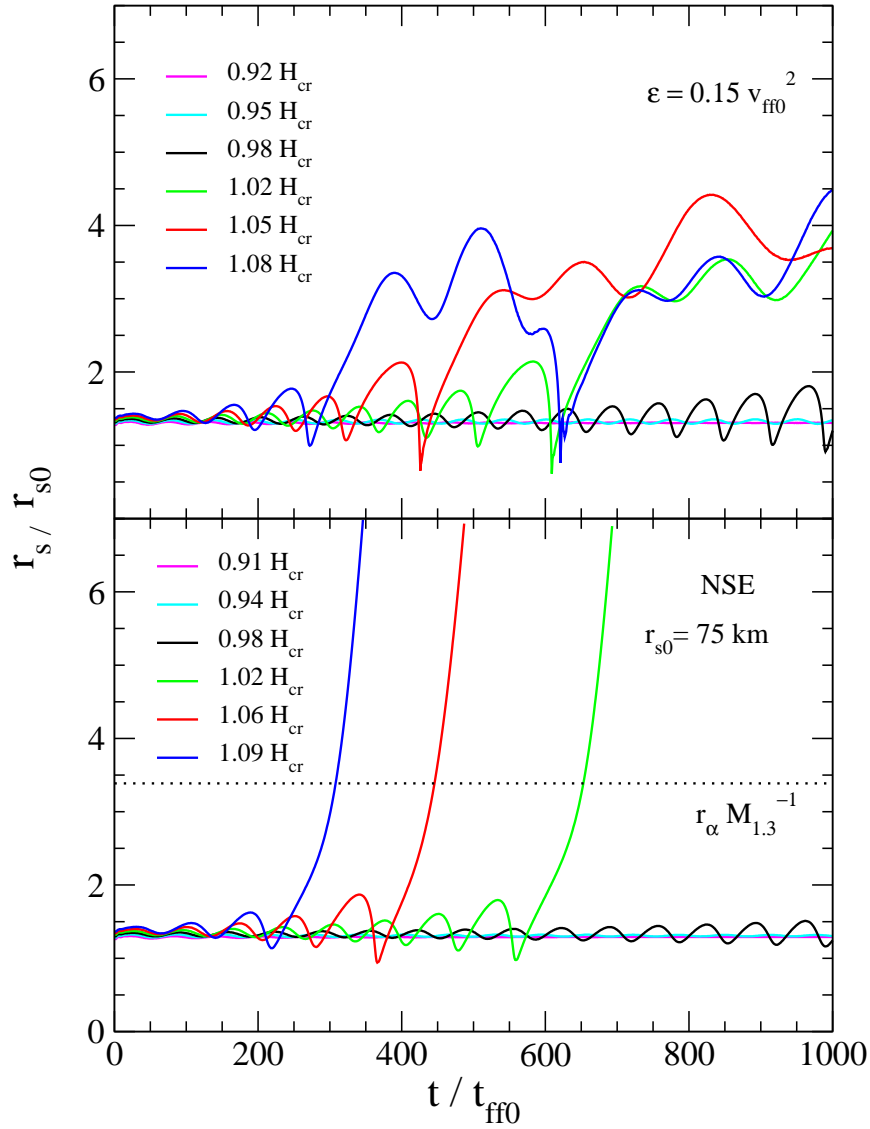


Figure 6.1: Shock radius as a function of time for two sequences of 1D simulations. The upper panel shows runs with constant dissociation energy $\varepsilon = 0.15 v_{ff0}^2$, and a range of heating coefficients H near the critical value $H_{cr} = (0.006625 \pm 0.000125) v_{ff0}^3 r_{s0}$. The lower panel shows runs with $r_{s0} = 75 \text{ km}$ and an α -particle contribution to the EOS. In this case, X_α^{eq} is initially negligible everywhere below the shock (see Table 2.2), but grows as the shock expands. The horizontal dotted line labels the radius r_α at which the nuclear binding energy Q_α of an α -particle equals its gravitational binding energy (eq. 2.1). The critical heating for this second sequence is lower, $H_{cr} = (0.006125 \pm 0.000125) v_{ff0}^3 r_{s0}$.

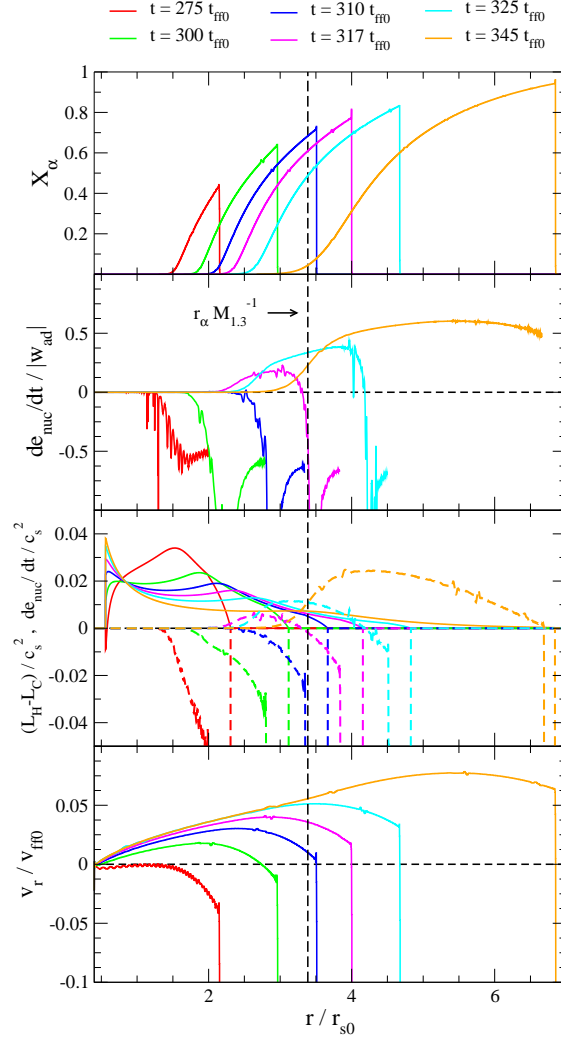


Figure 6.2: Radial profiles of various quantities during shock breakout in the NSE model with $H = 1.09H_{\text{cr}}$ and $r_{s0} = 75$ km (Fig. 6.1). Top panel: mass fraction of α -particles. Second panel: rate of release of specific nuclear binding energy de_{nuc}/dt compared with the (adiabatic) rate of change of enthalpy w_{ad} [eq. 6.1]. Third panel: net neutrino heating rate per unit volume $\mathcal{L}_H - \mathcal{L}_C$ (thin curves) and de_{nuc}/dt (thick dashed curves), both normalized to the local value of $c_s^2 = \gamma p/\rho$. Bottom panel: radial velocity normalized to v_{ff0} at radius r_{s0} . Both de_{nuc}/dt and w_{ad} are smoothed in radius for clarity.

2D, as this situation would be Rayleigh-Taylor unstable (dense fluid over light fluid is unstable on the dynamical time t_{ff0}).

6.3 Two-Dimensional Simulations

In the previous chapter we discussed how neutrino heating can result in the accumulation of large scale parcels of hot fluid behind the shock, driving a secular expansion through buoyancy forces (§5.3.1). Here we focus on the relative contributions of neutrino heating and α -particle recombination to the subsequent expansion of the shock, as well as their spatial distribution.

One gains considerable insight into the mechanism driving shock breakout by examining the distribution of Bernoulli parameter (eq. [2.8]) in the shocked fluid. We first consider the NSE runs with $r_{s0} = 50$ km and 125 km, with the heating parameter H just above the threshold for an explosion. Two snapshots from each of these runs are shown in Figs. 6.3 and 6.4. In the first case, the initial equilibrium shock radius is only $\sim r_\alpha/4$ km, and α -particles are essentially absent below the shock. In the second, the shock starts at $\sim 2r_\alpha/3$ and $X_\alpha \sim 0.5$ initially in the postshock flow.

Large deformations of the outer shock are generally caused by convective plumes that carry positive energy. Strong neutrino heating is generally concentrated inside the inner bound ($b < 0$) zone. The degree of symmetry of the bound material depends on the α -particle abundance. In the $r_{s0} = 125$ km run, the bound region is spherically stratified and the material with $b > 0$ is generally excluded from it. Strong recombination heating is present both below and above the surface where $b \simeq 0$, indicating that it is mainly responsible for imparting positive energy to the shocked material. The mean shock radius expands by a factor ~ 2.5 between the two frames in Fig. 6.4, but the growth in the volume of positive-energy material is not accompanied by a significant expansion of the inner bound region, whose outer radius remains fixed at $r \simeq r_\alpha$. This segregation

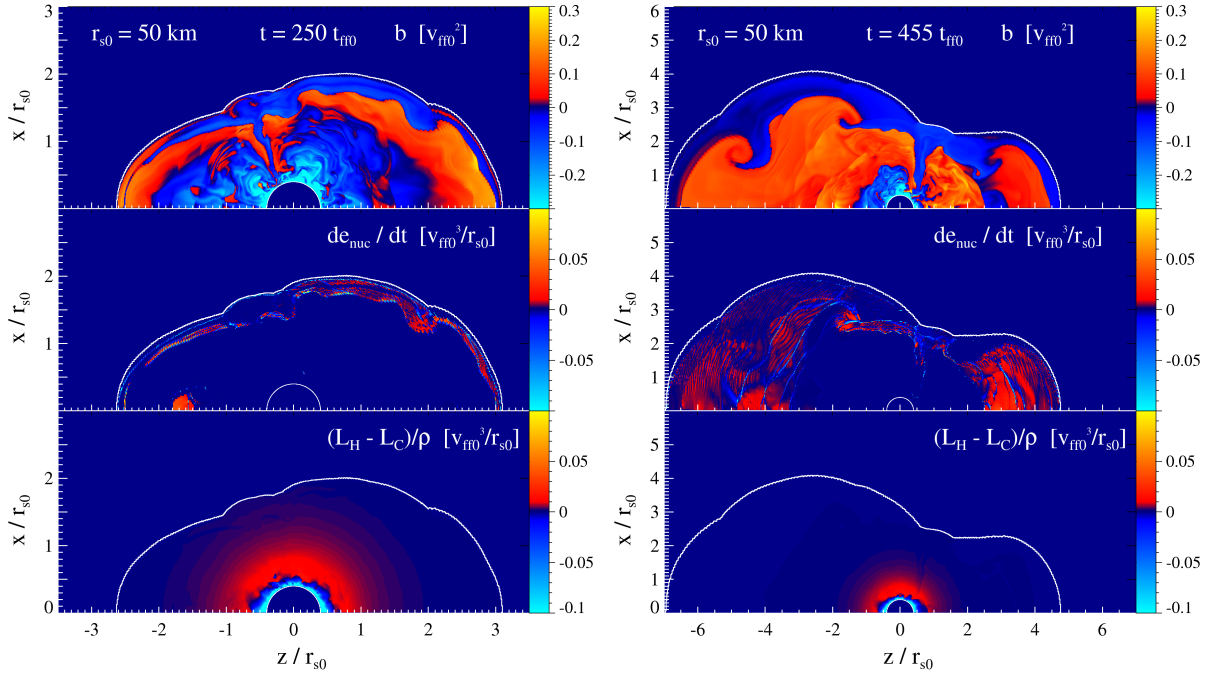


Figure 6.3: Snapshots in the evolution of the NSE run with $r_{s0} = 50$ km, well inside r_α , just above the threshold for an explosion. Within each panel, the top figure displays Bernoulli parameter b ; the middle figure the rate of change of nuclear binding energy per unit mass; and the bottom figure the net neutrino heating rate per unit mass. Left: α -particles begin to form as the shock approaches r_α in the $r_{s0} = 50$ km run, but neutrino heating remains much stronger than recombination heating. Right: the same run just before the shock hits the outer boundary. When the shock starts off well inside r_α , neutrino heating dominates the initial expansion, and material with $b > 0$ forms well inside r_α (see §5.3.1).

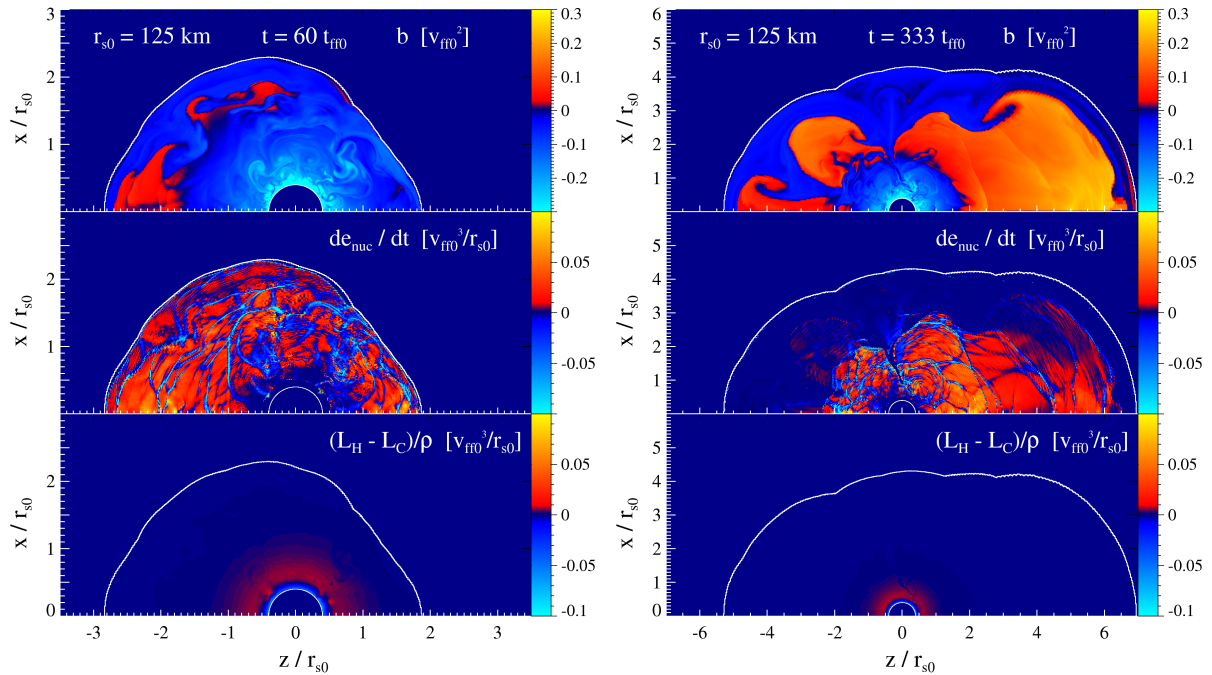


Figure 6.4: Same as Figure 6.3, but now showing the NSE run with $r_{s0} = 125$ km, close to r_α , just above the threshold for an explosion. Left: the early development of an asymmetric plume with positive b . Right: the same run just before the shock hits the outer boundary. In this $r_{s0} = 125$ km run, the heating by α -particle recombination is enhanced with respect to neutrino heating due to the large X_α in the initial stationary model. Recombination heating straddles the central zone with $b < 0$, which maintains a nearly spherical boundary near the radius $r_\alpha (\simeq 2.0 r_{s0})$.

of bound from unbound material is broken when the shock is more compact initially, as is seen in the two panels of Fig. 6.3. A single dominant accretion plume is continuously present, which funnels cold and dense material into the zone of strong neutrino heating. Alpha-particles are present only well outside the boundary between $b < 0$ and $b > 0$.

The relative strength of neutrino heating and recombination heating depends on the initial radius of the shock, and on the Bernoulli parameter of the postshock material. Figure 6.5 separates out cooling by α -particle dissociation from heating by recombination and neutrino radiation during the pre-explosion quasi-steady state (leftmost panels), the onset of explosion (second panel left to right), and shock breakout (two rightmost panels). [See Figure 5.2 for comparison.] The colored curves separate out the positive, negative, and net contributions from nuclear energy generation. The sharp negative spike near $b = 0$ represents α -particle dissociation in fresh, cold downflows. The formation of material with $b > 0$ is primarily due to α -particle recombination in the $r_{s0} = 125$ km run. As the initial radius of the shock is reduced with respect to r_α , neutrino heating makes a proportionately larger contribution near breakout.

The strength of the boost given to the shock by recombination heating can be gauged by comparing de_{nuc}/dt to the adiabatic rate of change w_{ad} of the enthalpy of the flow (eq. [6.1]). Figure 6.6 shows the result for all three NSE sequences with H just above H_{cr} . In all cases, $de_{\text{nuc}}/dt \simeq w_{\text{ad}}$ in various parts of the shocked fluid once the shock extends beyond a radius $\simeq r_\alpha$, just as in 1D. Most of the heat input by recombination is concentrated where $X_\alpha \sim 0 - 0.5$.

Strong recombination heating quite naturally extends below the zone where α -particles are present in significant numbers, as is seen in Fig. 6.7. The first and third panels of this figure depict the pre-explosion steady state of the $r_{s0} = 75$ km model with $H = 1.02H_{\text{cr}}$, while the second and fourth panels show the last time before the shock hits the outer boundary. At the latter time, one sees that the strongest recombination heating is concentrated in a layer where $X_\alpha \lesssim 0.5$, at the base of the extended α -rich plumes. Just as

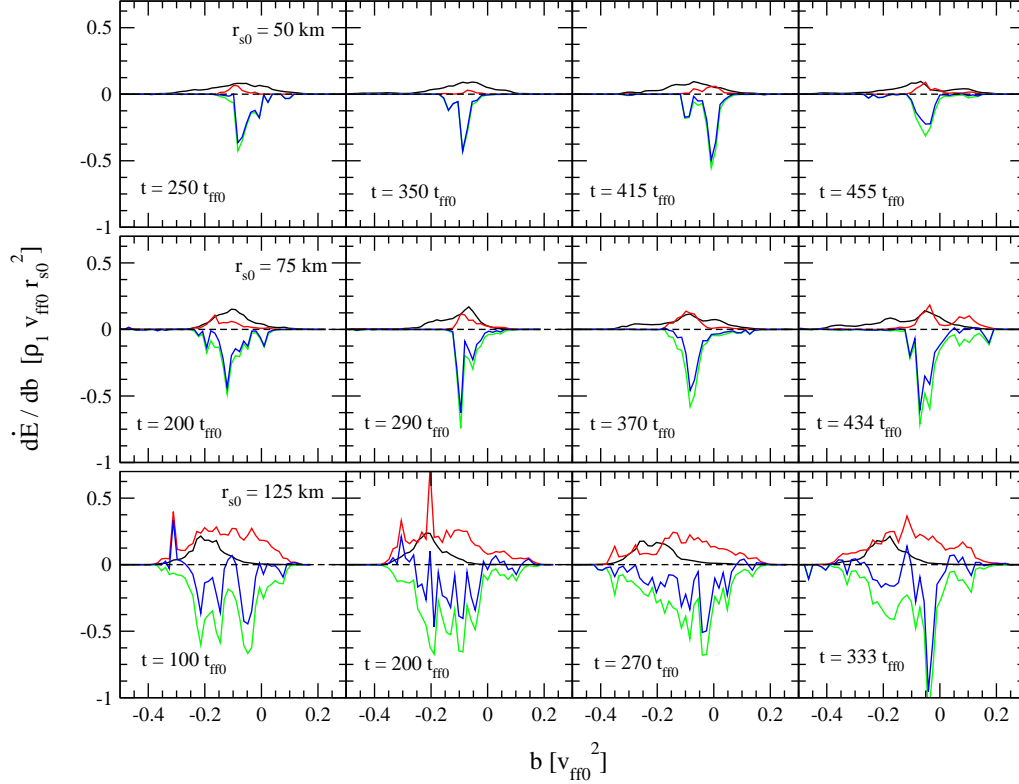


Figure 6.5: Heating rate of material, as distributed with respect to Bernoulli parameter b . This illustrates the relative importance of neutrino heating and nuclear dissociation/recombination in hot and cold parts of the flow. We restrict attention to material in the gain region (defined by $\mathcal{L}_H > \mathcal{L}_C$) in the three 2D NSE runs just above the threshold for explosion. Four snapshots are shown: the pre-explosion quasi-steady state (leftmost), onset of explosion (second from left to right), and breakout (third and fourth). Black curves: net heating rate resulting from neutrino absorption and emission. Red/green curves: heating/cooling rate by α -particle recombination and dissociation in material with $de_{\text{nuc}}/dt > 0$ and $de_{\text{nuc}}/dt < 0$, respectively. Blue curves: net heating/cooling rate due to changing α -particle abundance. The sharp negative spike near $b = 0$ represents α -particle dissociation in fresh, cold downflows. The formation of material with $b > 0$ is primarily due to α -particle recombination in the $r_{s0} = 125$ km run. As the initial radius of the shock is reduced with respect to r_α , neutrino heating makes a proportionately larger contribution near breakout.

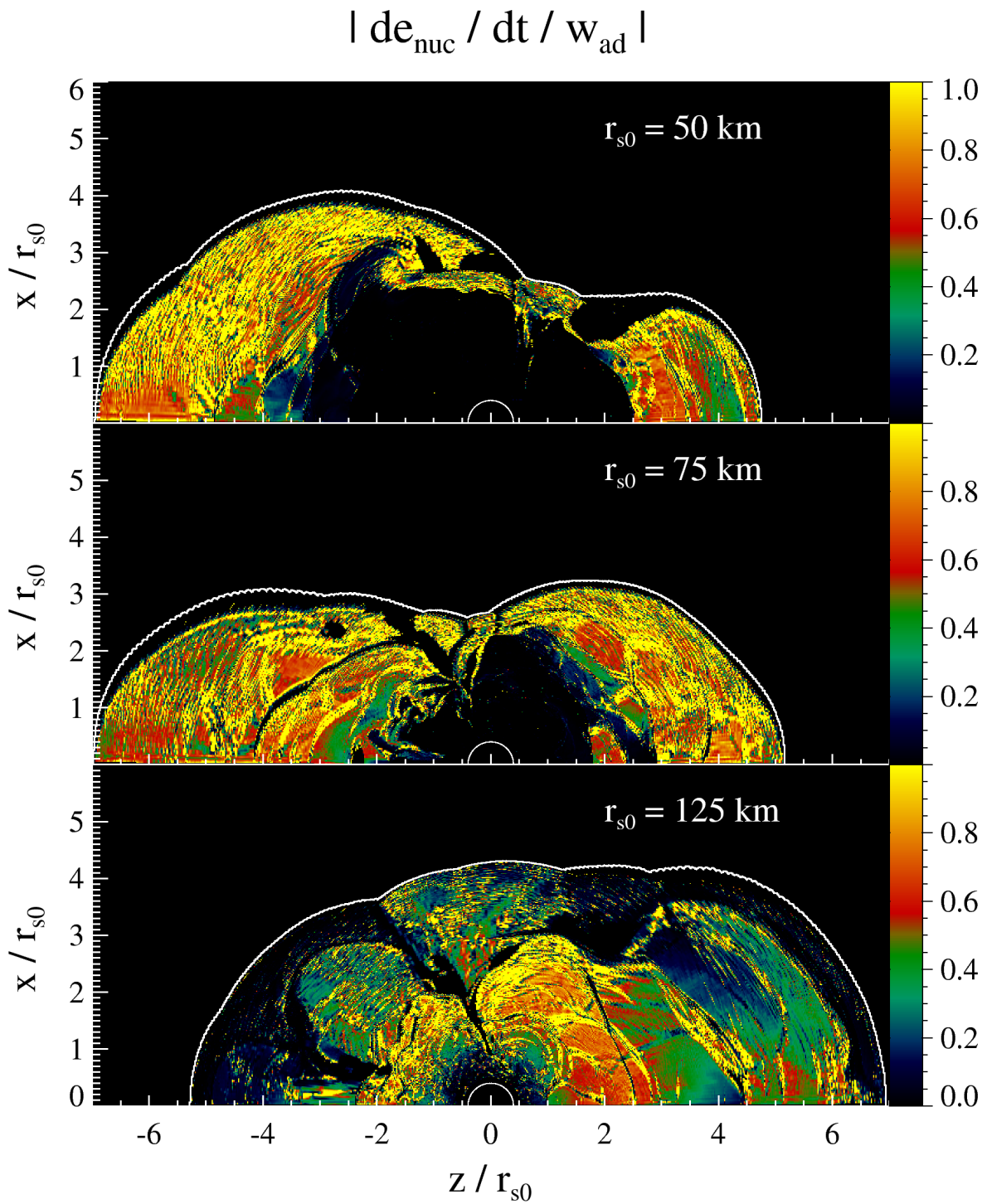


Figure 6.6: Ratio of de_{nuc}/dt (rate of release of specific nuclear binding energy, eq. [2.15]) to w_{ad} (adiabatic rate of change of the enthalpy, eq. [6.1]) for the three NSE models with H just above H_{cr} .

in the 1D simulations (e.g. Fig. 6.2), X_α approaches unity during shock breakout.

Histograms of de_{nuc}/dt versus b and X_α are shown in Fig. 6.8. The rapid dissociation of α -particles in fresh downflows is represented by the long tail toward large negative values of de_{nuc}/dt , showing that nuclear energy generation constitutes a net energy sink of the system. The α -particle concentration is very stratified, with higher X_α occurring at larger radius. Most of the mass with positive Bernoulli parameter is located at large radii. It is also apparent from Fig. 6.8 that material with a longer residency time tends to have *lower* X_α , as is expected because it also tends to have a higher temperature. Before the shock gets close to a radius r_α , most of the shocked material has negative Bernoulli parameter and $t_{\text{res}} \lesssim 50t_{\text{ff0}}$, pointing to material lingering for about one convective overturn.

Another interesting feature of Fig. 6.4 is the presence of secondary shocks, which are triggered once the outer shock becomes significantly non-spherical. Their locations are marked by discrete jumps in the rate of recombination heating. Secondary shocks are also prevalent throughout the nonlinear phase in the constant- ε models. Figure 6.9 shows the normalized pressure gradient $(r/p)|\nabla p|$ for collapse models of both types, when H is just above threshold for an explosion (right before the shock hits the outer boundary of the simulation volume). In both cases, secondary shocks extend over the whole postshock domain, signaling the dissipation of supersonic turbulence which is stirred by accretion plumes that penetrate into the gain region.

6.4 Critical Heating Rate for Explosion

An explosion occurs when the heating parameter H is raised above a critical value¹ H_{cr} . We now explore how H_{cr} depends on the details of the EOS and the initial radius of the shock. One can express H simply in terms of the ratio of the heating rate ($4\pi r^3 \mathcal{L}_H$) to the accretion luminosity ($GM\dot{M}/r$), in the idealized (but unrealistic) case where the flow

¹Our method for determining H_{cr} is discussed in §5.2.

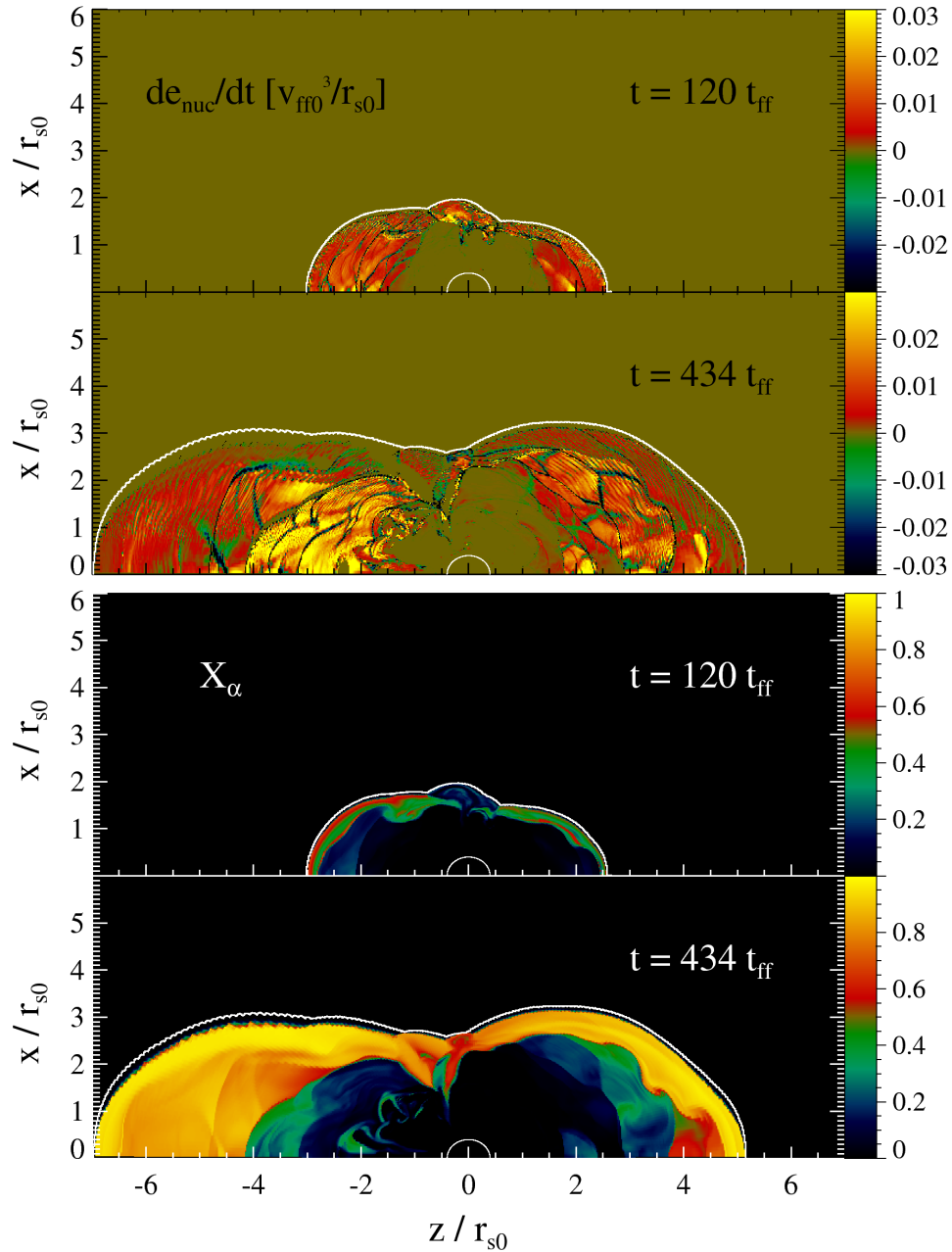


Figure 6.7: Top panels: rate of release of specific nuclear binding energy de_{nuc}/dt . Bottom panels: mass fraction of α -particles X_{α} . We show two instants in the exploding NSE run with $r_{\text{s0}} = 75$ km and $H = 1.02H_{\text{cr}}$. The shock contour is approximated by the white line which marks $X_{\text{O}} = 90\%$.

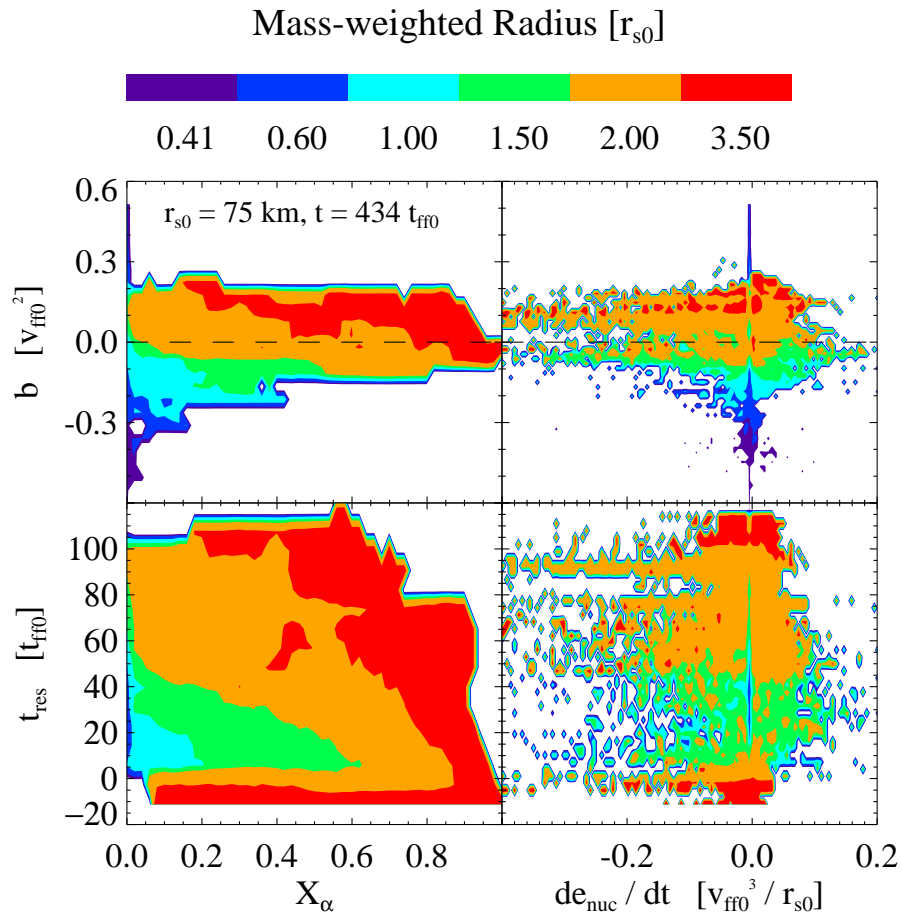


Figure 6.8: Histogram of Bernoulli parameter b and residency time t_{res} versus α -particle mass fraction X_α and rate of release of specific nuclear binding energy de_{nuc}/dt , in the exploding run with $r_{s0} = 75 \text{ km}$ (Fig. 6.7).

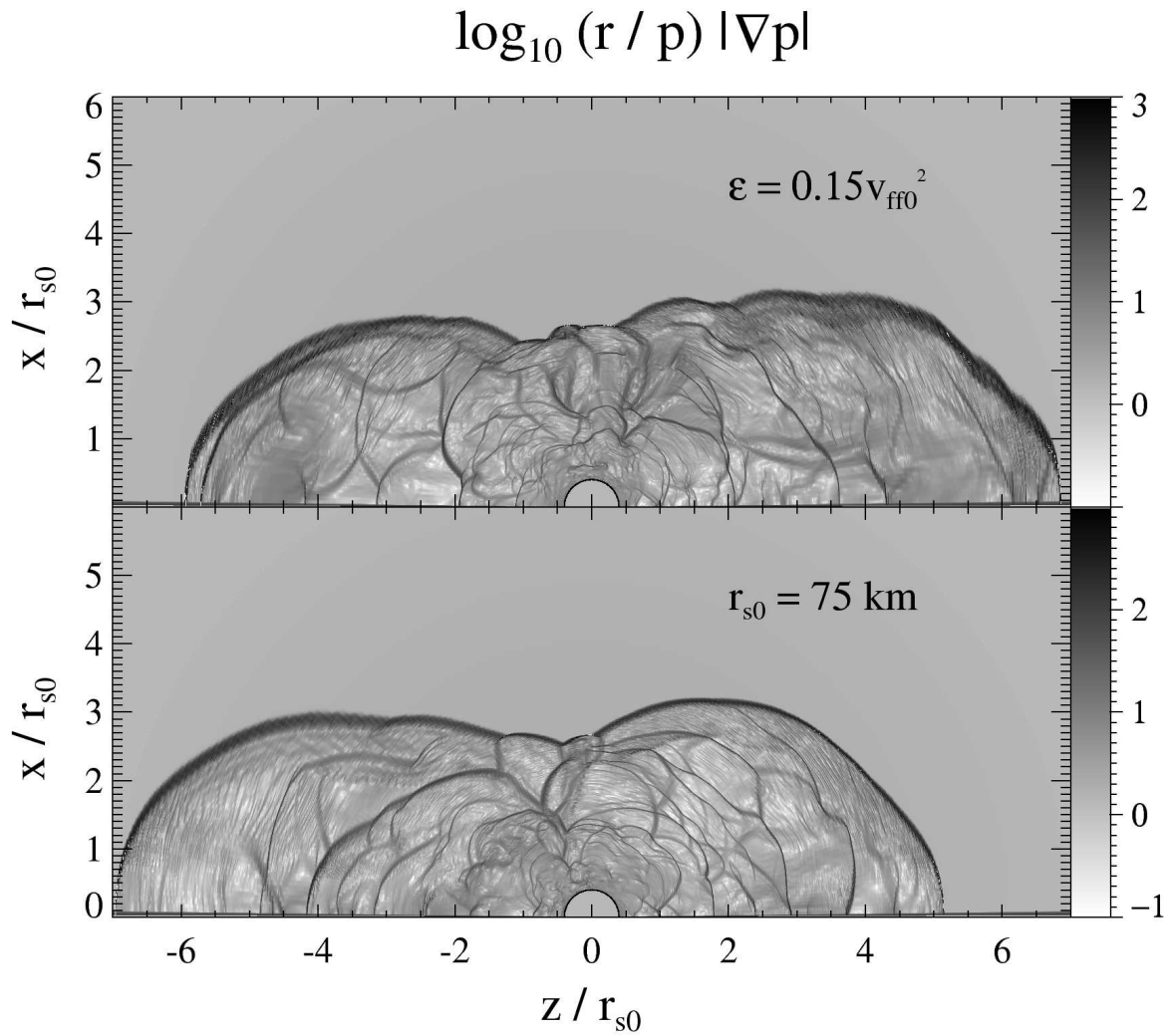


Figure 6.9: Normalized pressure gradient $(r/p)|\nabla p|$ showing the secondary shock structure during breakout. The top model is $\varepsilon = 0.15v_{\text{ff}0}^2$ and the bottom NSE with $r_{\text{s}0} = 75 \text{ km}$. Both have heating rates just above the threshold for an explosion.

is composed only of free nucleons and moves hypersonically. Then this ratio depends on H but not on the accretion rate $\dot{M} = 4\pi r^2 \rho(r) |v_{\text{ff}}(r)|$. The precise value of the reference radius is unimportant; we choose r_{s0} , the shock radius in the time-independent, spherical flow solution at $H = 0$. Then

$$\frac{4\pi r_{s0}^3 \mathcal{L}_H[\rho_1(r_{s0})]}{GM\dot{M}/r_{s0}} \Big|_{X_\alpha=0; \mathcal{M}=\infty} = \frac{2H}{r_{s0} v_{\text{ff}0}^3}. \quad (6.2)$$

This quantity is $\sim 10^{-3} - 10^{-2}$ in the models we examine, which are below or near the threshold for explosion.

Note that the cooling in our model is concentrated at the base of the settling flow. As a result, the width of the gain region (relative to the shock radius) does not change significantly between different models. The critical heating parameter is therefore only indirectly related to the amplitude of the cooling function through the structure of the settling flow below the shock. Our purpose here is to explore how the critical heating rate depends on the strength of the gravitational binding of the shocked fluid to the collapsed core, and on the abundance of alpha particles.

Figure 6.10 displays H_{cr} for all of our model sequences. The abscissa is ε/v_1^2 , where ε is the nuclear dissociation energy and v_1 is the flow speed upstream of the shock in the initial configuration (that is, in the time-independent, spherical flow solution). In the case of the NSE equation of state, this quantity can be translated into an initial value of the shock radius using Fig. 2.1. (Note that ε/v_1^2 has a weak dependence on r_s in the NSE sequence.)

A few interesting features of Fig. 6.10 deserve comment. First, a comparison with Table 2.2 shows that the critical heating rate for explosion is $\sim 50 - 70\%$ of the maximum heating rate for which a steady-state flow solution can be found. The maximal heating parameter H_{steady} for a steady flow corresponds directly to the one first determined by Burrows & Goshy (1993) using a more realistic EOS. Note also that the values of H_{cr} in the 1D and 2D models are much closer to each other than they are to H_{steady} . This result is perhaps not surprising, given that the explosion is not immediate, but is approached

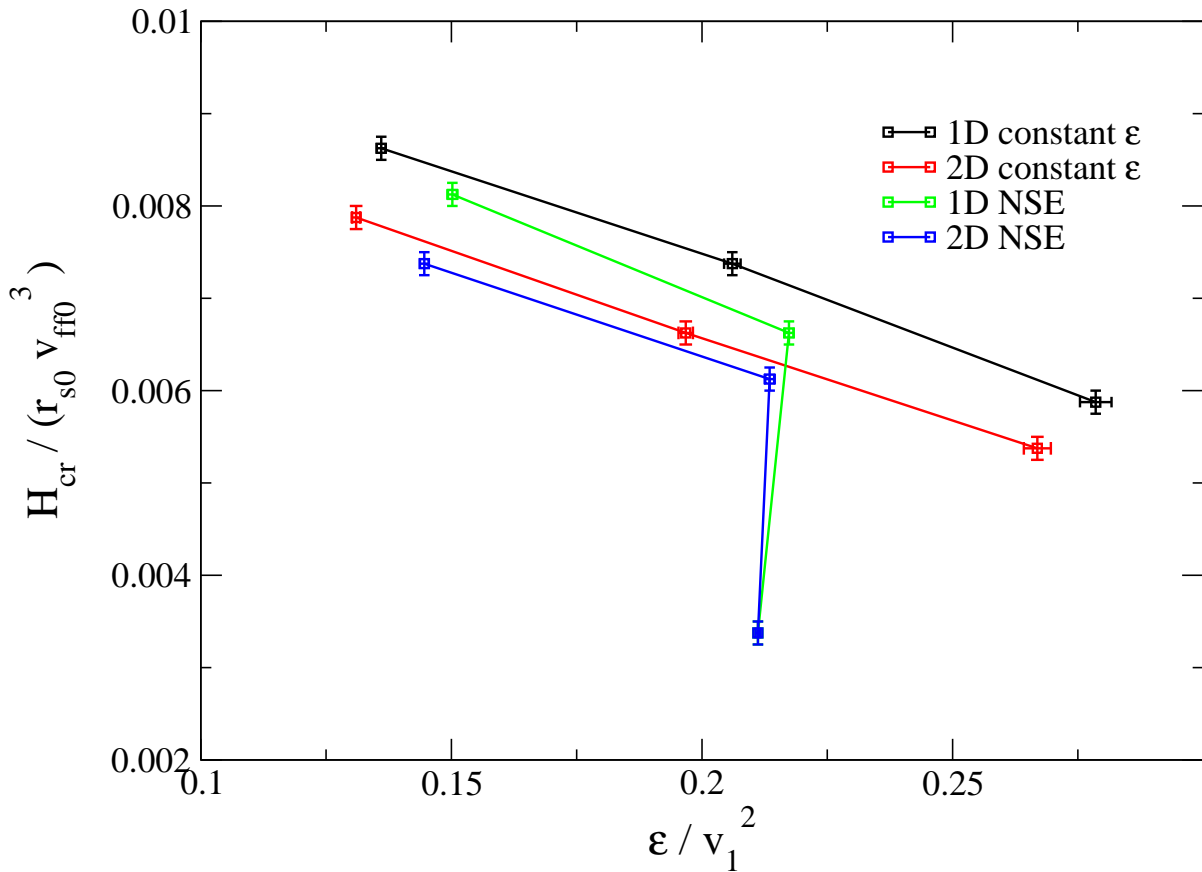


Figure 6.10: Critical heating parameter H_{cr} that yields an explosion, for all the model sequences explored in this paper (Table 2.2). The abscissa is the ratio of ϵ to v_1^2 in the initial flow configuration (v_1 being the radial flow velocity just upstream of the shock). Error bars show the separation between exploding and non-exploding models, with the points marking the average.

through a series of transient fluid motions.

Second, H_{cr} is lower when NSE between n , p and α is maintained below the shock. The difference between the NSE models and the constant- ε models is only $\sim 10\%$ in H_{cr} when the shock starts out well below r_α (eq. [2.1]). In spherical symmetry, this effect can be ascribed to the slow decline of ε with increasing shock radius: this makes it easier for the shock to expand through the range of radii where $\varepsilon/v_{\text{ff}0}^2$ approaches $\frac{1}{2}$. An explosion is significantly easier when the fluid below the shock starts out with a significant population of α particles, as in the models with $r_{\text{s}0} = 125$ km (note that ε/v_1^2 decreases at large radius in the NSE model, see Figure 2.1).

Third, H_{cr} tends to decrease with increasing ε/v_1^2 : a slightly *lower* heating rate per unit mass is required to explode a flow with a *larger* density contrast κ across the shock. Because almost all the gravitating mass is in the collapsed core, the gravitational binding energy of the gain region is approximately proportional to κ , whereas the net heat absorbed over the advection time is a stronger function of density, $t_{\text{adv}} \int (\mathcal{L}_H - \mathcal{L}_C) d^3r \propto \kappa^2$. (One factor of κ comes from the advection time t_{adv} as given by eq. [3.3], and the other from the density dependence of \mathcal{L}_H .) For example, Table 2.2 shows that κ is ~ 1.6 times larger for $\varepsilon/v_{\text{ff}0}^2 = 0.2$ than for $\varepsilon/v_{\text{ff}0}^2 = 0.1$, and that H_{cr} is smaller by the inverse of the same factor.

Fourth, the 2D runs all require less heating than their 1D counterparts to explode. A major reason for this is that all two-dimensional configurations explode along one or both poles (see Figs. 6.6 and 5.3), so that less material must be lifted through the gravitational field than in a fully spherical explosion. We have found that the precise value of the difference between the critical heating rate in the 1D and 2D explosions depends on the choice of $r_*/r_{\text{s}0}$, and therefore on the normalization C of the cooling function. The fact that we find a smaller difference than Murphy & Burrows (2008) may be a consequence of our simpler cooling function and equation of state.

The critical heating rate depends in an interesting way on the starting radius of the

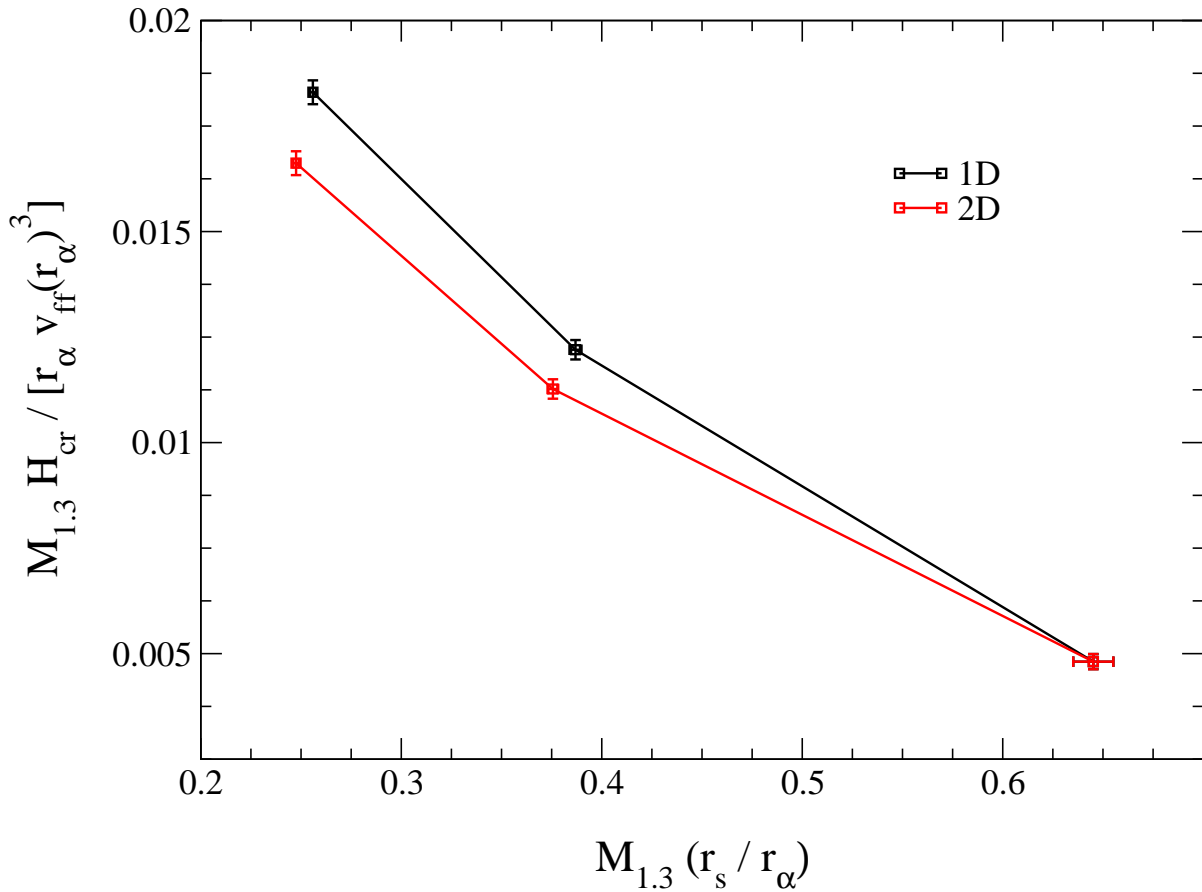


Figure 6.11: Critical heating parameter H_{cr} that yields an explosion, for the runs that include α -particles in the EOS. The abscissa is the ratio of the initial shock radius r_s to r_{α} . Error bars have the same meaning as in Fig. 6.10. The critical heating parameter (a close analog of L_{ν}) decreases substantially with increasing shock radius. The differences in H_{cr} between the 1D and 2D models also decreases.

shock, in a way that points to the recombination of α -particles as an important last step in the transition to an explosion. Figure 6.11 shows that H_{cr} in the NSE models grows rapidly as the initial shock radius² r_s is pushed inside r_α . Here we normalize the heating parameter at a fixed *physical* radius, namely r_α . Translated into the context of a realistic core collapse, this means that the critical neutrino luminosity for an explosion decreases with increasing shock radius. The radius of the stalled shock depends, in turn, on the EOS above nuclear matter density: Marek & Janka (2009) find that a softer EOS corresponds to a larger shock radius, mainly due to the higher accretion luminosity onto the neutronized core. Here we have subsumed this uncertainty in the high-density EOS into a single free parameter, the ratio r_{s0}/r_α . Hydrodynamic instabilities are effective at driving an explosion to the extent that they push the shock radius close to r_α ; beyond this point, the remainder of the work on the flow is done largely by α -particle recombination.

One also notices from Fig. 6.11 that the difference between H_{cr} in 1D and 2D depends on the starting radius of the shock. The closer r_{s0} is to r_α , the weaker the dependence of the critical heating rate on the dimensionality of the flow.

6.5 Summary

In this chapter we have explored the quantitative effect that the energy released by alpha-particle recombination has on an accretion shock system close to the threshold for an explosion. We have focused on the nature of shock breakout on one- and two-dimensional systems, the relative importance of neutrino and recombination heating, their spatial distribution, and their effect on the critical heating rate for an explosion. Our main results can be summarized as follows:

1. – The critical heating parameter that yields an explosion depends sensitively on the

²Note that r_s is the shock radius in the time-independent flow solution. For a fixed cooling function, r_s is a monotonically increasing function of H , and equals r_{s0} at $H = 0$.

starting position of the shock relative to r_α . This means that the critical neutrino luminosity depends sensitively on the stall radius of the shock and, in turn, on the core structure of the progenitor star and the density profile in the forming neutron star. Within the framework explored in this paper, we find two extreme types of explosion. In the first, neutrino heating does most of the work, with a significant final boost from α -particle recombination. In the second, neutrino heating is generally less important at promoting material below the shock to positive energies.

2. – During the final stages of an explosion, the heat released by α -particle recombination is comparable to the work done by adiabatic expansion. This heat is concentrated in material that has previously been heated by neutrinos. Significantly more energy is lost through α -particle dissociation in fresh downflows, so that nuclear dissociation remains on balance an energy sink within the accretion flow.

3. – The critical heating parameter H_{cr} for an explosion is generally lower in 2D than in 1D, but the difference becomes smaller as the starting radius of the shock approaches r_α . The precise value of the difference is dependent on the ratio r_*/r_{s0} and thus on the cooling efficiency and equation of state.

4. – We have explored essentially one ratio of cooling radius to shock radius, namely $r_*/r_{s0} = 0.4$ at zero heating (corresponding to $r_*/r_s \sim 0.2$ near the threshold for an explosion). The growth of the $\ell = 1$ SASI mode is strongest for this particular aspect ratio when $\varepsilon = 0$ (see Figure 12 of Paper I). As dissociation is introduced into the flow, we found that the peak growth rate moves to larger values of r_*/r_{s0} . On the other hand, detailed collapse calculations indicate ratios of neutrinosphere radius to shock radius that are even smaller than ~ 0.2 following ~ 100 ms after collapse (e.g. Marek & Janka 2009). We conclude that the $l = 1$ SASI mode is not being artificially suppressed by our choice

of initial shock size.

Chapter 7

Conclusions

In this thesis, we have investigated the stability and dynamics of a spherical accretion shock in the context of core-collapse supernovae. We have done so by constructing a simplified model of the system that incorporates the relevant physical processes in steps of increasing complexity. Our main goal has been to understand nonlinear phenomena involving multidimensional hydrodynamic instabilities from a fundamental point of view.

We have focused on the intrinsic stability of the accretion flow, in the absence of neutrino-driven convection, when nuclear dissociation is allowed to take place below the shock. We then added neutrino heating gradually, and studied the competition between the overstable mode and convective motions driven by a negative entropy gradient in the region where heating dominates cooling. Later, we increased the heating rate until an explosion was uncovered, and studied the dynamics in 1D and 2D, focusing on understanding the differences introduced by dimensionality. Finally, we assessed the effects of α -particle recombination on the dynamics and critical heating rate for explosion.

We found that nuclear dissociation at realistic levels significantly damps the standing accretion shock instability (SASI), both in its linear phase and when fully saturated, with similar effects being obtained when reducing the adiabatic index of the flow. We have also found that the maximum growth rates of these modes are attained when the

radial advection time below the shock is comparable to the lateral sound crossing time, with the radial cycle determining the mode overtone and the lateral period the angular degree. Regarding the interplay with convection, we agree with previous investigations in that there is a critical heating rate below which convection is quenched by the accretion flow and the SASI dominates. At the threshold for a neutrino-driven explosion, we find that all of our simulations are above this critical point where convection dominates the dynamics. Indeed, the maximal amplitude of dipolar shock motions is found when the oscillation period is comparable to the convective period.

In spite of the simplifications introduced in our model, the calculations already show many similarities with more elaborate collapse calculations. One-dimensional explosions are due to a global instability resembling the spherically symmetric version of the SASI, modified by heating. Strong deformations of the shock in 2D are driven by material with positive Bernoulli parameter, which generally resides outside the radius r_α where the gravitational binding energy of an α -particle is equal to its nuclear binding energy. The recombination of α -particles plays a major role in creating this positive-energy material, but for this to happen the shock must be pushed beyond ~ 200 km from the neutronized core.

In this investigation, we have considered only neutrino heating as the impetus for the initial expansion of the shock, rather than more exotic effects such as rotation or magnetic fields. We found that the critical neutrino luminosity for an explosion is a steep function of the position of the shock relative to the radius r_α . Significant EOS uncertainties remain at supranuclear densities. A softening or hardening of the EOS feeds back on the position of the shock for a given pre-collapse stellar model (Marek & Janka, 2009). Variations in the density profile of the progenitor star will similarly modify the position of the shock, the concentration of α -particles below it, and therefore the critical neutrino luminosity for an explosion.

There are at least two reasons why explosions by the mechanism investigated here

may be more difficult in 3D than in 2D. First, the existence of more degrees of freedom for the low-order modes of the shock in 3D implies that the amplitude of individual shock oscillations is lower (see, e.g., the results of Iwakami et al. 2008). As a result, it is more difficult for the shock to extend out to the radius where α -particle recombination gives it the final push. Second, an explosion that is driven by neutrino heating in 2D involves the accumulation of vorticity on the largest spatial scales, an effect that is special to two dimensions. A full resolution of these issues is possible only with high-resolution 3D simulations.

Our model for the shocked material retains one significant simplification: we do not allow the electron fraction Y_e to vary with position below the accretion shock. Here there are two competing effects: electron captures tend to reduce Y_e , whereas absorption of ν_e and $\bar{\nu}_e$ tends to drive high-entropy material below the shock toward $Y_e \simeq 0.5$. Since we are interested especially in the dynamics of this high-entropy material, we have set $Y_e = 0.5$ throughout the flow. The consequences of introducing these additional degrees of freedom in the equation of state will be examined in future work.

We conclude by emphasizing that significant insight can be gained by performing carefully constructed numerical experiments in a situation where the real problem is very complicated. Separating out, and gradually adding different physical ingredients in a nonlinear context allows the identification of the relative importance of each effect on the total outcome, when all the pieces are put in place. In this way, the understanding of natural phenomena in terms of fundamental physical principles is better advanced.

Appendix A

Alpha-Particle Abundance in Nuclear Statistical Equilibrium

We calculate the α -particle mass fraction X_α in nuclear statistical equilibrium by limiting the nuclear species to α -particles and free nucleons, and fixing the electron fraction $Y_e = 0.5$. We tabulate X_α and temperature T as a function of pressure p and density ρ , and then use these tables to calculate the rate of release of nuclear binding energy by the method described in §2.2.1. The temperature does not appear explicitly in the FLASH hydrodynamic solver, and only enters the flow equations indirectly through X_α .

We include the contributions to p from radiation, relativistic and partially degenerate electron-positron pairs, and nonrelativistic α -particles and nucleons. When $k_B T > m_e c^2/2$, it can be written (Bethe et al., 1980):

$$p = \frac{1}{12} \frac{(k_B T)^4}{(\hbar c)^3} \left[\frac{11\pi^2}{15} + 2\eta^2 + \frac{1}{\pi^2} \eta^4 \right] + \left(1 - \frac{3}{4} X_\alpha \right) \frac{\rho}{m_u} k_B T, \quad (\text{A.1})$$

where $\eta = \mu_e/(k_B T)$ the normalized electron chemical potential, also known as degeneracy parameter, and \hbar , c , and m_u are Planck's constant, the speed of light, and the atomic mass unit, respectively. The density and degeneracy parameter are further related by

$$\rho = \frac{m_u}{3\pi^2 Y_e} \left(\frac{k_B T}{\hbar c} \right)^3 \eta(\pi^2 + \eta^2), \quad (\text{A.2})$$

where Y_e is the electron fraction. The equilibrium fraction of α -particles is given by the nuclear Saha equation,

$$X_n^2 X_p^2 = \frac{1}{2} X_\alpha \left[\frac{m_u n_Q(T)}{\rho} \right]^3 \exp\left(-\frac{Q_\alpha}{k_B T}\right); \quad n_Q(T) = \left(\frac{m_u k_B T}{2\pi\hbar^2} \right)^{3/2} \quad (\text{A.3})$$

as supplemented by the conditions of mass and charge conservation,

$$X_n + X_p + X_\alpha = 1 \quad (\text{A.4})$$

$$X_p + \frac{1}{2} X_\alpha = Y_e. \quad (\text{A.5})$$

In eqs. (A.3)-(A.5), X_n and X_p are the mass fractions of free neutrons and protons, respectively, and $Q_\alpha = 28.3$ MeV is the binding energy of an α -particle. Combining eqs. (A.1) and (A.2) gives η and T in terms of p and ρ . The equilibrium mass fraction X_α^{eq} is calculated from ρ and T . For numerical calculations, we tabulate X_α^{eq} , $\partial X_\alpha^{\text{eq}}/\partial \ln \rho$, and $\partial X_\alpha^{\text{eq}}/\partial \ln p$ for a grid of density and pressure. In addition, we tabulate partial derivatives of T to substitute in eqs. (B.10) and (B.11).

Figure A.1 shows contours of constant X_α^{eq} and constant entropy for different variables as a function of density. The entropy per nucleon is obtained by adding the contributions from the different components (e.g. Bethe et al. 1980),

$$S = \pi^2 Y_e \frac{(11\pi^2/15 + \eta^2)}{\eta(\pi^2 + \eta^2)} + \left(1 - \frac{3}{4} X_\alpha\right) \left[\frac{5}{2} + \ln \left\{ \frac{m_u n_Q(T)}{\rho} \right\} \right] - X_p \ln X_p - X_n \ln X_n - \frac{1}{4} X_\alpha \ln (X_\alpha/32). \quad (\text{A.6})$$

The postshock density in the initial configuration is typically $\rho_2 \sim 10^9$ g cm⁻³ with an entropy $\sim 10 - 15 k_B$ /nucleon. The formation of α -particles that is seen in Fig. 2.1 results from an expansion of the shock into the part of the thermodynamic plane in Figs. A.1a,b where $\rho_2 < 10^9$ g cm⁻³ and $T \lesssim 1$ MeV. In this regime, the electrons are non-degenerate and the pressure in photons and pairs begins to exceed the nucleon pressure. The dip in the adiabatic index seen in Fig. A.1f results from α -particle dissociation/recombination, which partially compensates the change in internal energy due to compression/expansion.

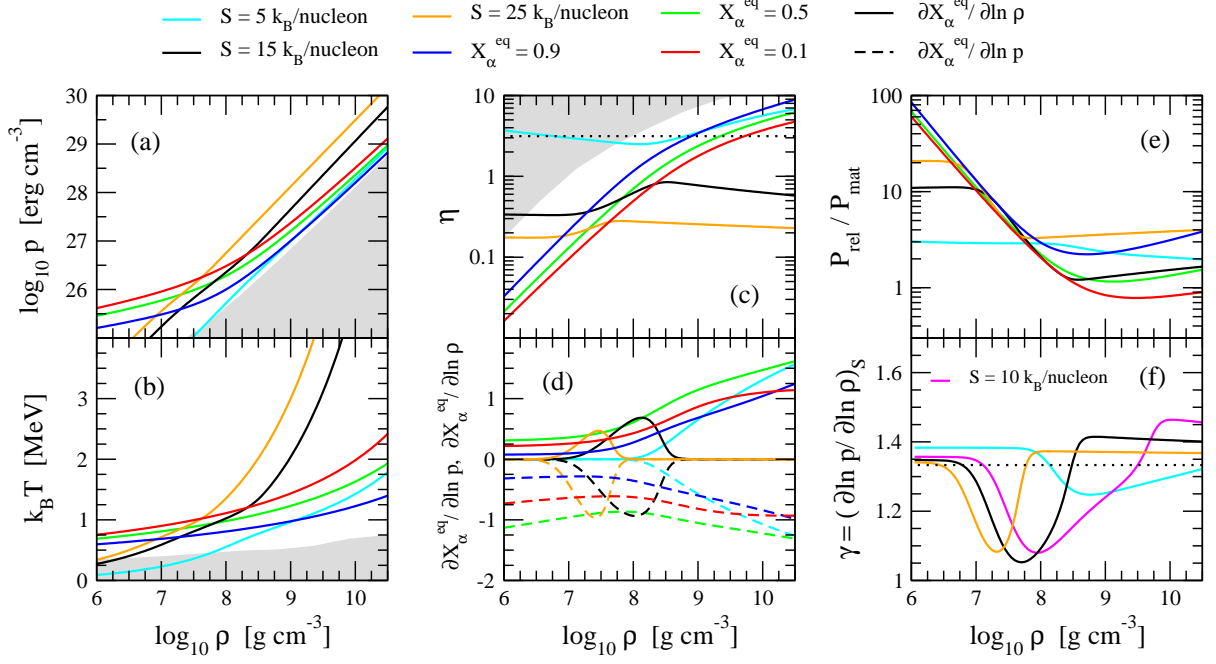


Figure A.1: Equation of state of a fluid containing n , p , α , photons, and finite-temperature and partially degenerate electrons, in nuclear statistical equilibrium. We solve eqns. (A.1)-(A.5) and tabulate all quantities on a grid of density and pressure. Panels (a), (b) and (c): pressure, temperature, and degeneracy parameter as a function of density, for fixed values of X_α^{eq} and entropy. Dotted line: $\eta = \pi$, the approximate boundary between degenerate and non-degenerate electrons. The gray area shows the region of the thermodynamic plane where $X_{\text{O}}^{\text{eq}} = 0.5$. Panel (d): partial derivatives of X_α^{eq} with respect to density (solid lines, positive) and pressure (dashed lines, negative). Panel (e): ratio of relativistic pressure (photons and pairs) to material pressure (α -particles and nucleons). Panel (f): adiabatic index γ for different adiabats (dotted line: $\gamma = 4/3$).

Appendix B

Time-Independent Flow Equations Describing Initial Models

We write down the ordinary differential equations that are used to compute the initial flow, and the density profiles in Fig. 2.3a,b,c. The steady state Euler equations in spherical symmetry are

$$\frac{1}{v_r} \frac{dv_r}{dr} + \frac{1}{\rho} \frac{d\rho}{dr} + \frac{2}{r} = 0 \quad (\text{B.1})$$

$$v_r \frac{dv_r}{dr} + \frac{1}{\rho} \frac{dp}{dr} + g = 0 \quad (\text{B.2})$$

$$\rho v_r \frac{de_{\text{int}}}{dr} - \frac{pv_r}{\rho} \frac{d\rho}{dr} = \mathcal{L}_H - \mathcal{L}_C + \mathcal{L}_\alpha, \quad (\text{B.3})$$

where e_{int} is the internal energy per unit mass, \mathcal{L}_H , \mathcal{L}_C , and \mathcal{L}_α the source terms described in eqns. (2.5)-(2.7), and $g = GM/r^2$. Since two variables suffice to describe the thermodynamic state of a system, we write

$$\frac{de_{\text{int}}}{dr} \equiv E_p \frac{dp}{dr} + E_\rho \frac{d\rho}{dr}. \quad (\text{B.4})$$

and

$$\mathcal{L}_\alpha \equiv A_p \frac{dp}{dr} + A_\rho \frac{d\rho}{dr}. \quad (\text{B.5})$$

The coefficients E_i and A_i encode the dependence on the equation of state. Replacing eqns. (B.4) and (B.5) in (B.3), and using eqns. (B.1) and (B.2) to eliminate the pressure derivative, we obtain

$$\frac{d\rho}{dr} = \frac{(\rho v_r E_p - A_p)(\rho g - 2\rho v_r^2/r) + (\mathcal{L}_H - \mathcal{L}_C)}{(\rho v_r E_\rho - p v_r/\rho - A_\rho) + v_r^2(\rho v_r E_p - A_p)}. \quad (\text{B.6})$$

The coefficients in eqs. (B.4) and (B.5) work out to

$$E_p = \frac{1}{(\gamma - 1)\rho} \quad (\text{constant } \gamma) \quad (\text{B.7})$$

$$E_\rho = -\frac{p}{(\gamma - 1)\rho^2} \quad (\text{constant } \gamma). \quad (\text{B.8})$$

for a constant- γ equation of state, $e_{\text{int}} = p/[(\gamma - 1)\rho]$. The pressure (eq. [A.1]) in the NSE model described in Appendix A can be decomposed into contributions from relativistic particles and from nucleons, $p = p_{\text{rel}} + p_{\text{mat}}$, and the specific internal energy is

$$e_{\text{int}} = \frac{1}{\rho} \left(3p_{\text{rel}} + \frac{3}{2}p_{\text{mat}} \right) = 3\frac{p}{\rho} - \frac{3}{2} \left(1 - \frac{3}{4}X_\alpha \right) \frac{k_B T}{m_u}. \quad (\text{B.9})$$

One therefore finds

$$E_p = \frac{3}{\rho} + \frac{9}{8} \frac{k_B T}{m_u} \frac{\partial X_\alpha}{\partial p} - \frac{3}{2} \left(1 - \frac{3}{4}X_\alpha \right) \frac{1}{m_u} \frac{\partial(k_B T)}{\partial p}, \quad (\text{NSE}) \quad (\text{B.10})$$

$$E_\rho = -\frac{3p}{\rho^2} + \frac{9}{8} \frac{k_B T}{m_u} \frac{\partial X_\alpha}{\partial \rho} - \frac{3}{2} \left(1 - \frac{3}{4}X_\alpha \right) \frac{1}{m_u} \frac{\partial(k_B T)}{\partial \rho}. \quad (\text{NSE}) \quad (\text{B.11})$$

The initial postshock solution is obtained by integrating the above equations from r_s to an inner radius r_* at which the flow stagnates. We iterate the normalization of the cooling function in eq. (2.5) so that $r_* = 0.4r_{s0}$ in the absence of heating. When adding heating, the cooling normalization and r_* are kept fixed, which results in an expansion of the shock from its initial position to $r_s > r_{s0}$ (Fig. 2.3a,b).

When including α -particles in the EOS, one needs to calculate self-consistently the value of X_α^{eq} below the shock, the corresponding dissociation energy $\varepsilon(t = 0)$ [eq. (2.11)], and compression factor κ [eq. (2.10)]. The density upstream of the shock is obtained from

$$\rho_1(r_s) = \frac{\dot{M}}{4\pi r_s^2 |v_1(r_s)|}, \quad (\text{B.12})$$

where

$$v_1(r_s) = -\frac{v_{\text{ff}}(r_s)}{\sqrt{1 + 2\mathcal{M}_1^{-2}(r_s)/(\gamma - 1)}} \quad (\text{B.13})$$

is the upstream velocity at $r = r_s$, while the upstream pressure satisfies

$$p_1(r_s) = \frac{\rho_1(r_s)[v_1(r_s)]^2}{\gamma\mathcal{M}_1^2(r_s)}. \quad (\text{B.14})$$

Eqns. (B.12) and (B.14) are transformed to physical units for input to the NSE model by adopting $\mathcal{M}_1(r_{s0}) = 5$, $\dot{M} = 0.3 M_\odot \text{ s}^{-1}$, $M = 1.3 M_\odot$, and a particular value for the shock radius r_{s0} in the absence of heating.

Appendix C

Numerical Treatment of Nuclear Burning in FLASH2.5

Nuclear dissociation is implemented by means of the *fuel+ash* nuclear burning module in FLASH2.5 (Fryxell et al., 2000). To prevent undesired dissociation effects upstream of the shock, we replace the density and temperature thresholds for burning in the default version of the code with a threshold in Mach number: burning takes place so long as the fluid has a Mach number lower than $\mathcal{M}_{\text{burn}} = 2$. This results in a small amount of incomplete burning in the presence of strong shock deformations, a phenomenon which is also encountered in the full collapse problem. The critical heating parameter H_{cr} depends weakly on $\mathcal{M}_{\text{burn}}$: changes in $\mathcal{M}_{\text{burn}}$ cause small changes in the amount of unburnt material with zero Bernoulli parameter, and only slightly alters the net energy of the gain region. At the outer boundary of the simulation volume, $\mathcal{M}_{\text{burn}}$ is just below the Mach number of the upstream flow. We have tried expanding the outer boundary to $r = 9r_{\text{s}0}$ (with a somewhat smaller $\mathcal{M}_{\text{burn}}$) and found that runs that did hit $r = 7r_{\text{s}0}$ still hit the new outer boundary.

For constant ε models, the threshold in Mach number has the effect of localizing the nuclear dissociation right behind the shock. In principle all of the kinetic energy of

accretion can be absorbed by nuclear dissociation downstream of a shock: the Riemann problem has a limiting solution $\rho_2 \rightarrow \infty$ and $v_2 \rightarrow 0$, with $\rho_2 v_2 = \rho_1 v_1$, which for a strong shock yields $\varepsilon \rightarrow v_1^2/2$. However, the numerical evolution of the problem in discrete timesteps limits the dissociation energy to be smaller in magnitude than the specific internal energy of the fluid, otherwise negative pressure results. In particular, since we want to maintain a steady shock as background flow for shock stability calculations, the maximum dissociation energy that can be removed in a single timestep at $r = r_{s0}$ is the internal energy of the postshock flow after dissociation has been subtracted. That is, if we allow for the density contrast κ to increase according to eq. (2.10), then we require

$$\varepsilon < \frac{v_1^2}{\gamma(\gamma - 1)\mathcal{M}_2^2\kappa^2}, \quad (\text{C.1})$$

where \mathcal{M}_2 is the post-shock Mach number, eq. (3.1). The maximum single-step dissociation energy ε_{max} is obtained by equating the two sides of eq. (C.1). One finds $\varepsilon_{\text{max}} \simeq 0.213v_{\text{ff}}^2$ for $\gamma = 4/3$ and $\mathcal{M}_1 \rightarrow \infty$.

In reality, burning of the shocked fluid occurs within a layer of a finite width. To relax the above limit on ε , we have modified the default *fuel+ash* submodule of FLASH2.5 to allow nuclear dissociation to occur in stages: instead of burning all the *fuel* into *ash* in a single step, we only allow the burning of a fraction $1/n_{\text{burn}}$ at a time. The value of n_{burn} is adjusted empirically so as to avoid numerical problems at large expansions of the shock, where ε may approach the local value¹ of $v_{\text{ff}}^2/2$. In most cases, the burning is spread across $\sim n_{\text{burn}}$ cells behind the shock. We have checked that the mode frequencies of the flow are insensitive to the particular choice, as long as the single-step constraint is met.

In the NSE nuclear dissociation model, burning takes place in a more extended region behind the shock. In this case, the numerical stability of the flow is maintained using an

¹As we discuss in § 4, the shock oscillations saturate at a low amplitude when $\varepsilon > 0.15v_{\text{ff}}^2$, which means that this effect is negligible for the simulations reported in this paper.

implicit update of the pressure in between hydro sweeps,

$$p_{\text{new}} = p_{\text{cur}} + (\gamma - 1)\rho e_{\text{nuc}}(\rho, p_{\text{new}}), \quad (\text{C.2})$$

where e_{nuc} is the energy generation per timestep in equation (2.14), and the subscripts *cur* and *new* refer to the current and new value of the pressure, respectively. The density is kept constant across this step, so as to be consistent with the other source terms. Equation (C.2) usually converges in 3-4 Newton iterations, adding a negligible overhead to our execution time. We restrict the timestep of the simulation so that, in addition to the standard Courant-Friedrichs-Levy condition, it enforces $|e_{\text{nuc}}| < 0.8(p/\rho)/(\gamma - 1)$. To prevent α -particle recombination in the cooling layer (due to the decrease of internal energy), we adopt a cutoff in density, so that $X_{\alpha} = 0$ if $\rho > 3 \times 10^{10} \text{g cm}^{-3}$.

Bibliography

Akiyama, S., Wheeler, J. C., Meier, D. L., & Lichtenstadt, I. 2003, *ApJ*, 584, 954

Arnett, W. D. 1967, *Canadian Journal of Physics*, 45, 1621

Arnett, W. D., Bahcall, J. N., Kirshner, R. P., & Woosley, S. E. 1989, *ARA&A*, 27, 629

Audi, G., Wapstra, A. H., & Thibault, C. 2003, *Nuclear Physics A*, 729, 337

Baade, W., & Zwicky, F. 1934a, *Proceedings of the National Academy of Science*, 20, 259

—. 1934b, *Proceedings of the National Academy of Science*, 20, 254

Bethe, H. A. 1990, *Reviews of Modern Physics*, 62, 801

—. 1993, *ApJ*, 412, 192

—. 1996, *ApJ*, 469, 737

—. 1997, *ApJ*, 490, 765

Bethe, H. A., Applegate, J. H., & Brown, G. E. 1980, *ApJ*, 241, 343

Bethe, H. A., Brown, G. E., Applegate, J. H., & Lattimer, J. M. 1979, *Nuclear Physics A*, 324, 487

Bethe, H. A., & Wilson, J. R. 1985, *ApJ*, 295, 14

- Blandford, R., & Eichler, D. 1987, *Phys. Rep.*, 154, 1
- Blondin, J. M., & Mezzacappa, A. 2006, *ApJ*, 642, 401
- . 2007, *Nature*, 445, 58
- Blondin, J. M., Mezzacappa, A., & DeMarino, C. 2003, *ApJ*, 584, 971
- Blondin, J. M., & Shaw, S. 2007, *ApJ*, 656, 366
- Bodenheimer, P., & Woosley, S. E. 1983, *ApJ*, 269, 281
- Bond, J. R., Arnett, W. D., & Carr, B. J. 1984, *ApJ*, 280, 825
- Bowers, R., & Wilson, J. R. 1982, *ApJ*, 263, 366
- Brown, G. E., Bethe, H. A., & Baym, G. 1982, *Nuclear Physics A*, 375, 481
- Bruenn, S. W., Raley, E. A., & Mezzacappa, A. 2004, *ArXiv Astrophysics e-prints*
- Buras, R., Janka, H.-T., Rampp, M., & Kifonidis, K. 2006a, *A&A*, 457, 281
- Buras, R., Rampp, M., Janka, H.-T., & Kifonidis, K. 2006b, *A&A*, 447, 1049
- Burbidge, E. M., Burbidge, G. R., Fowler, W. A., & Hoyle, F. 1957, *Reviews of Modern Physics*, 29, 547
- Burrows, A. 1987, *ApJ*, 318, L57
- Burrows, A., Dessart, L., Livne, E., Ott, C. D., & Murphy, J. 2007a, *ApJ*, 664, 416
- Burrows, A., & Goshy, J. 1993, *ApJ*, 416, L75
- Burrows, A., Hayes, J., & Fryxell, B. A. 1995, *ApJ*, 450, 830
- Burrows, A., Livne, E., Dessart, L., Ott, C. D., & Murphy, J. 2006, *ApJ*, 640, 878
- . 2007b, *ApJ*, 655, 416

- Burrows, A., Mazurek, T. J., & Lattimer, J. M. 1981, *ApJ*, 251, 325
- Calder, A. C., Fryxell, B., Plewa, T., Rosner, R., Dursi, L. J., Weirs, V. G., Dupont, T., Robey, H. F., Kane, J. O., Remington, B. A., Drake, R. P., Dimonte, G., Zingale, M., Timmes, F. X., Olson, K., Ricker, P., MacNeice, P., & Tufo, H. M. 2002, *ApJS*, 143, 201
- Cappellaro, E., Evans, R., & Turatto, M. 1999, *A&A*, 351, 459
- Colella, P., & Woodward, P. R. 1984, *Journal of Computational Physics*, 54, 174
- Colgate, S. A. 2004, in *Stellar Collapse*, ed. C. Fryer (Dordrecht: Kluwer), xxv
- Colgate, S. A., & Johnson, M. H. 1960, *Physical Review Letters*, 5, 235
- Colgate, S. A., & White, R. H. 1966, *ApJ*, 143, 626
- Cowling, T. G. 1933, *MNRAS*, 94, 39
- Davidson, P. A. 2004, *Turbulence: an introduction for scientists and engineers*, 1st edn. (Oxford: Oxford University Press)
- DeLaney, T., Smith, J. D., Rudnick, L., Stage, M. D., Isensee, K., Rho, J., Reach, W. T., Ennis, J. A., Kozasa, T., Gomez, H., Allen, G. E., Davis, J. E., & Houck, J. C. 2009, in *Bulletin of the American Astronomical Society*, Vol. 41, *Bulletin of the American Astronomical Society*, 377
- Dessart, L., Burrows, A., Livne, E., & Ott, C. D. 2006, *ApJ*, 645, 534
- . 2007, *ApJ*, 669, 585
- Epstein, R. I. 1979, *MNRAS*, 188, 305
- Fernández, R., & Thompson, C. 2009a, *ApJ*, in press, astro-ph/0812.4574
- . 2009b, *ApJ*, 697, 1827

- Foglizzo, T., Galletti, P., Scheck, L., & Janka, H.-T. 2007, *ApJ*, 654, 1006
- Foglizzo, T., Scheck, L., & Janka, H.-T. 2006, *ApJ*, 652, 1436
- Foglizzo, T., & Tagger, M. 2000, *A&A*, 363, 174
- Fowler, W. A., & Hoyle, F. 1964, *ApJS*, 9, 201
- Freedman, D. Z. 1974, *PrD*, 9, 1389
- Fryer, C. L., Rockefeller, G., & Warren, M. S. 2006, *ApJ*, 643, 292
- Fryer, C. L., & Young, P. A. 2007, *ApJ*, 659, 1438
- Fryxell, B., Olson, K., Ricker, P., Timmes, F. X., Zingale, M., Lamb, D. Q., MacNeice, P., Rosner, R., Truran, J. W., & Tufo, H. 2000, *ApJS*, 131, 273
- Gallagher, J. S., & Starrfield, S. 1978, *ARA&A*, 16, 171
- Goldreich, P., & Kumar, P. 1988, *ApJ*, 326, 462
- Goldreich, P., & Weber, S. V. 1980, *ApJ*, 238, 991
- Hamuy, M. 2004, in *Stellar Collapse*, ed. C. Fryer (Dordrecht: Kluwer), 39–64
- Harding, A. K., & Lai, D. 2006, *Reports on Progress in Physics*, 69, 2631
- Heger, A., Woosley, S. E., & Spruit, H. C. 2005, *ApJ*, 626, 350
- Herant, M., Benz, W., & Colgate, S. 1992, *ApJ*, 395, 642
- Herant, M., Benz, W., Hix, W. R., Fryer, C. L., & Colgate, S. A. 1994, *ApJ*, 435, 339
- Hillebrandt, W., & Niemeyer, J. C. 2000, *ARA&A*, 38, 191
- Houck, J. C., & Chevalier, R. A. 1992, *ApJ*, 395, 592
- Iwakami, W., Kotake, K., Ohnishi, N., Yamada, S., & Sawada, K. 2008, *ApJ*, 678, 1207

Janka, H.-T. 2001, *A&A*, 368, 527

Janka, H.-T., & Mueller, E. 1996, *A&A*, 306, 167

Janka, H.-T., Müller, B., Kitaura, F. S., & Buras, R. 2008, *A&A*, 485, 199

Kifonidis, K., Plewa, T., Scheck, L., Janka, H.-T., & Müller, E. 2006, *A&A*, 453, 661

Kippenhahn, R., & Weigert, A. 1994, *Stellar Structure and Evolution*, 1st edn. (Berlin: Springer)

Kitaura, F. S., Janka, H.-T., & Hillebrandt, W. 2006, *A&A*, 450, 345

Kulsrud, R. M. 2005, *Plasma Physics for Astrophysics*, 1st edn. (Princeton: Princeton Univ. Press)

Lai, D., & Goldreich, P. 2000, *ApJ*, 535, 402

Laming, J. M. 2007, *ApJ*, 659, 1449

Landau, L. D., & Lifshitz, E. M. 1987, *Fluid Mechanics*, 2nd edn. (Oxford: Butterworth-Heinemann)

Lattimer, J. M., & Prakash, M. 2007, *Phys. Rep.*, 442, 109

Lattimer, J. M., & Swesty, D. F. 1991, *Nuclear Physics A*, 535, 331

LeBlanc, J. M., & Wilson, J. R. 1970, *ApJ*, 161, 541

Leveque, R. J. 1998, in *Saas-Fee Advanced Course 27: Computational Methods for Astrophysical Fluid Flow.*, ed. O. Steiner & A. Gaultschy, 1

Liebendörfer, M., Mezzacappa, A., Thielemann, F.-K., Messer, O. E., Hix, W. R., & Bruenn, S. W. 2001, *PRD*, 63, 103004

MacFadyen, A. I., & Woosley, S. E. 1999, *ApJ*, 524, 262

- Marek, A., & Janka, H.-T. 2009, *ApJ*, 694, 664
- Mezzacappa, A., Calder, A. C., Bruenn, S. W., Blondin, J. M., Guidry, M. W., Strayer, M. R., & Umar, A. S. 1998, *ApJ*, 495, 911
- Miller, D. S., Wilson, J. R., & Mayle, R. W. 1993, *ApJ*, 415, 278
- Miyaji, S., Nomoto, K., Yokoi, K., & Sugimoto, D. 1980, *PASJ*, 32, 303
- Murdin, P., & Murdin, L. 1985, *Supernovae*, 2nd edn. (Cambridge: Cambridge Univ. Press)
- Murphy, J. W., & Burrows, A. 2008, *ArXiv e-prints*
- Nagano, M., & Watson, A. A. 2000, *Reviews of Modern Physics*, 72, 689
- Ohnishi, N., Kotake, K., & Yamada, S. 2006, *ApJ*, 641, 1018
- Ott, C. D., Burrows, A., Dessart, L., & Livne, E. 2008, *ApJ*, 685, 1069
- Ott, C. D., Burrows, A., Thompson, T. A., Livne, E., & Walder, R. 2006, *ApJS*, 164, 130
- Porter, D. H., & Woodward, P. R. 1994, *ApJS*, 93, 309
- Press, W. H., Teukolski, S. A., Vetterling, W. T., & Flannery, B. P. 2006, *Numerical Recipes in Fortran 77*, 2nd edn. (Cambridge: Cambridge University Press)
- Quirk, J. J. 1994, *Int. Jour. Num. Meth. Fluids*, 18, 555
- Rampp, M., & Janka, H.-T. 2002, *A&A*, 396, 361
- Sagert, I., Fischer, T., Hempel, M., Pagliara, G., Schaffner-Bielich, J., Mezzacappa, A., Thielemann, F.-K., & Liebendörfer, M. 2009, *Physical Review Letters*, 102, 081101
- Scheck, L., Janka, H.-T., Foglizzo, T., & Kifonidis, K. 2008, *A&A*, 477, 931

- Scheck, L., Kifonidis, K., Janka, H.-T., & Müller, E. 2006, *A&A*, 457, 963
- Shara, M. M. 1989, *PASP*, 101, 5
- Sumiyoshi, K., Yamada, S., Suzuki, H., Shen, H., Chiba, S., & Toki, H. 2005, *ApJ*, 629, 922
- Swesty, F. D., & Myra, E. S. 2005a, in *Open Issues in Core Collapse Supernova Theory*, ed. A. Mezzacappa & G. M. Fuller, 176
- Swesty, F. D., & Myra, E. S. 2005b, *Journal of Physics Conference Series*, 16, 380
- Thompson, C. 2000, *ApJ*, 534, 915
- Thompson, C., & Duncan, R. C. 1993, *ApJ*, 408, 194
- Thompson, C., & Murray, N. 2001, *ApJ*, 560, 339
- Thompson, T. A., Burrows, A., & Pinto, P. A. 2003, *ApJ*, 592, 434
- Thompson, T. A., Quataert, E., & Burrows, A. 2005, *ApJ*, 620, 861
- Walder, R., Burrows, A., Ott, C. D., Livne, E., Lichtenstadt, I., & Jarrah, M. 2005, *ApJ*, 626, 317
- Wallerstein, G., Iben, I. J., Parker, P., Boesgaard, A. M., Hale, G. M., Champagne, A. E., Barnes, C. A., Käppeler, F., Smith, V. V., Hoffman, R. D., Timmes, F. X., Sneden, C., Boyd, R. N., Meyer, B. S., & Lambert, D. L. 1997, *Reviews of Modern Physics*, 69, 995
- Wang, L., & Wheeler, J. C. 2008, *ARA&A*, 46, 433
- Weaver, T. A., Zimmerman, G. B., & Woosley, S. E. 1978, *ApJ*, 225, 1021
- Weinberg, N. N., & Quataert, E. 2008, *MNRAS*, 387, L64

Wilson, J. R. 1971, *ApJ*, 163, 209

Wilson, J. R. 1985, in *Numerical Astrophysics*, ed. J. M. Centrella, J. M. Leblanc, & R. L. Bowers, 422

Wilson, J. R., & Mayle, R. W. 1988, *Phys. Rep.*, 163, 63

—. 1993, *Phys. Rep.*, 227, 97

Woosley, S. E. 1993, *ApJ*, 405, 273

Woosley, S. E., & Bloom, J. S. 2006, *ARA&A*, 44, 507

Woosley, S. E., Heger, A., & Weaver, T. A. 2002, *Reviews of Modern Physics*, 74, 1015

Woosley, S. E., & Weaver, T. A. 1995, *ApJS*, 101, 181

Yamasaki, T., & Foglizzo, T. 2008, *ApJ*, 679, 607

Yamasaki, T., & Yamada, S. 2007, *ApJ*, 656, 1019